Politecnico di Milano

SCHOOL OF INDUSTRIAL AND INFORMATION ENGINEERING
Master of Science – Nuclear Engineering

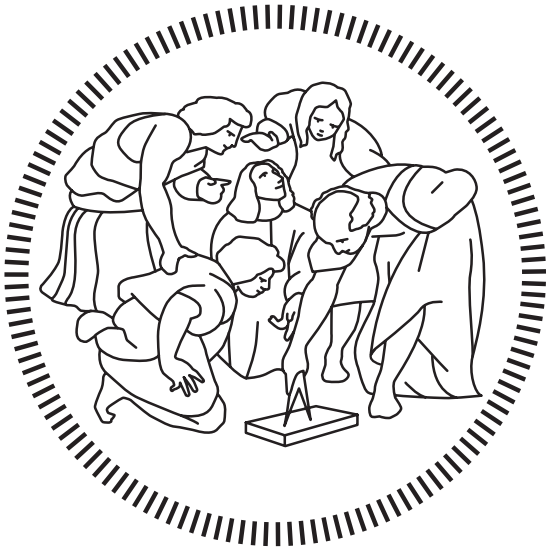

Study of Neutron-induced Damage to Cardiac Implantable Electronic Devices in Radiation Therapy

Supervisor
Prof. Marco Caresana

Co-Supervisor
Dott. ssa Cinzia Mordacchini

Graduation thesis of:
Christian Ferrante – 905123

Academic Year 2019 – 2020

Acknowledgements

Foremost, I would like to express my sincere gratitude to my supervisor, Prof. Marco Caresana, for giving me the opportunity to do this research. It was a great privilege to work and study under his guidance. I would also thank all the people who worked in this project, M. Quattrocchi, M. Severgnini, C. Mordacchini, F. D'Errico, M. Zecchin for their supervision, A. Hossein, S. Markovic, Y. E. Gardenali and L. Alticozzi for their useful contribution, and G. Zorloni for his collaboration. I extend my gratitude to Politecnico di Milano for everything I've learned through all these years of study. I'm extremely grateful to my family for their love, caring and sacrifices for educating me and preparing me for my future. A special mention goes to my niece Melissa, for cheering up my last two years with smiles and joy. Finally, a special thank goes to all my closest friends for their support.

"And tomorrow's just a mystery
But that's okay"
T. S.

Sommario

In radioterapia, specialmente per trattamenti ad alta energia, si è evidenziato in diverse occasioni il danneggiamento di dispositivi cardiaci impiantati nei pazienti. Sull'ipotesi che il danno possa essere indotto dalla inevitabile presenza di un campo neutronico secondario, lo scopo di questo lavoro di tesi è stato di caratterizzare la dose neutronica intorno a due diversi modelli di LINAC medicali e studiare i possibili danni indotti dall'interazione dei neutroni con i dispositivi.
Per la misurazione della dose neutronica, espressa come equivalente di dose ambientale H*(10), è stato usato il rivelatore LUPIN, un particolare REM counter progettato per applicazioni dosimetriche in campi pulsati. In funzione della disponibilità, lo strumento è stato confrontato con altri strumenti quali REM counter commerciali, dosimetri a bolle e simulazioni montecarlo. Per lo studio dei danni indotti ai dispositivi e dell'interazione con i neutroni, invece, sono state effettuate radiografie neutroniche con fascio termico su un vasto campione di pacemaker e defibrillatori.
I risultati mostrano che la produzione neutronica negli acceleratori, misurata in termini di dose, cresce significativamente all'aumentare delle energie del fascio e della dimensione del campo di irraggiamento, e che la dose diminuisce all'aumentare della distanza dal centro del fascio. Inoltre, la produzione di neutroni è significativamente minore per fasci di elettroni. Confrontati con gli altri metodi di acquisizione, i risultati del rivelatore LUPIN mostrano che questo strumento non solo rappresenta un valido sistema di monitoraggio della dose ambientale, in quanto in linea con le simulazioni montecarlo, ma anche costituisce l'unico valido strumento di misura attivo, poiché i REM counter convenzionali sottostimano pesantemente la dose a causa del pile-up di conteggi. Dalle radiografie neutroniche si è invece potuto notare un sospetto assorbimento neutronico in alcune componenti che potrebbe essere ricondotto alla presenza di borofosfosilicato (BPSG), un materiale spesso usato nella produzione di componenti elettroniche in alternativa al tradizionale fosfosilicato (PSG). I risultati della diagnosi dei dispositivi dopo le radiografie, inoltre, mostrano che un discreto numero di dispositivi ha riportato errori o malfunzionamenti, confermando di fatto l'ipotesi di danno indotto da neutroni termici.

Abstract

In high energy radiation therapy, there is experimental evidence that several damages can occur to cardiovascular implantable electronic devices (CIED). On the assumption that damages can be due to secondary photoneutrons, the aim of this thesis work was to assess the neutron ambient dose equivalent around two different linear accelerators (LINAC) and to study the induced damages from the interaction between neutrons and devices.

For the measurement of the dose, expressed as ambient dose equivalent H*(10), we used the LUPIN detector, a particular REM counter developed for dosimetric applications in pulsed neutron fields (PNF), together with different instruments like traditional REM counters, bubble dosimeters and montecarlo simulation. To study the interaction between neutrons and devices and the induced damages, also, a sample of 99 CIEDs was subjected neutron radiography with thermal neutrons and tested for proper operation before and after the irradiation.

Results show that the neutron field around linear accelerators increases at increasing energy and field size, while the ambient dose equivalent decreases for increasing distance from the isocenter of the machine. Also, the neutron production is way lower for electron beam therapy. Compared to other instruments, the LUPIN detector is confirmed not only as a valid instrument for neutron dosimetry in radiation therapy, in well agreement with monteacarlo simulations, but also the only valid active instrument, since traditional REM counters heavily underestimate the dose due to pulse pile-up. From neutron radiographs we have noticed a sensible neutron absorption in some integrated circuits that in principle can be due to the presence of borophosphosilicate glass (BPSG), a material often used in the production of semiconductor devices as an alternative to traditional phosphosilicate glass (PSG). The results from the post-irradiation device analysis, also, show that a fair number of devices has been suffering from errors and malfunctions, basically confirming the hypothesis of neutron-induced damages from thermal neutrons.

Riassunto Esteso

Introduzione

Secondo i dati pubblicati nell'ambito del progetto "Global Burden of Disease" (Figura 1), i problemi cardiovascolari rappresentano la prima causa di mortalità nel mondo, seguiti al secondo posto dal cancro che solo nel 2017 è stato la causa di oltre 9 milioni di morti [1]. Nella medicina moderna, la radioterapia convenzionale rappresenta una valida tecnica non invasiva per la lotta al tumore, basata sull'uso di radiazioni ionizzanti mirate per uccidere le cellule tumorali. Spesso accoppiata alla chemioterapia e alla rimozione chirurgica, la radioterapia è intrapresa da quasi il 70% dei pazienti oncologici [4].

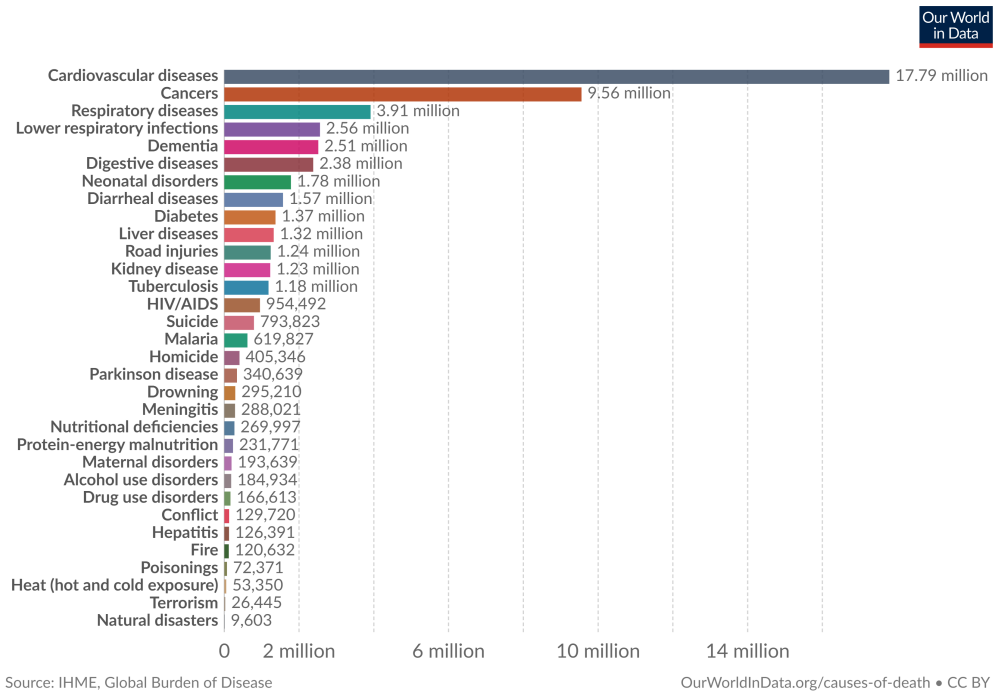

Figure 1. Numero di morti per causa, Mondo, 2017

A partire da uno studio preliminare condotto dall'Associazione Italiana di Aritmologia e Cardiostimolazine (AIAC) in collaborazione con Associazione Italiana Fisica

Medica (AIFM) e Associazione Italiana di Radioterapia Oncologica (AIRO), lo scopo di questo lavoro di tesi è stato di investigare sui possibili danni indotti da neutroni sui dispositivi impiantabili, siano essi pacemakers (PM) o defibrillatori (ICD), dei pazienti sottoposti a radioterapia convenzionale esterna, dunque condotta con fasci di elettroni o fotoni generati da acceleratori lineari (LINAC). Infatti, l'evidenza sperimentale di precedenti studi mostra che, specialmente quando la terapia è condotta con fotoni di alta energia (i.e. sopra i 6 MV), diversi danni hardware e software possono affliggere i dispositivi, rendendo la terapia particolarmente pericolosa per quei pazienti definiti "pacemaker dipendenti", ovvero la cui funzionalità cardiaca è inevitabilmente legata al corretto funzionamento del dispositivo impiantato [4] [5] [6]. I malfunzionamenti possono essere divisi principalmente in tre categorie a seconda della gravità e possono essere transitori, temporanei o permanenti. Una delle possibili cause di malfunzionamento, che verrà investigata, potrebbe essere la presenza nel dispositivo di borofosfosilicato (BPSG), un materiale spesso usato come copertura protettiva nella produzione di dispositivi a semiconduttore, per le sue ottime proprietà isolanti e per la sua resistenza a shock meccanici e termici, in alternativa al più tradizionale fosfosilicato (PSG). Il BPSG, infatti, per la presenza di boro-10 nella matrice (un isotopo del boro presente in natura con abbondanza isotopica del 20%), può indurre assorbimento di neutroni termici e produzione, per reazione (n, α), di particelle pesanti cariche in grado di danneggiare le componenti elettroniche [40]. In un acceleratore lineare, una corrente di elettroni viene accelerata in una guida d'onda e inviata contro un bersaglio in metallo, dove la conversione in fotoni avviene per bremsstrahlung. Il fascio così prodotto viene poi attenuato, collimato e inviato al sito tumorale secondo uno specifico piano di trattamento. Lo schema generale della testata di un LINAC è mostrato in Figura 2.

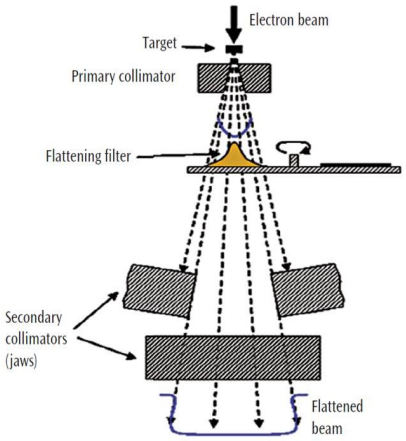

Figure 2. Schema della testata di un acceleratore lineare

Tuttavia, dal momento che la maggior parte delle componenti nella testata della macchina inclusi il bersaglio e i collimatori sono fatti in tungsteno [7] [8], la presenza di fotoni di alta energia può portare facilmente alla produzione di fotoneutroni per reazione (γ, n). Per fotoni di energia superiore alla soglia energetica di reazione (circa 7 MeV), l'energia dei neutroni prodotti può essere espressa dalla relazione

$$E_n(\theta) \cong \frac{M(E_\gamma) + Q}{m + M} + \frac{E_\gamma \sqrt{(2mM)(m + M)(E_\gamma + Q)}}{(m + M)^2} \, cos(\theta) \tag{1}$$

dove θ è l'angolo di incidenza tra il fotone e il neutrone prodotto, E_γ è l'energia del fotone, m e M sono rispettivamente le masse del neutrone e del nucleo di rinculo moltiplicate per il fattore c^2. Invece, la fluenza neutronica Φ (n·cm^{-2}) ad una distanza d dall'isocentro per 1 Gy di dose terapeutica è [9]

$$\Phi = \Phi_{dir} + \Phi_{sc} + \Phi_{th} = \frac{aQ}{4\pi d^2} + \frac{5.4aQ}{S} + \frac{1.26Q}{S} \tag{2}$$

dove Φ_{dir} è il contributo dei neutroni diretti, Φ_{sc} il contributo dei neutroni scatterati e Φ_{th} il contributo dei neutroni termici, Q la qualità della sorgente neutronica, a il fattore di trasmissione (i.e. 0.85 per il tungsteno, 1 per il piombo) e S la superficie della stanza di trattamento in cm^2. Lo spettro risultante dei neutroni all'interno della stanza mostra un picco principale alle alte energie (i.e. intorno ad 1 MeV) e un secondo picco dovuto ai neutroni termici (i.e. 0.025 eV) [7].

Strumenti e Metodi

La prima parte del lavoro è stata di caratterizzare la dose neutronica, espressa come equivalente di dose ambientale H*(10), in differenti posizioni intorno all'acceleratore lineare e in diverse condizioni di funzionamento della macchina. Gli acceleratori che sono stati usati in questo studio sono il Clinac DHX di Varian System (Palo Alto, California) e il Synergy 3028 di Elekta (Stoccolma, Svezia).
Le misure sono state acquisite con l'ausilio del rivelatore LUPIN (distribuito da ELSE Nuclear srl, Via Dante Alighieri 16, 21052 Busto Arsizio (VA), Italia). Il rivelatore LUPIN (Long Interval, Ultra-wide dynamic Pile-up free Neutron rem counter) è un particolare rem counter sviluppato specificamente per applicazioni di radioprotezione in condizioni di campi neutronici pulsati e campi misti.
Il LUPIN (Figura 3), grazie ai suoi prinicipi di funzionamento innovativi, è in grado di superare le limitazioni dei tradizionali rem counter e di soddisfare i molti requisiti richiesti da un un rivelatore ideale per campi neutronici pulsati in termini di sensibilità e frequenza di impulsi. In più, è in grado di rigettare efficientemente il contributo

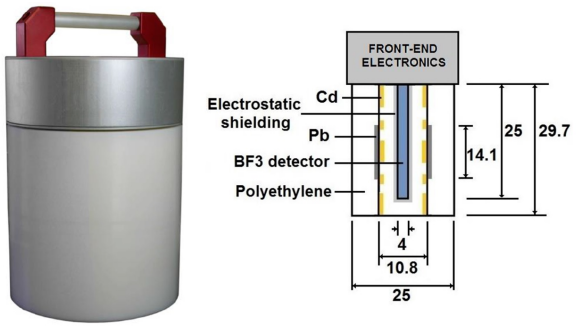

Figure 3. Rivelatore LUPIN (a sinistra) e disegno schematico delle componenti principali (a destra)

dovuto ai fotoni che accompagnano i neutroni in condizioni di campo misto [12] [21] [22].

Al fine di confrontare le performance del LUPIN con altri strumenti, alcune misure sono state ripetute, a seconda della disponibilità, con rem counter tradizionali, rivelatori a bolle e simulazioni montecarlo.

Un rivelatore a bolle, o dosimetro a bolle (Figura 4), è un particolare tipo di rivelatore di radiazioni formato da una sospensione di goccioline di freon super-riscaldato all'interno di una matrice inerte e immiscibile. Quando la radiazione neutronica in-

Figure 4. Dosimetro a bolle per neutroni veloci (BD-PND)

teragisce con la matrice all'interno del volume attivo del dosimetro, lungo la traccia si ha produzione di particelle cariche la cui energia viene depositata causando la vaporizzazione locale del freon e la nucleazione delle goccioline in gocce visibili a occhio nudo, che possono essere successivamente contate e convertite in equivalente di dose ambientale attraverso la sensibilità dello strumento, espressa come *bolle* μSv^{-1}, fornita dal produttore.

Insieme ai rivelatori a bolle, inoltre, è stato utilizzato un particolare fantoccio dosimetrico sviluppato dall'Università degli Studi di Trieste. Il fantoccio, schematizzato in Figura 5, è uno speciale contenitore formato da moduli di polietilene, in grado di ospitare i dosimetri, circondati da strati di carbonato di boro.

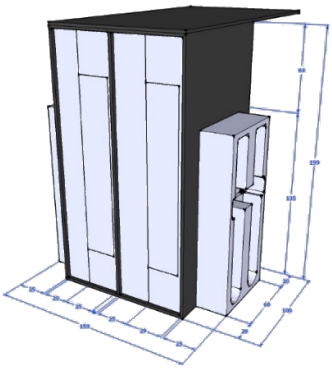

Figure 5. Fantoccio dosimetrico dell'Università degli Studi di Trieste

Tale fantoccio rende possibile sia l'assorbimento della componente termica del fascio all'interno dello strato borato, sia l'attenuazione delle componenti veloce ed epitermica nel polietilene, al fine di studiarne il comportamento in una matrice sufficientemente simile al corpo umano.
Il codice montecarlo, sviluppato per l'acceleratore Synergy sulla base di dati forniti direttamente dal produttore, è stato sviluppato in MCNPX dall'Università degli Studi di Trieste al fine di simulare la produzione neutronica nelle medesime condizioni con cui la dose è stata misurata dal rivelatore LUPIN. In particolare, la fluenza neutronica in un certo punto è stata calcolata attraverso la funzione F5 e poi convertita in equivalente di dose ambientale H*(10) attraverso i coefficienti di conversione presenti in MCNPX. In Figura 6 è mostrato il modello 3D della testata usato per la simulazione.

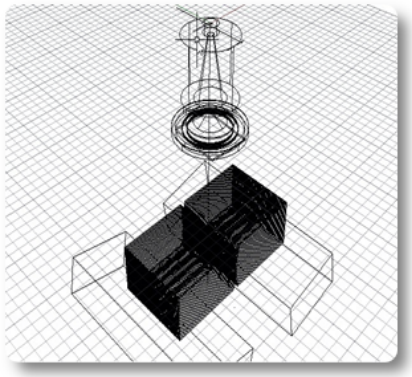

Figure 6. Modello 3D per simulazione montecarlo. Si possono riconoscere il bersaglio, il filtro d'attenuazione e i collimatori

La seconda parte del lavoro si è concentrata sullo studio dell'interazione tra neutroni termici e dispositivi cardiaci, in termini di assorbimento e di danni effettivamente indotti. A questo proposito, un campione di 99 dispositivi è stato inviato al Paul Scherrer Institute (PSI) per produrre un set di radiografie neutroniche presso la stazione

di radiografia neutronica termica NEUTRA (Figura 7).

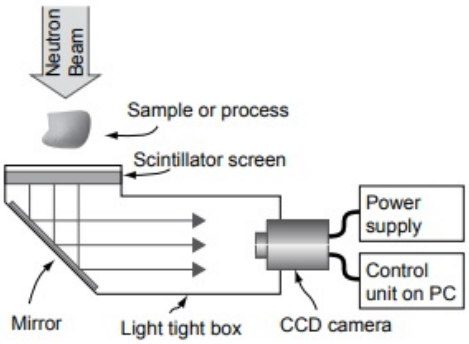

Figure 7. Sistema di lettura della stazione NEUTRA, PSI

La radiografia neutronica è una tecnica di acquisizione di immagini non distruttiva basata sulle proprietà di attenuazione dei neutroni di un campione e, vista la differenza nella attenuazione di un fascio di neutroni rispetto ad un fascio di fotoni, può essere considerata una tecnica complementare alla radiografia X tradizionale.
La stazione NEUTRA si trova lunga una delle 4 linee gemelle di neutroni termici uscenti dalla sorgente di neutroni da spallazione SINQ. Il fascio è moderato da acqua pesante.
I dispositivi sono stati irraggiati da un flusso di circa 10^7 n/cm^2/s per circa 2 minuti ciascuno (con eccezioni fino a 10 minuti) e il risultato è stato un set di 6 immagini per ogni dispositivo. Tutte le immagini sono state processate mediante l'uso del software "ImageJ" e ogni dispositivo è stato testato per il corretto funzionamento prima e dopo l'irraggiamento, eccetto uno che non è stato possibile rispedire a causa di una eccessiva attivazione.

Attività Sperimentale

L'equivalente di dose ambientale H*(10) intorno agli acceleratori lineari è stato misurato in modo sistematico operando le macchine in diverse condizioni di funzionamento quali modalità d'erogazione (i.e. fotoni, elettroni), energia del fascio e dimensione del campo. Per entrambe le macchine, la testata è stata fissata in posizione verticale (i.e. ad un angolo di 0°) e l'irraggiamento è stato protratto per 20 secondi con una frequenza d'impulso di 600 unità monitor al minuto (da calibrazione, 1 MU = 1 cGy alla profondità di build-up per campi 10x10), per una dose totale erogata di circa 2 Gy su un fantoccio di acqua solida. Il rivelatore LUPIN è stato posizionato sia a diverse distanze lungo il lettino di trattamento sia a fianco di esso su un tavolino, a 81 cm lungo l'asse e 62.5 cm di distanza laterale. Quest'ultima posizione è stata usata anche per i dosimetri a bolle. Successivamente, per ottenere una misura più

realistica di quella che potrebbe essere la dose effettiva misurabile dal LUPIN durante una sessione di terapia, sono stati riprodotti piani di trattamento reali al seno e ai polmoni su un fantoccio BOMAB fornito dall'Università degli Studi di Pisa. Al fine di emulare correttamente il seno, come mostrato in Figura 8, sono state aggiunte al fantoccio due mammelle artificiali in silicone rispettivamente di 300 cm^3 e 500 cm^3.

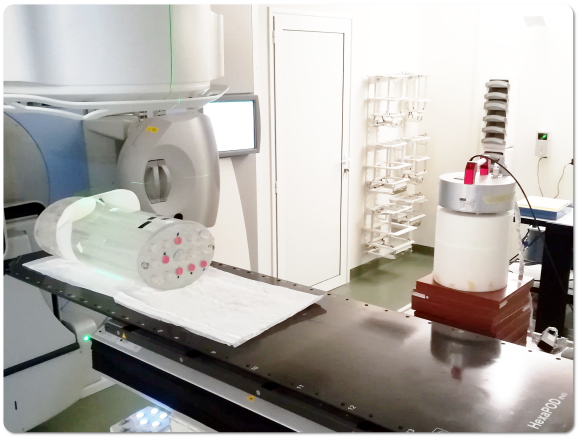

Figure 8. Fantoccio BOMAB con mammelle in silicone. A destra, il rivelatore LUPIN

Risultati

Dai risultati ottenuti è evidente che la produzione di fotoneutroni è molto maggiore per campi di fotoni piuttosto che di elettroni, fino a un ordine di grandezza di differenza, e in particolare per fotoni ad alta energia (i.e. sopra i 6 MV) e campi di trattamento più larghi, in accordo con l'ipotesi che la maggior produzione neutronica avvenga nelle componenti in tungsteno, in particolare il bersaglio e i collimatori primari a monte della testata. In generale, i dati acquisiti dal rivelatore LUPIN, normalizzati per la dose erogata (in Gy o MU) sono in buon accordo con i dati disponibili in letteratura sia per quanto riguarda i fotoni che gli elettroni. Parte dei risultati sono riportati in Figura 9.

Quando messo a confronto con le misure di altri rem counter tradizionali, il LUPIN si conferma in grado di registrare una dose molto maggiore, specialmente per fotoni ad alta energia, e un profilo di attenuazione con la distanza coerente, laddove invece gli altri dispositivi mostrano un andamento piatto della dose all'aumentare della distanza, se non leggermente crescente, a causa dell'evidente pile-up dei conteggi.

Rispetto ai risultati calcolati con il codice montecarlo, il LUPIN si mostra in buon accordo, specialmente considerando l'incertezza di misura. I dosimetri a bolle invece, sia misurati in loco che da letteratura, mostrano una risposta molto inferiore e questa differenza è ancora da investigare, ma probabilmente riconducibile ad una

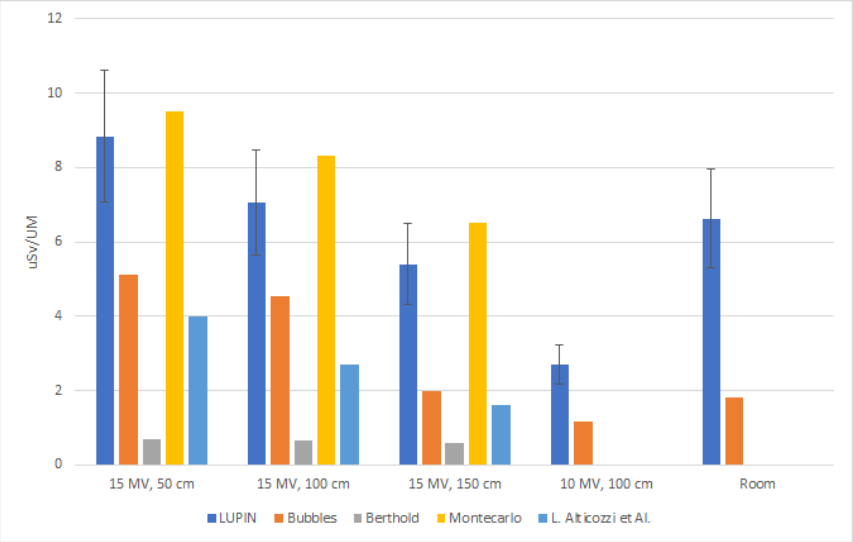

Figure 9. Dose H*(10) per MU a confronto: LUPIN, dosimetri a bolle, simulazione montecarlo e dati di letteratura. L'etichetta "Room" indica le misure effettuate con il rivelatore posto adiacentemente al lettino del paziente

conservazione non ottimale dei dosimetri. Comunque, considerando per i dosimetri a bolle anche i risultati disponibili in letteratura, si evince che il principale contributo alla dose è dovuto ai neutroni veloci, con un rapporto thermal-to-fast nell'ordine del 10%, ma il maggior flusso neutronico si ha per la componente termica, soprattutto all'aumentare della distanza dall'isocentro della macchina.
I risultati ottenuti dalle radiografie neutroniche, invece, danno spazio a considerazioni più ampie e interessanti. Se da un lato la maggior parte delle immagini per modelli

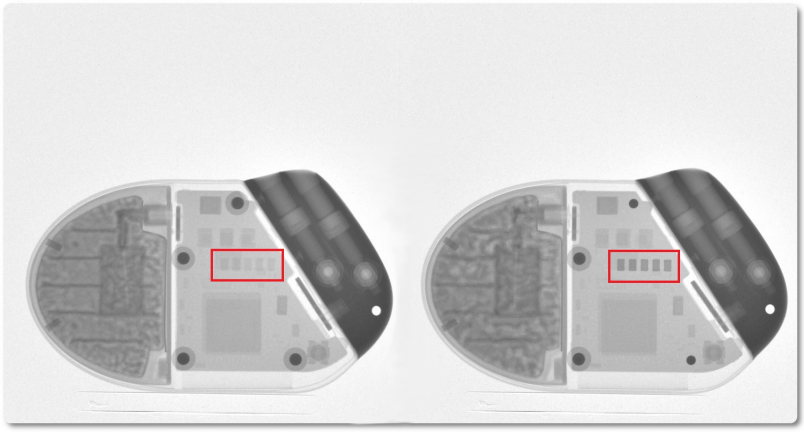

Figure 10. Radiografie neutroniche di due dispositivi identici prodotti da Medico. Si può notare un evidente maggior assorbimento neutronico nei chip del dispositivo a sinistra.

simili non hanno evidenziato differenze, per cui non si potrebbe confermare o escludere la presenza di PBSG nei modelli, in alcuni casi, come riportato ad esempio in

Figura 10, si evidenzia un insolito assorbimento neutronico in determinati chip di una particolare unità che, in linea di principio, potrebbe confermare l'ipotesi che sia possibile la presenza di BPSG in alcuni dispositivi al posto del più tradizionale PSG, e che la presenza possa variare anche all'interno di uno stesso modello, in quanto i due materiali sono spesso trattati come equivalenti in fase di produzione.
Dai test di funzionamento, comunque, i modelli riportati in Figura 10 in particolare non sono risultati danneggiati dalle radiografie, perciò la sola presenza di BPSG potrebbe non bastare a giustificare i danni indotti. In ogni caso, dal campione di 98 dispositivi testati dopo l'irraggiamento, 32 dispositivi risultano danneggiati e 8 hanno mostrato variazioni in parametri importanti tra cui, ad esempio, la vita residua della batteria (Figura 11). Nei casi più rilevanti, 7 dispositivi hanno mostrato errori di

Figure 11. Riassunto delle analisi di funzionamento dei dispositivi condotte a seguito delle radiografie neutroniche, divise per produttore

telemetria, 1 ha completamente esaurito la carica e 1 è risultato completamente non funzionante e impossibile da testare. Dunque, è stato possibile confermare di fatto l'ipotesi che il danno da radiazione sia indotto, almeno in parte, da neutroni termici, e che questo può riguardare sia la componentistica elettronica che le batterie.

Contents

List of Figures

List of Tables

Introduction

Cardiovascular diseases are the leading cause of death globally. The second biggest cause are cancers [1]. According to the 2016 World Health Organization (WHO) report on cardiovascular diseases, an estimated 17.5 million people died from cardiovascular diseases in 2012, representing 31% of all global deaths. Of these deaths, 85% are due to heart attack and stroke [2]. On the other hand, in the World Cancer Report 2014, it is stated that "approximately 14 million new cases and 8 million cancer-related deaths in 2012 have been registered, affecting populations in all countries and regions". Also, the number of cancer cases is expected to rise to 25 millions over the next 20 years [3]. From a study published by the Italian Associations of Arrhyth-

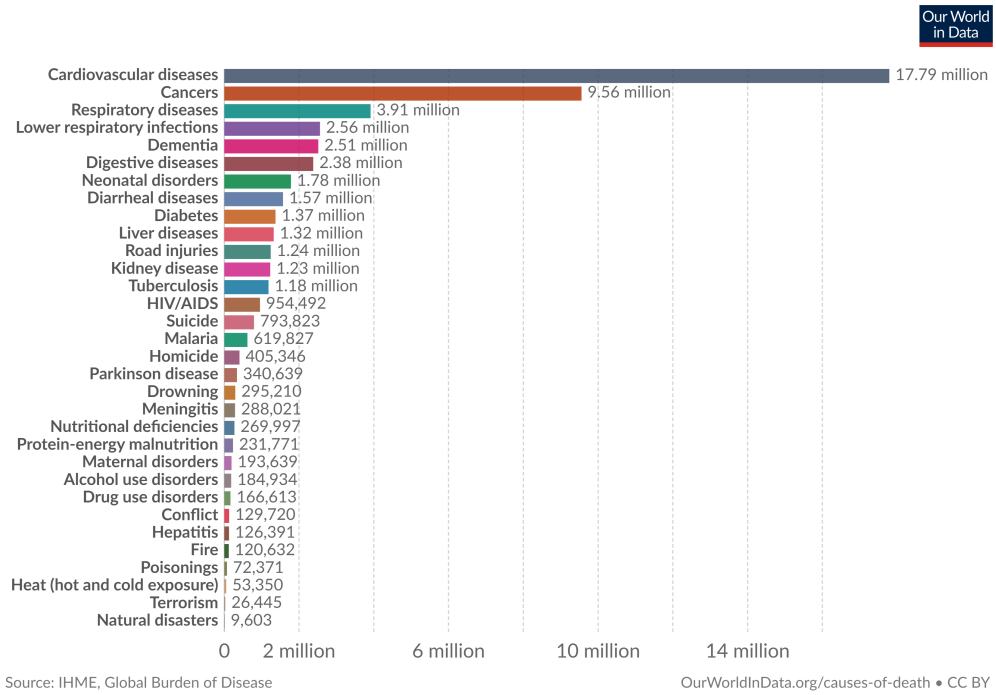

Figure 12. Number of deaths by cause, World, 2017

mologists "Associazione Italiana Aritmologia e Cardiostimolazione" (AIAC), Medical Physicists "Associazione Italiana Fisica Medica" (AIFM) and Radiation Oncologists "Associazione Italiana Radioterapia Oncologica" (AIRO), following the AIAC

XV national meeting (April 12^{th}-13^{th} 2018, Bologna), over 600'000 CIEDs, among pacemakers (PM) and implantable cardioverter-defibrillators (ICD), are implanted annually in Europe and radiation therapy is undertaken by almost 70% of cancer patients, including many patients with implantable cardiovascular devices.
Nevertheless, there is experimental evidence that when high radiation dose and high beam energy (above 6 MV) are used in radiation therapy, several hardware and software malfunctions can occur to the CIEDs, and it is important to be aware that these malfunctions are particularly dangerous when dealing with a pacemaker-dependant patient, that is a person whose heart functionality is totally dependent on the pacemaker. For this reason, the main goal of the study was to develop a strict protocol for the "Management of patients with cardiac implantable electronic devices (CIED) undergoing radiotherapy" in order to avoid fathal consequences [4].
Malfunctions can be divided depending on the severity in:

- *transient malfuctions*, that are due to electro-magnetic interferences and last only for the duration of the radiation exposure.
- *reset-to-backup setting malfuctions*, that are temporary error that can be resolved by reprogramming the device;
- *permanent malfunctions*, that cannot be resolved. The device must be explanted and substituted.

A list of literature relevant device malfunctions is available in reference [4], [5] and [6]. Few examples are reported in Table 1.

Table 1. In vivo published data on radiotherapy and CIEDs

First author (Year)	Tumor site	Device type	Total RT dose/fraction	Energy	Effects
Dasgupta (2011)	Cardiac Metastases	PM	37.5/2.5 Gy	n.d	Ventricular undersensing
Lau (2008)	Prostate	ICD	74/2 Gy	23 MV	Reset into fallback mode
Frantz (2003)	Breast	PM	66/2 Gy	n.d	Loss of telemetry capabilities

The purpose of this thesis work, a joint collaboration between Politecnico di Milano, AIFM, AIAC, AIRO, Università degli studi di Trieste and Università degli Studi di Pisa is to further expand the knowledge in radiation damage to CIEDs by studying in particular the possible neutron induced damages, caused by the secondary neutrons generated in the medical linear particle accelerator (LINAC) gantry. These so called "photoneutrons" are produced by means of (γ, n) reactions by the interaction of high energy photons with the constituent materials of the linac head, mainly tungsten [7] [8]. In fact, its low reaction threshold for the (γ, n) reaction (about 6 or 7 MeV depending on the isotope), together with a large reaction cross section (Table 2) and

Table 2. Photoneutron production cross section for the most common isotopes of typical materials present in the head of a linear accelerator (from IAEA)

Element	Atomic Z	E_{min} [MeV]	E_{max} [MeV]	σ [mb]
^{12}C	6	18.7	23	13.1
^{48}Ti	22	11.6	16.1	48.55
^{56}Fe	26	11.2	20	45
^{63}Cu	29	10.9	16.6	69.9
^{184}W	74	7.4	12.814	390.87
^{208}Pb	82	7.4	13.743	500

a low neutron absorption cross section, results in a high photoneutron emission [7]. According to the International Atomic Energy Agency (IAEA) report 47 [9], the neutron fluence Φ (n·cm^{-2}) at a distance d from the isocenter per 1 Gy of primary radiation is

$$\Phi = \Phi_{dir} + \Phi_{sc} + \Phi_{th} = \frac{aQ}{4\pi d^2} + \frac{5.4aQ}{S} + \frac{1.26Q}{S} \tag{3}$$

where Φ_{dir} is the contribution of direct neutrons, Φ_{sc} is the contribution of scattered neutrons and Φ_{th} is the contribution of thermal neutrons, Q is the neutron source quality, a is the transmission factor (0.85 for tungsten, 1 for lead) and S is the total treatment room surface in cm^2.

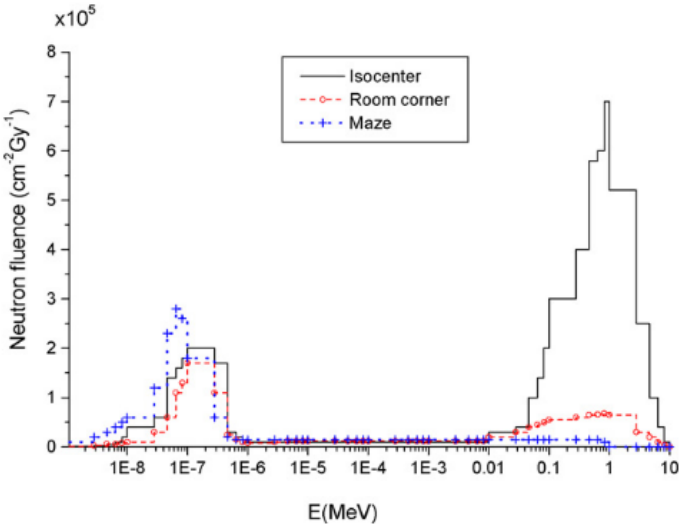

Figure 13. Neutron spectra at different points of a typical treatment room for a 15MeV photon beam

Figure 13 [7] shows that the fast neutron fluence is the main contribution at the isocenter and its contribution decreases at increasing distance. On the contrary, the thermal neutron fluence is almost 7 times lower at the isocenter but increases with increasing distance. This is due to the thermalization process, which happens by

scattering inside the room. Finally, it is shown that the epithermal neutron fluence is almost constant at different distances.
Though measurements of neutron fluence and ambient dose equivalent around medical linacs have already been performed with passive detectors in literature (see ref. [5], [8], [10] and [11]), the need to define a strict protocol for patients management requires the capability to get a valid real-time response in terms of neutron dose during the treatment, for which purpose passive dosimeters are not suitable. For this reason, the LUPIN BF3-NP detector, a neutron rem counter specifically designed to work in pulsed and mixed neutron fields (see ref. [12] and [13]), has been chosen as the ideal candidate for the acquisition of neutron measures for this work. Sample measurements were also acquired with traditional REM counters and bubble dosimeters for comparison, and a montecarlo simulation for the Synergy accelerator was developed by the University of Trieste.
Measurements were made between July and October 2019 at the "Ospedale di Circolo e Fondazione Macchi" hospital in Varese (IT), housing a Varian Clinac DHX, and around two identical Elekta Synergy 3028 at the "San Luca" hospital in Lucca (IT) and the "Ospedale Maggiore" hospital in Trieste (IT), in order to compare the results either between different and identical linear accelerators.
To study the neutron induced damage on devices, a set of neutron radiography acquisitions were made on several devices. The radiographs were performed by the Radiation Metrology Section of the Paul Scherrer Institute (PSI) in Villigen (CH) and the images were processed with the open source image processing program "ImageJ". The main goal of the analysis was to search for a sufficient boron presency to justify the neutron damage by means of $^{10}B(n,\alpha)^{7}Li$ reactions with thermal neutrons. In fact, many semiconductor devices are often covered with a borophosphosilicate glass (BPSG) layer instead of the more common phosphosilicate glass (PSG), both being good alternatives for their good mechanical and isolating properties,. Also, all the devices were tested for proper operation before and after the irradiation. Traditional radiographs of a couple devices were also made for comparison.
To better undestand the framework of the study, a general overview on radiation therapy is given in Chapter 1, together with a brief description of how a linear accelerator works. The second chapter focuses on the principles of neutron physics and detection, with a detailed description of the LUPIN neutron detector, the bubble dosimeters and the montecarlo simulation that were used in this work. The third chapter is description of the measurements made with linear accelerators, followed by results and comments.
The fourth chapter describes the metodology and result of the neutron radiography

analysis and the device testing. Finally, in the conclusive chapter, additional comments and future developments of the work are presented.

Chapter 1

Overview on Radiation Therapy

Radiation therapy, or radiotherapy, is a type of cancer therapy that uses radiation beams to kill cancer cells. Its earliest roots go back to the discovery of X-rays in 1895 by Wilhelm Röntgen, which soon attracted the interest of Léopold Freund and Eduard Schiff, who suggested they could be used in the treatment of disease. Though no reliable contemporary source of this claim exists, Emil Grubbe of Chicago was possibly the first American physician to use X-rays to treat cancer, beginning in 1896.
In general, the term *radiation therapy* is most often referred to external beam radiation therapy. In this type of therapy, the high-energy beam comes from a machine, for example a LINAC, placed outside the human body in the treatment room. Nowadays, radiation therapy mostly uses X-ray or electron beams, but protons or other beam particles can also be used for their peculiarities.
Radiation therapy damages cells by destroying the DNA genetic material that controls how cells grow and divide. While it is true that both healthy and cancer cells get damaged, the main goal of radiation therapy is to damage as few normal, healthy cells as possible. To spare nearby tissues, shaped radiation beams are aimed from several angles of exposure to intersect at the tumor site, providing a much larger absorbed dose there than in the surrounding healthy tissue. Also, healthy cells can often repair much of the damage caused by radiation through DNA repair processes.

1.1 The DNA

The Deoxyribonucleic Acid (DNA) is the biomolecule containing the hereditary material in humans and almost all other organisms. It was first isolated by Friedrich Miescher in 1869, and its molecular structure was first identified by Francis Crick and James Watson at the Cavendish Laboratory within the University of Cambridge in 1953, supported by X-ray diffraction data acquired by Raymond Goslingand Rosalind

Franklin at King's College London. In 1962, after Franklin's death, Watson, Crick, and Wilkins jointly received the Nobel Prize in Medicine.
DNA is shaped as a double helix of sugar-phosphate chains. Each chain carries a unique sequence of four nitrogenous bases: adenine (A), guanine (G), cytosine (C) and thymine (T). Together, a base, sugar, and phosphate are called a nucleotide. The two chains are connected one each other by hydrogen bonds between GC and AT pairs. A chemical representation of the DNA is given in Figure 1.1.

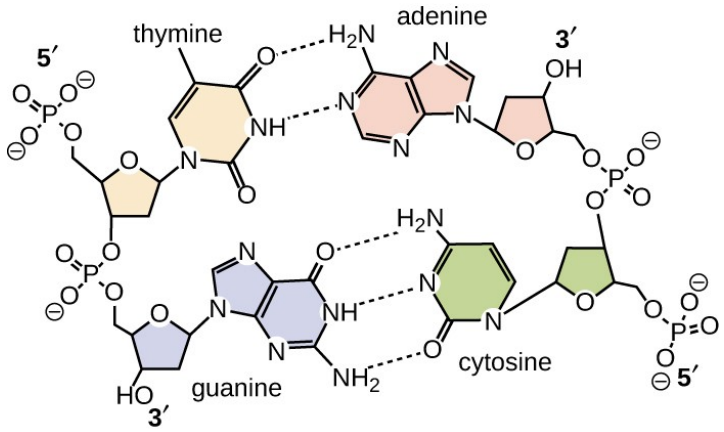

Figure 1.1. Chemical structure of DNA

Human DNA consists of about 3 billion bases, and more than 99 percent are the same in all people. The order, or sequence, of these bases determines all the information available for building and maintaining an organism.
The most important property of DNA is its capability to replicate, or make copies of itself. In fact, each strand of DNA in the double helix can serve as a pattern for duplicating the sequence of bases. This is critical in cell duplication because each new cell needs to have an exact copy of the DNA present in the old one. Another important role of the DNA is played in protein biosynthesis. In fact, the DNA serves as the source of information for the process which builds proteins.

1.2 Radiation Quantities

Before heading to the biological effects of radiation, it is important to give a brief introduction to the principal physical quantities that will be mentioned. These can be divided in three main groups: radiometric quantities (related to the physical properties of the radiation), protection quantities (related to the biological effects) and operational (measurable) quantities.

Radiometric quantities

To define the properties of a radiation field, it is important to define the *particle fluence* (rate), that is expressed as

$$\phi = \frac{dN}{dAdt} \ \left[m^{-2}s^{-1}\right] \tag{1.1}$$

where dN is the number of particles passing through a sphere with differential cross section dA in a time interval dt.
Instead, to deal with the energy deposition of a ionizing radiation, a useful quantity to be defined is the absorbed dose. The absorbed dose is defined as the ratio between the mean deposited energy of a ionizing radiation and the mass of the deposition site. According to the following relation,

$$D = \frac{d\bar{\epsilon}}{dm} \ [Gy] \tag{1.2}$$

where $d\bar{\epsilon}$ is the mean deposited energy and dm is the mass. The unit of measure of the absorbed dose is the Gray (1 Gy = 1 J/kg).

Protection quantities

The exposure to the same amount of energy per unit mass (i.e. absorbed dose) generates different effects depending on the properties of the radiation. The main difference between different types of particles can be taken into account by the Linear Energy Transfer (LET).
The LET represents the energy deposition spatial density, and it mostly depends on the particle type (photon, electron, neutron, etc.) and energy. To take into account the LET, the absorbed dose is transformed into a new quantity called *Dose Equivalent* (H):

$$H = D \cdot Q \ [Sv] \tag{1.3}$$

where Q is a parameter related to the LET (dimensionless). The S.I. unit of measure of the dose equivalent is again J/kg, but, to differentiate it from the absorbed dose and to consider the presence of the Q factor, it is called *Sievert* (1 Sv = 1 J/Kg).
Also, to take into account the possibility that different radiation fields can interact with the same tissue, the equivalent dose to tissue is defined as the weighted average

$$H_T = \sum_R \omega_R D_R \tag{1.4}$$

where ω_R is the dimensionless weighting parameter of the radiation R and D_R is the absorbed dose in tissue of such radiation.
Finally, to consider a whole body irradiation, the so called *Effective Dose* is defined to be the weighted sum of the equivalent dose in tissue over all tissues, where ω_T is the tissue-dependent weighting factor.

$$E = \sum_T \omega_T H_T \tag{1.5}$$

Operational Quantities

Due to the impossibility of directly measuring protection quantities in case of external exposure, the International Commission on Radiological Protection (ICRP), in its publication ICRP 60 ("1990 Recommendations of the International Commission on Radiological Protection") defines the so-called *operative quantities* [14]. The most important quantity for the present work is the *Ambient Dose Equivalent*, or H*(10), that is defined by ICRP as follows: *"The ambient dose equivalent, H*(10), at a point of interest in the real radiation field, is the dose equivalent that would be produced by the corresponding aligned and expanded*[1] *radiation field, in the International Commission on Radiation Units and Measurements (ICRU) sphere*[2] *at a depth of 10 mm, on the radius opposing the direction of radiation incidence".*

1.3 Biological Effects of Radiation

Biological effects of radiation mainly depend on ionization and excitation of atoms and molecules of the tissue where the interaction occurs. There are two types of biological effects, direct and indirect effects.
Direct effects happen when the impinging radiation directly breaks a molecular bond of a cellular species (e.g. the DNA). Possible damages induced to DNA are shown in Figure 1.2 and can be described as follows:

1. Changing the chemical structure of the bases;
2. Breaking the sugar-phosphate backbone;
3. Breaking the hydrogen bonds connecting the base pairs.

[1] Hypothetical radiation field which shows the same spectral fluence and specific direction of incidence of the point of interest, in a large volume of space.

[2] A theoretical 30 cm diameter "tissue equivalent" sphere consisting of a material with a density of 1 g·cm^3 and a mass composition of 76.2% oxygen, 11.1% carbon, 10.1% hydrogen and 2.6% nitrogen

It is important to note that the break of the backbone can be a single strand break (SSB) or a double strand break (DSB). Double-stranded DNA breaks are much more difficult to repair, and can easily lead to cell death.
Indirect effects, instead, happen when the radiation interacts with the medium surrounding cells (e.g. water) producing chemically reactive species, called scavengers, which can diffuse. Then, it will be the reaction between these reactive species and the cellular species which causes damages, not the radiation itself.

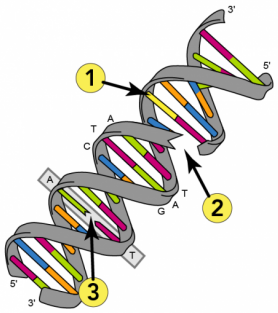

Figure 1.2. Possible damages induced to DNA

Since human cells are made for 70% of water, let us consider the main reactions occurring in water.

$$H_2O \rightarrow H_2O^+ + e^- \rightarrow H_2O^+ + e_{aq} \tag{1.6}$$

$$H_2O^+ \rightarrow \bullet OH + H^+ \tag{1.7}$$

$$H_2O \rightarrow H_2O^* \rightarrow H \bullet + \bullet OH \tag{1.8}$$

As described in equation (1.6), a water molecule can be excited producing a positive ion and a free electron. This electron can then diffuse and become a solvated electron, with a mean life in water of about 100 μs. Meanwhile, the positive water ion can separate in a free proton and a radical •OH, as shown in equation (1.7). Also, from equation (1.8) we see that a water molecule can be excited by incident radiation, and such excited species can then dissociate in free radicals H• and •OH, each with a mean life of about 1 μs in water medium. All these reactive species can recombine or react with DNA. For example, OH• radicals can react with hydrogen atoms inside a DNA molecule to produce Hydrogen Peroxide (H_2O_2). These reactions can cause the same types of DNA damage that were mentioned above.
After the chemical bonds have been broken, two types of damage can occur:

– deterministic effects, which happen above a tissue specific threshold dose and

higher is the dose, more severe are the symptoms.

– stochastic effects, which can happen at lower dose and their effects can emerge up to tens of years later the exposition. Symptoms in this case are not dependant on the dose, but, higher is the dose, higher is their probability to occurr.

Relative Biological Effectiveness

To compare different radiation qualities in their capability of producing a certain effect, a quantity called Relative Biological Effectiveness (RBE) is defined, that is the ratio of biological effectiveness of a reference radiation field relative to a different one, given the same amount of absorbed energy. In general, the reference radiation is considered as 150 kV X-rays or ^{60}C gamma rays.

$$RBE = \frac{D_X}{D} \tag{1.9}$$

RBE increases with LET up to a maximum for 140 keV/μm^{-1}, then decreases because of over-killing effect, since a higher ionization density results to be inefficient (see Figure 1.3).

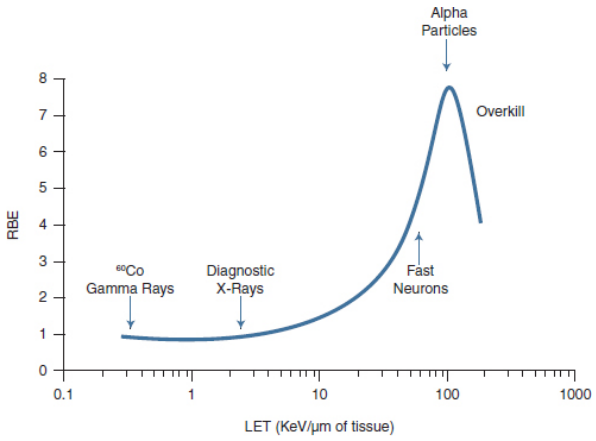

Figure 1.3. RBE against LET

Survival Curves

One of the most important biological effects of radiation is cell inactivation (cell death). This is studied by irradiating cellular cultures in radiation biology. The experimental data are plotted as *surviving curves* representing the logarithmic number of survived cells at a given endpoint with respect to the absorbed dose.
A cell is said to be survived if it can generate at least a colony of 50 daughters. Some damaged cells may continue to function for a time, but, if they do not reproduce,

they are not counted as survivors.
Mammalian cells survival curves generally show an exponential behaviour (i.e. a linear trend in the logarithmic plot) to high dose of radiation with a "shoulder" in the low-dose range, as shown in Figure 1.4.

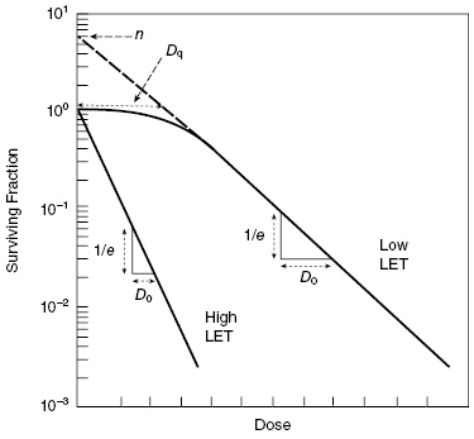

Figure 1.4. Survival curves plot

The presence of the edge signals the capability of cells to repair damages in case of low dose. However, it is important to note that survival curves would change under different conditions: radiation LET, different environment, oxygenation, dose fractionation and cell life-cycle.

Survival Curves Models

The simplest model (i.e. the pure exponential model) is based on the assumption that a singular ionization event is enough to inactivate the cell. In this case, the number of inactivated cells will be proportional to the absorbed dose through the exponential relationship

$$N = N_0 e^{-D/D_0} \tag{1.10}$$

where D_0 is the *mean lethal dose*.
A better model, accounting for damage repair, can be expressed in the form

$$\frac{N}{N_0} = 1 - (1 - e^{-D/D_0})^n \tag{1.11}$$

where n is the intercept of the exponential with the ordinate axis.
Finally, a last model based on the assumption that DSB lead to inactivation, is expressed as follows:

$$\frac{N}{N_0} = \alpha D + \beta D^2 \tag{1.12}$$

where α $[Gy^{-1}]$ is the linear dose coefficient representing the probability that a DSB is caused by a single event while β $[Gy^{-2}]$ is the quadratic dose coefficient representing the probability that a DSB is caused by two individual events. This last and more accurate relationship can interpolate either Equation (1.10) and Equation (1.11).

Dose Fractionation

The amount of radiation used in photon radiation therapy is measured in grays (Gy), and varies depending on the type and stage of cancer being treated. A typical dose for a whole treatment of a solid tumor is around 60 Gy, which is fractionated on average in 30 sessions of 2 Gy each. Dose fractionation is of primary importance for mainly two reasons. The first reason is cellular oxygenation. As shown in figure 1.5, indeed, cellular oxygenation is of great importance in defining cellular survivability, since the killing of tumor cells in oxygenated regions can be up to three times greater than in poorly oxygenated conditions.

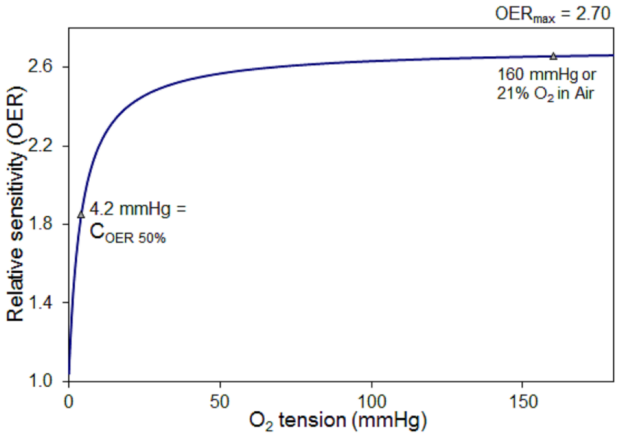

Figure 1.5. Oxygen Enhancement Ratio

This influence is described by the parameter oxygen enhancement ratio (OER) which is the ratio between the dose required to induce a given biological effect (D) and the dose required to induce the same effect in a fully oxygenated tissue at standard air pressure. (D_0).

$$OER = \frac{D}{D_0} \tag{1.13}$$

Therefore, by leaving cells time to re-oxygenate, each irradiation fraction will be more effective.

The other reason that makes it necessary to deliver the overall dose in fractions is to reduce as much as possible the possibility of inducing damages to healthy tissues. As shown in Figure 1.6, which represents the dose-responce curves for tumor and healthy tissue, it would be impossible to deliver the total therapeutic dose necessary

for tumor control in a single fraction without inevitably causing damages to nearby healthy cells.

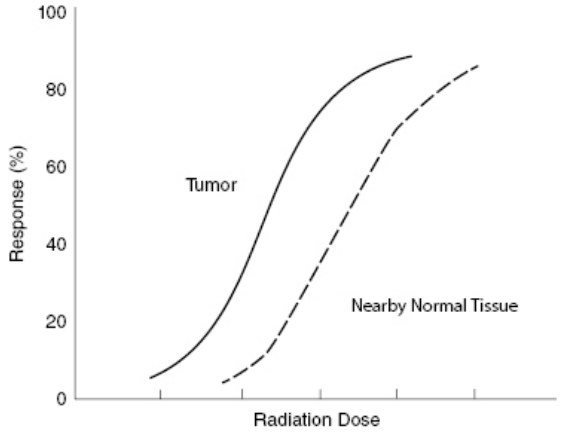

Figure 1.6. Tumor and normal tissue dose–response curves

Instead, dose fractionation allows healthy cells to recover almost completely between each irradiation. Therefore, every fraction of dose results in a low probability of inducing damages, and before the following irradiation is delivered the healthy cell can be considered fully recovered. The resulting survival curves for healthy cells, showing the effect of damage repair over fractions, are showed in Figure 1.7.

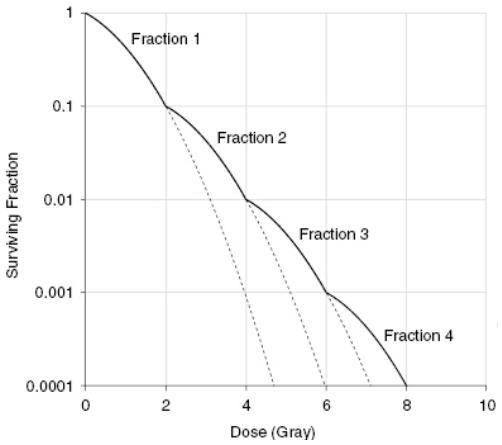

Figure 1.7. Survival curves with dose fractionation

1.4 Radiation Therapy LINAC

Nowadays, medical electron linear accelerators are the most employed devices in external beam radiation therapy. The working principles for modern linacs were proposed by Gustav Ising in 1924, and the first working machine was made in 1928 by Rolf Widerøe at the RWTH Aachen University. However, linac-based radiation

therapy dates back to several years later with the first patient to be treated in 1953 at the Hammersmith Hospital, London, with an 8 MV machine made by Metropolitan-Vickers.
The electron linear accelerator uses microwave technology to accelerate electrons in a *waveguide* consisting of a series of cavities, each included between two irises (see Figure 1.8 [16]). Irises are placed inside the waveguide to slow-down the phase velocity to be phased with the electron bunches.

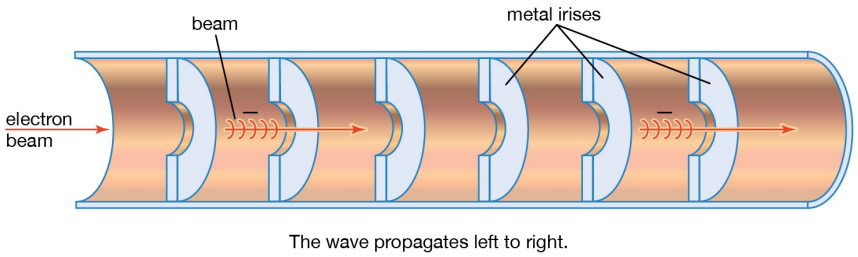

Figure 1.8. Waveguide for a linear electron accelerator

Electrons are produced by the so called *electron-gun*. In this component, electrons are produced by thermo-ionic effect as a continuous beam. This continuous beam is sent through a sequence of non-uniform cavities (i.e. the *buncher* section) to focus electrons in bunches and be phased with the acceleration electric field. Typically, one third of the continuous beam is collected and accelerated. For the acceleration of electrons, waveguides can operate in Standing Wave (SW) or Travelling Wave (TW) mode (see Figure 1.9 [17]). A standing wave is composed by moving forward and backwards electric field waves, reflected by the waveguide walls. The resulting wave is a wave oscillating in time but whose peak amplitude profile does not move in space, as a violin vibrating string. The peak amplitude of the wave oscillations at a given point in space is constant with time, and the oscillations at different points are in phase. For this mechanism to occur, one cavity out of two must possess a null electric field. These zero field cavities couple the microwave power among the cavities, but they are not providing acceleration.
A stationary wave is described by the following equation

$$y = 2Asin\left(\frac{2\pi x}{\lambda}\right)cos(\omega t) \tag{1.14}$$

where A is the wave amplitude, ω is the angular frequency and λ is the wavelength. Variables x and t represent space and time respectively. At points which are even multiples of a quarter wavelength, called the nodes, the amplitude is zero, whereas

at points which are odd multiples of a quarter wavelength, called the anti-nodes, the amplitude is maximum. The distance between two consecutive nodes or anti-nodes is $\lambda/2$.

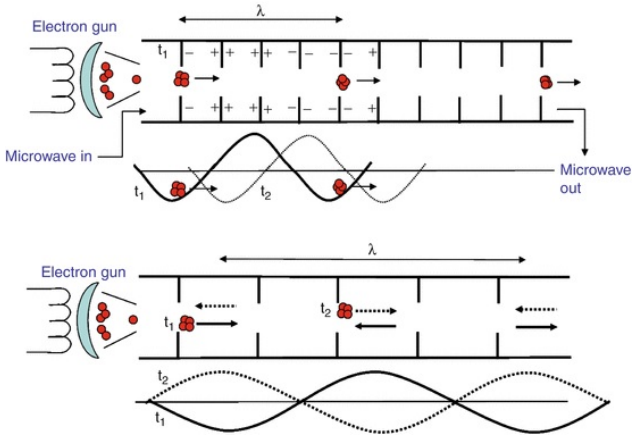

Figure 1.9. TW and SW waveguide structures

Differently from a standing wave, a travelling wave is a periodic function of one-dimensional space moving with constant speed. Its movement can be imagined as a surfer, placed on a wave maximum, surfing the wave in a given direction. For a travelling wave, two possible wave structures are possibile. In the $\pi/2$ structure, one cavity out of four contains an electron bunch, whereas in the $2\pi/3$ structure the ratio is one cavity out of free. It is important to know that in a TW waveguide the field waves are not reflected on the closing walls, but they are absorbed in a load at the exit. In general, travelling wave waveguides can grant a wider bandwidth, so a less frequency-variation susceptible system.
The total input power of the microwave, in both working structures, is spent as

$$P_0 = P_{Cu} + P_L + P_E \tag{1.15}$$

where P_{Cu} is the power dissipated in copper, P_L is the power reflected by the SW, or dissipated in the load by the TW, and P_E is the power given to the electron beam. In order to either contain the temperature rise in the system and accomodate the dose rate to the prescribed one, radiation therapy linacs must work in a pulsed mode with a duty factor of 0.001. This pulse frequency is about 100-200 Hz and superimposes to the microwave frequency that is around 3 GHz.
A schematic diagram of a linear accelerator is reported in Figure 1.10 [18]. Inside the machine head, in addition to the electron bending magnet, there are the physical shield, the bremsstrahlung target, a first set of heavy metal fixed collimators, the flattening filter and a second set of movable collimators, plus a transmission ioniza-

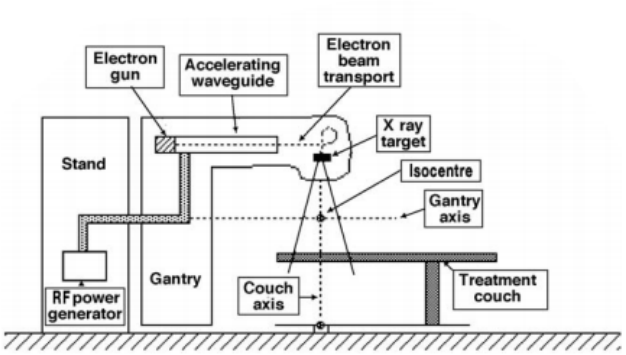

Figure 1.10. Linac Schematic Diagram

tion chamber for beam monitoring. In the bremsstrahlung target, electromagnetic radiation is produced by the deceleration of electrons in the target. Tipically, this is made of lead or tungsten in order to maximise the x-ray production, which depends on Z^2. Then, x-rays are modulated and shaped for beam delivery.

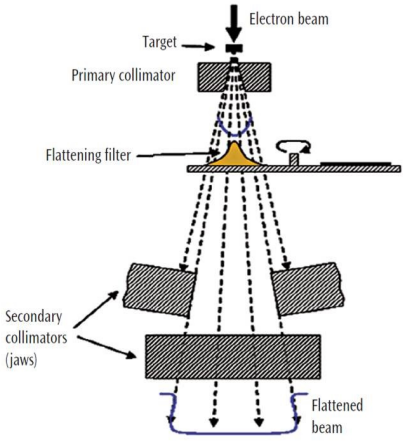

Figure 1.11. Linac Head Schematic Diagram

The flattening filter is a gaussian-shaped filter necessary to obtain a uniform dose profile. Indeed, when x-rays are generated in the bremsstrahlung target, the beam is forward peaked with respect to the original electron beam direction. Therefore, the x-ray dose would approximate a gaussian. The presence of the gaussian flattening filter can then attenuate the beam where it is more intense and with a lower efficiency where it is not, so that the resulting effect is a uniform dose profile. The uniformed beam passes finally through the second collimation stage, where movable collimators are used to define the treatment field, it is measured by the ionization chamber and it's delivered to the patient. It is important to note that most of deep-seated tumors can be treated with x-ray beams of 4-6 MV, but, thick sections of the human body, as the pelvis, must be treated with higher energies, up to 20 MV. In fact, as shown in

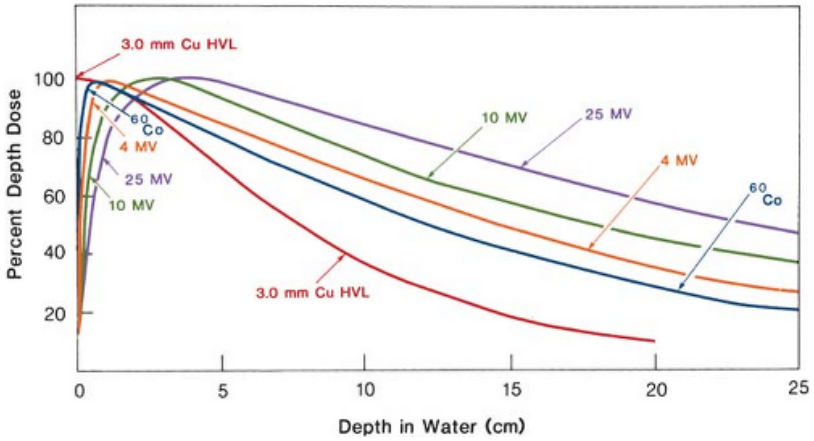

Figure 1.12. Depth-dose profiles

Figure 1.12, the depth-dose distribution for high energy beams shows a deeper dose maximum in tissue, thanks to secondary electron build-up.

Chapter 2

Elements of Neutron Physics

The neutron is a sub-atomic particle with no electric charge and rest mass equal to $1.67493 \cdot 10^{-27}$ kg. Together with protons, neutrons are the constituent of atom nuclei. The neutron discovery dates back to 1932 by James Chadwick (University of Cambridge, United Kingdom) and led him to the award of the Nobel Prize in Physics in 1935.

Neutrons can be produced and emitted as radiation by several processes. One of these processes, and the most important from the present work, is the photoneutron production. Neutrons can be producted by means of a (γ, n) reaction when a sufficiently energetic photon interacts with an appropriate target material. One example is the Deuterium reaction (2.1)

$$ {}^{2}_{1}\mathrm{H} + h\nu \rightarrow {}^{1}_{1}\mathrm{H} + {}^{1}_{0}\mathrm{n} \qquad (Q = -2.226 MeV) \tag{2.1} $$

To make the reaction possible, a photon energy of at least the negative of the Q value is required. For gamma-ray energies above this value, the corresponding neutron energy can be calculated as follows [19]

$$ E_n(\theta) \cong \frac{M(E_\gamma) + Q}{m + M} + \frac{E_\gamma \sqrt{(2mM)(m + M)(E_\gamma + Q)}}{(m + M)^2} \, cos(\theta) \tag{2.2} $$

where θ is the angle between the photon and neutron directions, E_γ is the gamma ray energy, m and M are the neutron and recoil nucleus mass$\times c^2$ respectively. It is important to note that the angle variation between 0 and π broadens the neutron energy spectrum of a few percent only, so, if photons are considered monoenergetic, neutrons can be considered also nearly monoenergetic.

2.1 Neutron Interaction with Matter

Since neutrons carry no charge, they cannot interact with matter by means of the coulomb force and they can travel long straight distances in matter without interacting. Neutrons eventually interact with nuclei of the absorbing material either by scattering or nuclear reactions. The relative probability of each interaction mode changes abruptly with neutron energy.
The term *neutron energy*, or neutron temperature, is used to indicate a free neutron's kinetic energy, usually given in electron-volts (eV). To make it simple, neutrons can be divided in three energy groups: *thermal neutrons* for energies around 0.025 eV, *epithermal neutrons* up to 0.5 eV and *fast neutrons* above 0.5 eV. Thermal neutrons, in particular, are so-called for their peculiarity of being in thermal equilibrium with the surrounding medium at a certain temperature, following a Maxwellian distribution in energy where 0.025 eV is the most probable energy at a temperature of 20°C:

$$P(E)dE = \frac{2}{\sqrt{\pi}} e^{-\frac{E}{KT}} \left(\frac{E}{KT}\right)^{\frac{1}{2}} \frac{dE}{KT} \tag{2.3}$$

where

- P(E) is the the number of neutrons of energy E per unit energy interval;
- E is the neutron energy;
- T is the absolute medium temperature;
- K is the Boltzmann constant ($K = 8.617333262 \times 10^{-5}\, eV \cdot K^{-1}$).

Thermal neutrons interact with matter mainly by nuclear reactions. In particular, the most accredited model is the so called "compound nucleus model", which assumes that the incident particle energy plus its binding energy are distributed to all nucleons of the formed compound nucleus, so that its excitation energy is

$$E^* = E_x + E_B - E_c \tag{2.4}$$

where E_c is its kinetic energy, E_x the neutron energy and E_B the neutron binding energy. This way, if a sufficient part of the excitation energy is released to one or more nucleons, they can overcome the energetic barrier and be emitted, concluding the reaction. The total Q *value* of the reaction $A(x, y)B$ is:

$$\Delta E = (m_A + m_x - m_B - m_y) \cdot c^2 \tag{2.5}$$

Differently from slow neutrons, fast neutrons have a lower interaction probability for nuclear reactions. Their main interaction mode is the elastic scattering. In elastic scattering, a neutrons collides with a nucleus of the target material, transfers part of its kinetic energy and deflects to change its original direction. In this process, either the total kinetic energy and linear momentum are conserved. The equation that describes the kinetic energy transferred from the neutron to the target nucleus is

$$\Delta E = E_{neutron} \frac{4\, m_{target}\, m_{neutron}}{(m_{target} + m_{neutron})^2}\, cos^2(\theta) \tag{2.6}$$

with θ being the diffusion angle. If the neutron kinetic energy is higher than the first excited state gap of the target nucleus, the target can also be left in such excited state, from which de-excites emitting a secondary γ ray (inelastic scattering).

2.1.1 Neutron Cross Section

For neutrons of a fixed energy, the interaction probability is a constant called *cross section*, σ. In particular, it is defined as the area for a nucleus that, when impinged by a neutron, gives interaction. Its unit of measure is then a surface quantity, the *barn*, defined as $10^{-24}\, cm^2$. When multiplied by the atomic density of the target material N, the cross section is converted to the *macroscopic cross section*, $\Sigma\, [cm^{-1}]$. This macroscopic cross section gets the same physical meaning of the linear attenuation coefficient for photons, that is the interaction probability per unit thickness of the target material. However, since Σ is specific for every interaction process, for a neutron of a given energy the total cross section will be defined as

$$\Sigma_{tot} = \Sigma_{scattering} + \Sigma_{rad.capture} + ... \tag{2.7}$$

and the corresponding attenuation relation is written

$$I = I_0\, e^{-\Sigma_{tot}} \tag{2.8}$$

Finally, in conjunction with the neutron flux, the macroscopic cross section enables also the calculation of the *reaction rate density*, that is the number of reaction per unit time and volume.

$$r.r. = \phi \cdot \Sigma \qquad [cm^{-3} s^{-1}] \tag{2.9}$$

2.2 Neutron Detection

Neutrons are neutral particles and thus do not produce direct ionization in matter. For this reason, they are generally detected by the effects that secondary charged particles produce. In case of slow neutrons, suitable nuclear reactions can be employed for the detection of the product charged particles, while fast neutrons are mainly detected from the ionization effects caused by recoil nuclei.
Neutron detectors can be divided in two main categories:

- Active detectors give an immediate responce and data can be collected in real time.
- Passive detectors store the information to be read after a specific analysis, that can be either short or long, simple or not.

The main active detector used in the present work was the LUPIN-BF3 NP detector distributed by ELSE NUCLEAR srl, Via Dante Alighieri 16, 21052 Busto Arsizio (VA). As passive detectors, bubble dosimeters have been used for comparison.

2.2.1 The LUPIN BF3-NP Detector

The original Long interval, Ultra-wide dynamic Pile-up free Neutron rem counter (LUPIN) is a detector developed for radiation protection purposes, specifically conceived for applications in pulsed neutron fields [20]. The LUPIN detector, due to

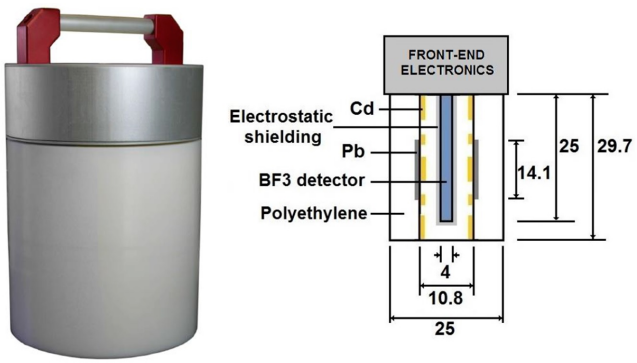

Figure 2.1. The LUPIN detector (on the left) and a schematic drawing of the most relevant components (on the right)

its innovative working principle, overcomes several rem counters limitations and meets four of the requirements needed by an ideal survey meter for pulsed neutron fields (PNF):

- It can withstand very high instantaneous neutron fluxes with values of H*(10) up to 16 nSv per burst without showing any saturation [12];

– It has a high sensitivity, comparable to that of commercially available rem counters;

– It has a measurement capability ranging over many orders of neutron burst intensity, from single neutron interaction up to a reaction rate of $2 \cdot 10^{-6} s^{-1}$ [21];

– It can efficiently reject the photon contribution that accompanies the neutron field [22].

However, to further improve the performance in PNFs, a new version of the detector, LUPIN-II, was also developed. The LUPIN-II detector is a rem counter consisting of a cylindrical BF_3 proportional counter - which working principle will be explained below - of 25 mm diameter and 150 mm length (Centronics 15EB/20/25SS) with gas pressure of 200 mmHg placed at the center of a cylindrical polyethylene moderator of 25 cm diameter with lead and cadmium inserts. An aluminium electrostatic shielding of 1.5 mm thickness encloses the detector and two polyethylene inserts, which are used to fill the void around the detector. The operating voltage is 1180 V [12] [21]. The LUPIN-II front-end electronics consists of a current to voltage Logarithmic Amplifier, whose output signal is acquired via an analog-to-digital converter (ADC) with a conversion rate of 10 MSamples/s and processed with a *LabVIEW* program. The

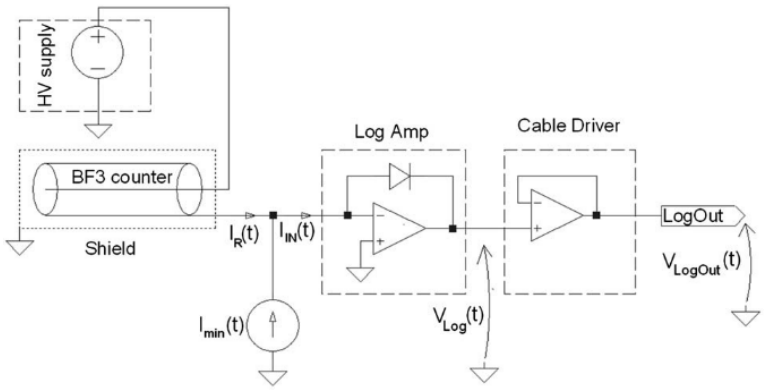

Figure 2.2. General scheme of the LUPIN detector

idea of the analysis software is the following: the voltage signal is converted back into a current signal and integrated over a time that can be set by the user. This allows measuring the generated charge even if the neutron interactions pile up [12]. The result of this calculation represents the total charge generated in BF_3 by the neutron interactions. This quantity, divided by the average charge expected by a single neutron interaction, represents the number of neutron interactions occurring during the integration time [21].

The particular design of the LUPIN-II detector, together with its advanced electronics, showed very good results compared with respect to other rem counters, including LUPIN. The results of an intercomparison made in 2014 at the Helmholtz Zentrum Berlin (HZB), widely discussed in reference [12], are reported for example in figure 2.3. As it is shown, the LUPIN-II rem counter was able to get a linear response up to 150 nSv/burst, with only a 20 % underestimation at 470 nSv/burst, while the other detectors soon failed by saturation. Another main improvement in LUPIN-II version

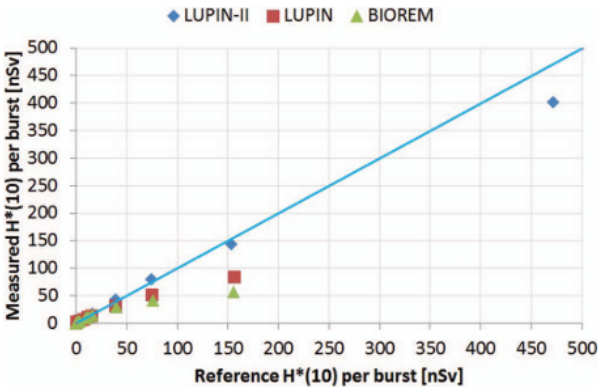

Figure 2.3. LUPIN, LUPIN-II, and BIOREM response (measured vs expected H*(10) per burst) at HZB

is the photon rejection in high energy mixed fields, that is for example the radiation field around a medical linear accelerator. The new rejection technique, called "derivative technique", digitally reverts the LUPIN-II into a detector operating in pulse mode, but the threshold is set on the derivative of the current signal, defined as [12]

$$\frac{d(I_n)}{dt} = \frac{1}{2\delta t}(I_{n-1} - I_{n-1}) \tag{2.10}$$

where I_{n-1},I_n, and I_{n+1} are the current values and δt is the time step (100 ns). In a steady photon field, the sudden increase in signal caused by a neutron interaction allows the derivative technique to effectively discriminate a neutron interaction from the photon background. As shown in figure 2.4 [12], the photon peak can be used as a trigger for the acquisition, while the charge integration starts with a 5 μs delay, thus excluding the photon contribution.

Nevertheless, a problem rises when a pulsed photon field is present. In this case, each photon burst will be treated as a trigger signal and included in the total count. For this reason, a mathematical correction must be accounted for a correct photon rejection. For each measure acquired by the LUPIN detector, the total ambient dose was reverted in raw counts by the conversion coefficient from neutron interactions to H*(10) (i.e. 1.85 nSv^{-1}). Also, the total number of photon pulses during the

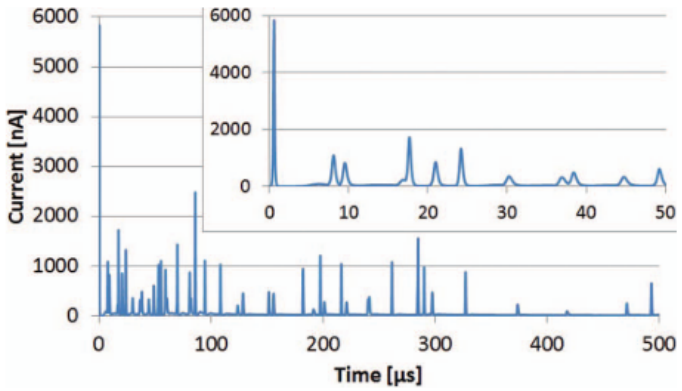

Figure 2.4. Signal acquired at PSI in a neutron field characterized by an intense photon background. The zoom of the first $50\mu s$ shows the prompt photon peak.

irradiation was calculated as the irradiation time multiplied by the pulse frequency of the machine, which was reported by the diagnosys software. Then, the total number of pulses was subtracted from the original count and the result was converted back in terms of H*(10).

Working Principle of a Proportional (BF3) Tube

Similarly to Geiger-Muller counters, the proportional gas counter is a gas-filled detector that relies on charge multiplication in order to amplify the output signal. When a ionization event happens inside the gas volume, several ion-electron pairs are produced. By applying a sufficiently high electric field, ions and electrons are pushed in opposite directions toward the cathode and the anode respectively. To make it simple,

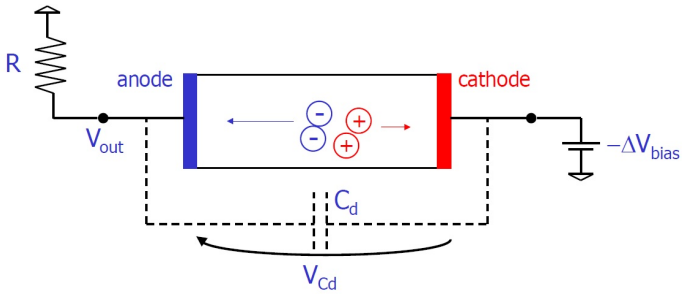

Figure 2.5. Gas Counter Readout Electronics

if we connect the cathode to a $-V_{bias}$ generator and the anode to ground through a large resistor, as shown in Figure 2.5, we've basically created an RC network. In case the capacitor has 0 initial voltage, it will charge to ΔV_{bias}. As an ion pair is produced, electrons and ions start moving inducing a charge variation Q on the capacitor plates. Thus, the capacitor gains an extra charge ΔV_{cd} (negative). Such voltage drop can be

read as ΔV_{out}.

$$\Delta V = \frac{Q}{C_d} \tag{2.11}$$

If the applied electric field is sufficiently high, electrons can be accelerated up to energies greater than the ionization energy of the filling gas, thus producing more ion-electron pairs and so on. In typical gases at room pressure, the process threshold is about 10^6 V·m^{-1}. The avalanche terminates when all free electrons are collected at the anode. In cylindrical geometry, the electric field can be expressed as a function of radius, r

$$\epsilon(r) = \frac{V}{r\, ln(\frac{b}{a})} \tag{2.12}$$

where

- V is the applied voltage between anode and cathode
- a is the anode wire radius
- b is the cathode *inner* radius.

The total charge Q, generated by n_0 original charged pairs, is

$$Q = n_0 e M \tag{2.13}$$

where M is the *gas multiplication factor*, dependent on pressure p, and defined as [19]

$$ln(M) = \frac{V}{ln(\frac{b}{a})} \cdot \frac{ln2}{\Delta V} \left(ln \frac{V}{p \cdot a \cdot ln(\frac{b}{a})} - ln(K) \right) \tag{2.14}$$

Nevertheless, when dealing with neutron detection, several other factors must be considered for the proper coversion of neutrons in detectable products. First of all, the neutron interaction cross section for the reaction to occurr must be as large as possible in order to minimize the detector dimensions, and the reaction Q value should be large enough to discriminate the nuclear reaction products from the possible gamma field using simple amplitude discrimination. Also, the secondary particles range must be considered, expecially for gas detectors, since particles can travel a long path in gases and may not be stopped inside the detector active volume. All considered, the probably most popular reaction for the conversion of thermal neutrons is the $^{10}B(n, \alpha)$ reaction

$$^{10}_{5}\mathrm{B} + ^{1}_{0}\mathrm{n} \rightarrow \begin{cases} ^{7}_{3}\mathrm{Li} + ^{4}_{2}\alpha & Q = 2.792\ MeV \\ ^{7}_{3}\mathrm{Li}^{*} + ^{4}_{2}\alpha & Q = 2.310\ MeV \end{cases} \tag{2.15}$$

with a relative branching of 6% and 94% respectively and a cross section for thermal neutrons of 3840 barns. When dealing with fast neutrons, instead, the detection efficiency can be somewhat increased by surrounding the detector with a scattering hydrogen-based material, in order to slow-down fast neutrons into the thermal region before reaching the proportial counter. The filling gas used for such type of detectors is ^{10}B 96% enriched BF_3, eventually mixed with Argon. In common with most proportional counters, BF_3 counters are cylindrical. Aluminium is often chosen as the cathode material for its low neutron absorbtion cross section. Gas pressure can range from 100 to 600 torr, with cathode diameter up to 15 cm and anode radius below $0,1$ mm. The operating voltage is $2000 - 3000$ V, and gas multiplication is in the order of $100 - 500$ [19]. In case of neutron counters, it is important to note that since the Q value of the (n, α) reaction is so large compared to the neutron kinetic energy, it is basically impossible to extract any information about the original neutron energy. However, for the same reason, the linear momentum of the coming neutron is totally negligible, and the two particles can be assumed as emitted in opposite directions. Individual energies can be computed by simple conservation of energy and momentum, resulting in

$$E_{Li} = 0.84\, MeV \qquad and \qquad E_{\alpha} = 1.47\, MeV \tag{2.16}$$

for the excited lithium case. Since particles are emitted with high energy in opposite direction, *wall effect* must be considered. Once the size of the detector is not large enough to fully stop both particles, expecially for reactions that happens near the detector walls, the escaping particle cannot deposit its full energy inside the active volume, resulting in a lower pulse height in the differential spectrum, as shown in Figure 2.6.

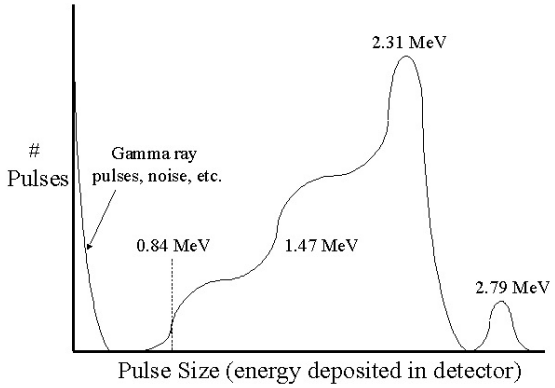

Figure 2.6. Expected pulse height spectrum from a BF_3 proportional counter

2.2.2 Bubble Detectors

A unique type of radiation detector particularly useful in neutron detection is the so called *superheated drop detector*, or "bubble detector". It is based on a suspension of super-heated freon droplets within an inert and immiscible matrix. Tipically, a bubble detector is made of a plastic tube containing few cubic centimeters of the gel (or polymeric) matrix and tens of thousands droplets of 100 μm or less in a super-heated state [19]. A fluid is said to be in a superheated state when it's above its boiling temperature, but, for some reason, still in a liquid state. This particular state is considered meta-stable, and a sufficient perturbation to the system leads to vaporization. When neutrons interact within the matrix, charged particles are produced and their deposition of energy along the track is the trigger that causes the local vaporization of the droplets and their nucleation into visible bubbles, fixed in the matrix for the successive count.

Figure 2.7. A bubble detector personal neutron dosimeter

It is important to note that because of the threshold energy required to trigger the state transition, only fast neutrons can produce recoil nuclei with sufficient energy. For thermal neutrons, bubble detectors can be made sensitive by incorporating an element that causes a neutron-induced nuclear reaction, such as $^{35}Cl(n,p)^{35}S$, producing high energy density recoil particles. For the same reason, almost all bubble detectors are insensitive to gamma fields, thus making them perfect for mixel fields environments.
For dose evaluation, the total number of bubbles generated is divided by the specific dosimeter sensitivity (in $bubbles\ \mu Sv^{-1}$) given by the producer. Bubbles can be counter either by eye or by automated systems like acoustic sensors or bubble counting algorithms. After counting, these dosimeters are reusable. To restore their properties, it is sufficient to screw the cap until bubbles are compressed again.

Two types of bubble detectors were employed for this work:

- Bubble Detector Thermal (BDT), for thermal neutrons detection;
- Bubble Detector - Personal Neutron Dosimeter (BD-PND), for fast neutrons detection, in the interval between 200 keV and 15 MeV.

Together with bubble detectors, a special dosimetric phantom was used.

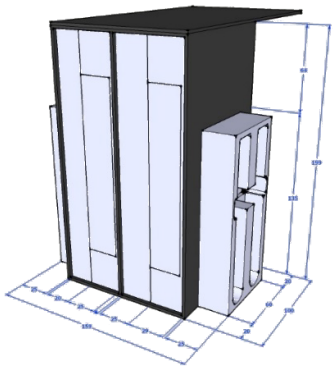

Figure 2.8. Dosimetric phantom

This is characterized by a parallelepiped shape, formed by polyethilene modules and covered by a 2 mm thick *Quick Boron* layer. Inside each polyethilene module, there is a cavity for the insertion of bubble detectors. *Quick Boron* is a mixed material composed by boron carbide (B_4C), resins and carbon fiber, which function is to stop thermal neutrons by capture in ^{10}B. The polyethylene matrix, instead, is meant to slowdown fast and epithermal neutrons to thermal energy. As a result, neutrons that are already at thermal energy get absorbed by cadmium, while fast and epithermal neutrons are slowed down and can be revealed as thermal inside the phantom.
Therefore, it was possible either to better discriminate the neutron components and to study the attenuation of fast neutrons in a matrix that is sufficiently similar to the human body.

Chapter 3

Measurement of Neutron H*(10) from Linear Accelators

The neutron dose around medical linear accelerators can depend on several factors, including (but not limited to):

- machine producer and model;
- beam energy;
- beam size;
- presence of scattering materials (including the patient bed) near the machine.

To get the most exhaustive data set possible, the ambient dose equivalent, H*(10), was measured with the LUPIN detector around linear accelerators in several conditions and all the experiments will be reported in the present chapter. In particular, different configurations of beam energy, size, collimator position, detector position and beam type were measured and compared. Measurements were acquired at three different hospitals, housing two different machines. This variety made it possible to compare the results either between different machines, to assess the differences, and identical machines, which are expected to provide almost identical results.
To evaluate the performance of the LUPIN detector relatively to other instruments, measurements were also acquired according to availability with other detectors including traditional rem counters (Wendy, Berthold, NRD) and bubble dosimeters. Also, a montecarlo simulation was developed specifically for one linear accelerator.
Finally, a few treatment plans have been tested with both linac models, based on real treatment plans delivered to patients.

3.1 Ospedale di Circolo e Fondazione Macchi (VA)

The "Ospedale di Circolo e Fondazione Macchi - Azienda Socio Sanitaria Territoriale (ASST) dei Sette Laghi" hospital, Viale Luigi Borri 57, 21100 Varese (IT), houses several linear accelerators for radiation therapy purposes. The one that was used for this work is the DHX Clinac by Varian Medical Systems (Palo Alto, California, U.S.). It can operate with electrons of 6, 12, 16 and 20 MeV and photons of 6 and 18 MV. The collimation jaws can size fields from 3x3 cm^2 to 30x30 cm^2 and, for electrons, different applicators are available for beam focusing. Finally, an absorbing wedge can be employed for beam shaping. This is basically an additional heavy metal triangular-shaped absorber used for breast x-ray radiation therapy (XRT) in particular circumstances.
The pulse frequency of the accelerator, measured with a Pico Technology Oscilloscope connected to the LUPIN detector, results to be 360 Hz for 6 MV photons (see Figure 3.1) and 180 Hz for 18 MV photons. The same pulse frequency was also confirmed by the diagnosis software of the machine.

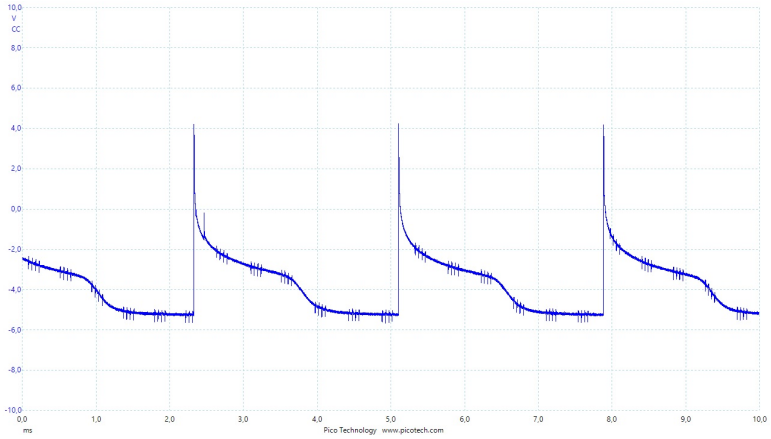

Figure 3.1. Varian DHX Clinac Voltage Output

During all the experiments, a dosimetric phantom made of polystyrene (solid water) of 30x30 cm^2 area and 20 cm height was placed in-field on the patient bed at a source to skin distance (SSD) of 100 cm to simulate the human chest.

3.1.1 Measurements with LUPIN Detector

Irradiation with photon beams

The first experiment was made to characterize the secondary neutron ambient dose equivalent from a photon beam irradiation with different parameters of the primary beam. The detectors that were used are the LUPIN and the NRD rem counters.

The machine was used in clinical mode by varying the field size from 3x3 cm^2 to 20x20 cm^2 and the photon energy from 6 to 18 MV. For each combination of field and energy, the detectors were placed on the patient bed at 50, 100, 150 and 200 cm from the isocenter.
The machine was set with the following parameters:

- Gantry angle: 0°
- Source-to-skin distance (SSD): 100 cm
- Irradiation time: 20 s
- Monitor Units: 600 MU per minute (1 MU = 1 cGy in calibration conditions)
- Detector position: on patient bed

Results are reported in Table 3.2, 3.3 and Table 3.4 and show the neutron dose expressed as H*(10), H*(10) per Gy and H*(10) per MU for LUPIN and NRD.

Irradiation with electron beams

The second experiment was made with electron therapy beams. The aim of the experiment was either to assess the neutron dose related to electron therapy and to compare the neutron production between photon and electron beams.
The machine was again used in clinical mode and it was equipped with different applicators, which define the field size.
Electron energy was set from 6 to 20 MV and the LUPIN detector was placed in the same positions as the previous experiment.
The machine was set with the following parameters:

- Gantry angle: 0°
- SSD: 100 cm
- Irradiation time: 20 s
- Monitor Units: 600 MU per minute (1 MU = 1 cGy in calibration conditions)
- Detector position: on patient bed

Results, expressed in terms of H*(10), are reported in Table 3.5.[1].

[1]Results for 6 and 9 MeV at 150 and 200 cm distance are omitted

Simulation of a real therapy plan

The last experiment was made to simulate a real XRT therapy plan. The main difference from the previous experiments is that in real therapy plans the machine gantry is not fixed in a given position, but it rotates around the body vertical axis to maximize the delivered dose in the tumor region while giving the lowest possible dose to the surrounding tissue. For the same reason, also the repetition rate (or pulse ratio) of the machine may vary during irradiation.
The working parameters of the simulated plan were the following:

- Beam type: X-rays
- Tumor region: Breast
- Repetition rate: 300 MU/Min
- SSD: 100 cm
- Photon energy: 6 MV
- LUPIN position: on bed, 50 cm from isocenter

Results, reported for each fraction in terms of H*(10), are reported in Table 3.1. The overall neutron ambient dose equivalent that was registered is 488 μSv.

Table 3.1. Neutron H*(10) from Varian DHX Clinac delivering a real therapy plan, measured by LUPIN

E (MV)	D (cm)	Fraction	Time (s)	H*(10) (μSv)
6	50	1.1	0.26	12
6	50	1.2	0.37	58
6	50	2.1	0.21	7
6	50	2.2	0.41	47
6	50	3.1	0.1	5
6	50	3.2	0.25	48
6	50	4.1	0.32	87
6	50	4.2	0.11	8
6	50	5.1	0.33	66
6	50	5.2	0.14	7
6	50	6.1	0.36	44
6	50	6.2	0.23	18
6	50	7.1	0.27	39
6	50	7.2	0.32	42

Table 3.2. Neutron H*(10) from Varian DHX Clinac operating with photon beams, measured by LUPIN and NRD

E (MV)	D (cm)	jaw X (cm)	jaw Y (cm)	wedge (deg)	LUPIN (μSv)	NRD (μSv)
18	50	3	3		2473	226
18	50	10	10		2501	216
18	50	20	20		2512	212
18	50	3	3	60	2480	221
18	50	10	10	60	2517	211
18	50	20	20	60	2554	199
18	100	3	3		2352	244
18	100	10	10		2352	246
18	100	20	20		2341	246
18	150	3	3		2214	
18	150	10	10		2209	
18	150	20	20		2191	
18	200	3	3		2100	284
18	200	10	10		2093	284
18	200	20	20		2071	282
6	50	3	3		10	26
6	50	10	10		97	25
6	50	20	20		440	26
6	50	3	3	60	10	25
6	50	10	10	60	106	26
6	50	20	20	60	366	25
6	100	3	3		1	24
6	100	10	10		8	25
6	100	20	20		60	25
6	150	3	3		0	
6	150	10	10		1	
6	150	20	20		13	
6	200	3	3		0	0.5
6	200	10	10		0	24
6	200	20	20		3	25

Table 3.3. Neutron H*(10) per delivered Gy from Varian DHX Clinac operating with photon beams, measured by LUPIN and NRD

E (MV)	D (cm)	jaw X (cm)	jaw Y (cm)	wedge (deg)	LUPIN (μSv/Gy)	NRD (μSv/Gy)
18	50	3	3		1527	140
18	50	10	10		1316	114
18	50	20	20		1214	102
18	50	3	3	60	3572	318
18	50	10	10	60	3091	259
18	50	20	20	60	2879	224
18	100	3	3		1452	151
18	100	10	10		1238	129
18	100	20	20		1131	119
18	150	3	3		1367	
18	150	10	10		1163	
18	150	20	20		1058	
18	200	3	3		1296	175
18	200	10	10		1102	149
18	200	20	20		1001	136
6	50	3	3		6	15
6	50	10	10		49	13
6	50	20	20		209	12
6	50	3	3	60	14	34
6	50	10	10	60	131	32
6	50	20	20	60	423	29
6	100	3	3		1	13
6	100	10	10		4	13
6	100	20	20		28	12
6	150	3	3		0	
6	150	10	10		1	
6	150	20	20		6	
6	200	3	3		0	0
6	200	10	10		0	12
6	200	20	20		1	12

Table 3.4. Neutron H*(10) per MU from Varian DHX Clinac operating with photon beams, measured by LUPIN and NRD

E (MV)	D (cm)	jaw X (cm)	jaw Y (cm)	wedge (deg)	LUPIN (μSv/MU)	NRD (μSv/MU)
18	50	3	3		12.37	1.13
18	50	10	10		12.51	1.08
18	50	20	20		12.56	1.06
18	50	3	3	60	12.40	1.11
18	50	10	10	60	12.59	1.06
18	50	20	20	60	12.77	1.00
18	100	3	3		11.76	1.22
18	100	10	10		11.76	1.23
18	100	20	20		11.71	1.23
18	150	3	3		11.07	
18	150	10	10		11.05	
18	150	20	20		10.96	
18	200	3	3		10.50	1.42
18	200	10	10		10.47	1.42
18	200	20	20		10.36	1.41
6	50	3	3		0.05	0.13
6	50	10	10		0.49	0.13
6	50	20	20		2.20	0.13
6	50	3	3	60	0.05	0.13
6	50	10	10	60	0.53	0.13
6	50	20	20	60	1.83	0.13
6	100	3	3		0.01	0.12
6	100	10	10		0.04	0.13
6	100	20	20		0.30	0.13
6	150	3	3		0.00	
6	150	10	10		0.01	
6	150	20	20		0.07	
6	200	3	3		0.00	0.00
6	200	10	10		0.00	0.12
6	200	20	20		0.02	0.13

Table 3.5. Neutron H*(10), H*(10) per Gy and H*(10) per MU from Varian DHX Clinac operating with electron beams, measured by LUPIN

E (MeV)	D (cm)	jaw X (cm)	jaw Y (cm)	Applicator	H*(10) (μSv)	μSv/Gy	μSv/MU
6	50	20	20	A6	15	7.8	0.08
6	50	20	20	A10	14	7.0	0.07
6	50	30	30	A25	18	9.1	0.09
9	50	20	20	A6	26	13.3	0.13
9	50	20	20	A10	25	12.5	0.13
9	50	30	30	A25	27	14.1	0.14
12	50	11	11	A6	21	10.8	0.11
12	50	14	14	A10	26	13.0	0.13
12	50	30	30	A25	47	24.9	0.24
16	50	11	11	A6	70	36.3	0.35
16	50	14	14	A10	77	38.5	0.39
16	50	28	28	A25	85	45.5	0.43
20	50	11	11	A6	146	75.5	0.73
20	50	14	14	A10	156	78.0	0.78
20	50	27	27	A25	139	74.8	0.70
6	100	20	20	A6	2	1.0	0.01
6	100	20	20	A10	2	1.0	0.01
6	100	30	30	A25	3	1.5	0.02
9	100	20	20	A6	5	2.6	0.03
9	100	20	20	A10	4	2.0	0.02
9	100	30	30	A25	5	2.6	0.03
12	100	11	11	A6	6	3.1	0.03
12	100	14	14	A10	7	3.5	0.04
12	100	30	30	A25	10	5.3	0.05
16	100	11	11	A6	28	14.5	0.14
16	100	14	14	A10	28	14.0	0.14
16	100	28	28	A25	24	12.8	0.12
20	100	11	11	A6	64	33.1	0.32
20	100	14	14	A10	62	31.0	0.31
20	100	27	27	A25	48	25.8	0.24
12	150	11	11	A6	3	1.5	0.02
12	150	14	14	A10	3	1.5	0.02
12	150	30	30	A25	4	2.1	0.02
16	150	11	11	A6	18	9.3	0.09
16	150	14	14	A10	17	8.5	0.09
16	150	28	28	A25	13	7.0	0.07
20	150	11	11	A6	41	21.2	0.21
20	150	14	14	A10	40	20.0	0.20
20	150	27	27	A25	29	15.6	0.15

3.2 Ospedale San Luca (LU)

The "San Luca" hospital, Via Guglielmo Lippi Francesconi 556, 55100 Lucca (IT), houses a Synergy 3028 linear accelerator made and distributed by Elekta (Stockholm, Sweden). The machine can operate with electrons of 6, 9 and 12 MeV and photons of 6 and 18 MV. The collimation jaws can size fields from 3x3 cm^2 to 20x20 cm^2.
The pulse frequency, measured by the dedicated diagnosis software, results to be 400 Hz for 6 MV photons and 200 Hz either for 10 and 15 MV photons. Again, a phantom made in polystyrene of 30x30 cm^2 area and 20 cm height was placed on the patient bed at a source to skin distance (SSD) of 100 cm to simulate the human chest.

3.2.1 Measurements with LUPIN Detector

Irradiation with photon beams

Similarly to what was done in Varese, the first part of the work consisted in the measurement of the neutron dose related to photon irradiation. Most measurements were made only with the LUPIN detector, but we were able to make few runs with other detectors that were available at the hospital. Again, the machine was used with the usual configuration:

- Gantry angle: 0°
- SSD: 100 cm
- Irradiation time: 20 s
- Monitor Units: 600 MU per minute (1 MU = 1 cGy in calibration conditions)
- Detector position: on patient bed

The LUPIN detector was placed on the patient bed at 50, 100 and 150 cm from the isocenter. Results are reported in Table 3.7.
However, during a real therapy session, measurements could not be made with the detector placed on the patient bed. For this reason, it was decided to make a second experiment in conditions that were more realistic and in line with what would be a real situation. First of all, the LUPIN detector was placed in a new position, suitable to be reproduced during real therapy sessions. In particular, it was set on a portable ladder next to the patient bed, at the same height of the patient bed but 81 cm from the isocenter and 62,5 cm from the vertical bed axis. The configuration is shown in Figure 3.8. Also, instead of the solid water phantom, a BOttle MAnnikin ABsorber (BOMAB) phantom developed by the University of Pisa was used for simulating the

human chest. This phantom is a polyethilene elliptical cylinder filled with water, specifically designed to simulate the human body (see Figure 3.2). Only five relevant machine configurations were measured, and are reported in Table 3.6.

Table 3.6. Neutron H*(10) from Elekta Synergy 3028 operating with photon beams on the BOMAB phantom, measured by LUPIN in Lucca

Energy (MV)	Detector position	jaw X (cm)	jaw Y (cm)	H*(10) (μSv)
15	Room	20	20	1216
10	Room	20	20	570
6	Room	20	20	87
6	Room	10	10	7
6	Room	3	3	2

Table 3.7. Neutron H*(10) from Elekta Synergy 3028 operating with photon beams, measured by LUPIN and other rem counters (L= LUPIN, A = Berthold, B = NRD, C = Wendy) in Lucca

E (MV)	D (cm)	jaw X (cm)	jaw Y (cm)	L (μSv)	A (μSv)	B (μSv)	C (μSv)
15	50	3	3	1882			
15	50	10	10	1870			
15	50	20	20	1884			
15	100	3	3	1487			
15	100	10	10	1464			
15	100	20	20	1454	169	138	70
15	150	3	3	1166			
15	150	10	10	1143			
15	150	20	20	1122			
10	50	3	3	807			
10	50	10	10	837			
10	50	20	20	906			
10	100	3	3	661			
10	100	10	10	659			
10	100	20	20	679	102.7	93	
10	150	3	3	504			
10	150	10	10	502			
10	150	20	20	513			
6	50	3	3	6			
6	50	10	10	58			
6	50	20	20	251			
6	100	3	3	6	8.6	14.4	
6	100	10	10	16	8.7	14.56	
6	100	20	20	62	8.6	14.7	
6	150	3	3	2			
6	150	10	10	3			
6	150	20	20	20			

Table 3.8. Neutron H*(10), H*(10) per Gy and H*(10) per MU from Elekta Synergy 3028 operating with photon beams, measured by LUPIN in Lucca. The approximation 1 MU = 1 cGy have been used for all field sizes.

E (MV)	D (cm)	jaw X (cm)	jaw Y (cm)	H*(10) (μSv)	μSv/Gy	μSv/MU
15	50	3	3	1882	941	9
15	50	10	10	1870	935	9
15	50	20	20	1884	942	9
15	100	3	3	1487	744	7
15	100	10	10	1464	732	7
15	100	20	20	1454	727	7
15	150	3	3	1166	583	6
15	150	10	10	1143	572	6
15	150	20	20	1122	561	6
10	50	3	3	807	404	4
10	50	10	10	837	419	4
10	50	20	20	906	453	5
10	100	3	3	661	331	3
10	100	10	10	659	330	3
10	100	20	20	679	340	3
10	150	3	3	504	252	3
10	150	10	10	502	251	3
10	150	20	20	513	257	3
6	50	3	3	6	3	0
6	50	10	10	58	29	0
6	50	20	20	251	125	1
6	100	3	3	6	3	0
6	100	10	10	16	8	0
6	100	20	20	62	31	0
6	150	3	3	2	1	0
6	150	10	10	3	1	0
6	150	20	20	20	10	0

XRT Simulations

For the simulation of real treatment plans, two different tumor sites have been simulated, lungs and breast. For both cases, the detector was placed at the same position at 81 cm from the isocenter and 62,5 cm from the vertical bed axis, and the BOMAB phantom was used for simulating the human chest. The SSD was again set to 100 cm.

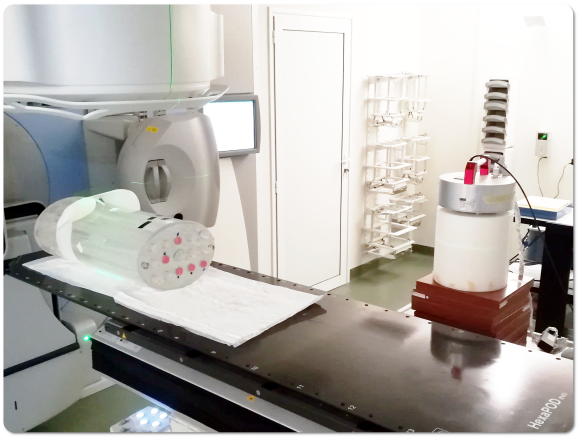

Figure 3.2. BOMAB phantom with silicon breast. At the right, the LUPIN detector

Breast Cancer

To simulate a woman breast, two silicon mammaries were placed on top of the phantom. The right was 300 cm^3 in volume to simulate a small breast, while the left was 500 cm^3 to simulate a large breast. Several XRT plans were delivered to both mammaries with 10 and 15 MV beam energy. To keep the experiment in line to what would be a real therapy session with the LUPIN detector used by medical operators for real time neutron monitoring, all values in this section are given strictly as reported by the LUPIN software, without any post-hoc photon rejection correction.
The first simulation was a 10 MV 10 Gy therapy divided in 5 fractions of 2 Gy to the tumor site (small breast). Each fraction can be further divided in 2 steps, each one with the machine gantry set at a different angle. The overall therapy started from position 1 (closer to the detector) for the first burst, then moved in position 2 (vertically symmetrical) for 5 burst and returned to position 1 for the last 4 bursts. Results are given in Table 3.9. In addition, the dose rate profile acquired by the lupin detector is showed in Figure 3.3.
The second simulation was a 4 Gy therapy divided in 2 fractions of 2 Gy to the tumor site (small breast). Again, each fraction can be divided in 2 steps of different gantry position. The beam energy was 15 MV. Results and dose rate profile are given in

Table 3.10 and Figure 3.4.

Table 3.9. Neutron H*(10) from breast cancer XRT - 10 MV, 10 Gy (small breast)

Dose (MU)	160	166	166	166	166	166	160	160	160	160
H*(10) (μSv)	768	86	89	90	90	90	795	775	771	783

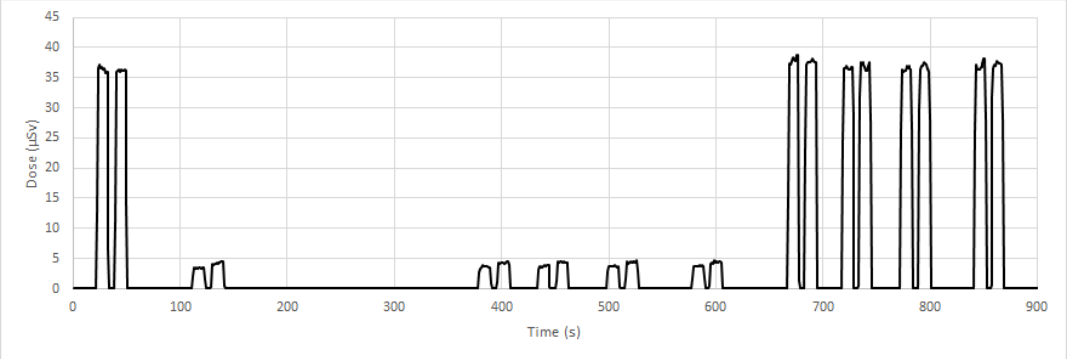

Figure 3.3. Dose profile for breast cancer XRT - 10 MV, 10 Gy (small breast)

Table 3.10. Neutron H*(10) from breast cancer XRT - 15 MV, 4 Gy (small breast)

Dose (MU)	156	161	161	156
H*(10) (μSv)	1728	393	397	1747

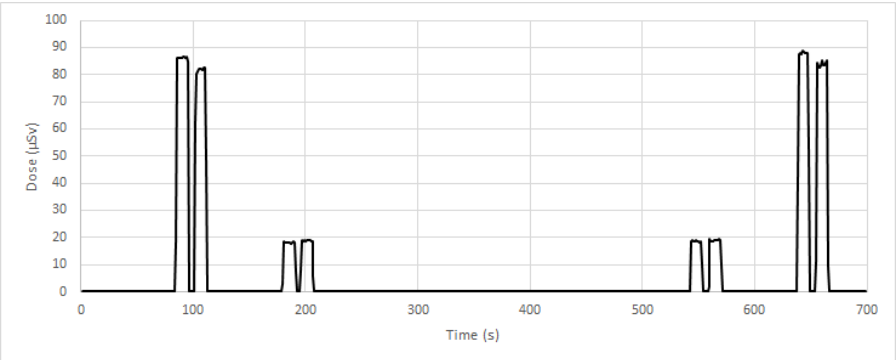

Figure 3.4. Dose profile for breast cancer XRT - 15 MV, 4 Gy (small breast)

The third simulation was a 10 Gy therapy divided in 5 fractions of 2 Gy to the tumor site (large breast). Again, each fraction can be divided in 2 steps of different gantry position. The beam energy was 10 MV. Results and dose rate profile are given in Table 3.11 and Figure 3.5.

The fourth simulation was a 6 Gy therapy divided in 3 fractions of 2 Gy to the tumor

site (large breast). Again, each fraction can be divided in 2 steps of different gantry position. The beam energy was 15 MV. Results and dose rate profile are given in Table 3.12 and Figure 3.6.

Table 3.11. Neutron H*(10) from breast cancer XRT - 10 MV, 10 Gy (large breast)

Dose (MU)	119	119	119	119	119	119	119	119	119	119
H*(10) (μSv)	204	411	415	417	416	412	207	204	206	202

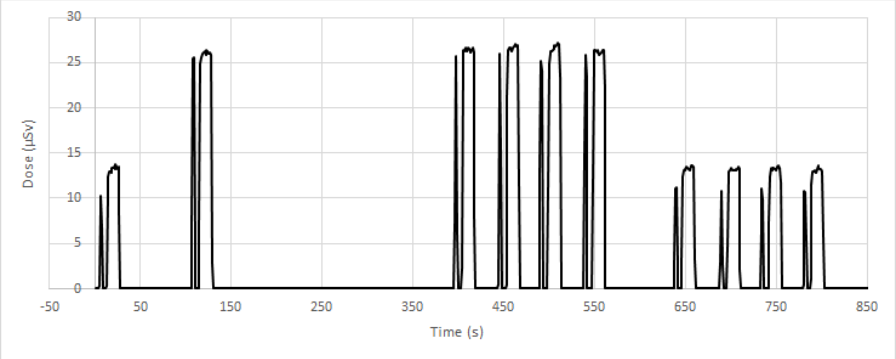

Figure 3.5. Dose profile for breast cancer XRT - 10 MV, 10 Gy (large breast)

Table 3.12. Neutron H*(10) from breast cancer XRT - 15 MV, 6 Gy (large breast)

Dose (MU)	114	114	114	115	115	115
H*(10) (μSv)	931	929	926	502	513	513

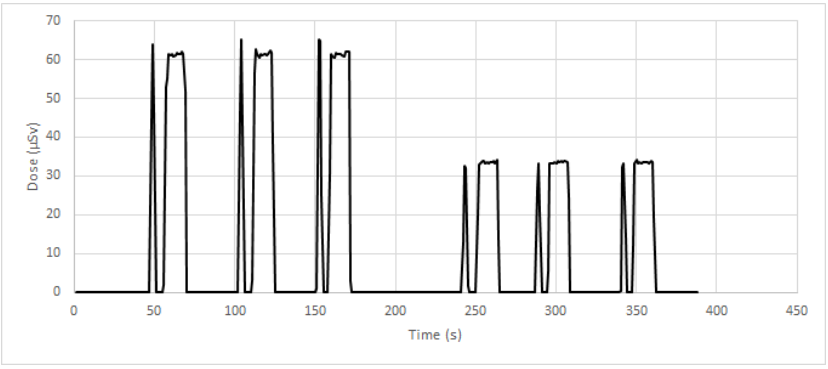

Figure 3.6. Dose profile for breast cancer XRT - 15 MV, 6 Gy (large breast)

Lung Cancer

To simulate lung cancer treatment plans, the silicon mammaries were removed and the phantom was placed on the patient bed with a SSD of 83.1 cm. The repetition rate was set to 200 MU/min. For each fraction of all plans, the gantry made a full rotation clockwise around the patient body. Four different plans were simulated and a summary is reported in Table 3.13. Also, the dose rate profile of plan 1 is reported in Figure 3.7 for example.

Table 3.13. Neutron H*(10) from lung cancer XRT - Summary

Plan	Tumor (cm)	E (MV)	Fractions	Gy/Fraction	T (min)	H*(10) (μSv)
1	3	10	10	2	12	6097
2	3	15	5	2	6	6890
3	6	10	2	2	2.4	1106
4	6	15	1	1	1.2	648

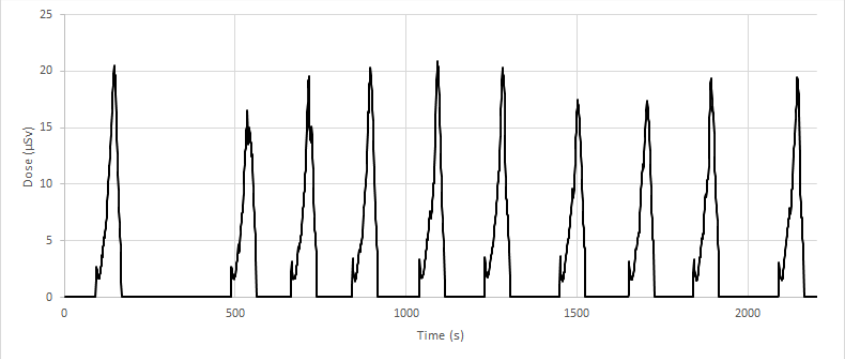

Figure 3.7. Dose profile (Lung cancer XRT - 10 MeV 20 Gy, tumor of 3 cm diameter)

3.3 Ospedale Maggiore (TS)

The "Ospedale Maggiore - Azienda Sanitaria Universitaria Integrata (ASUI)" hospital, Via Giovanni Sai 7, 34128 Trieste (IT), houses an Elekta Synergy 3028 linear accelerator identical to the model available in Lucca, which technical specification are reported in Chapter 3.2

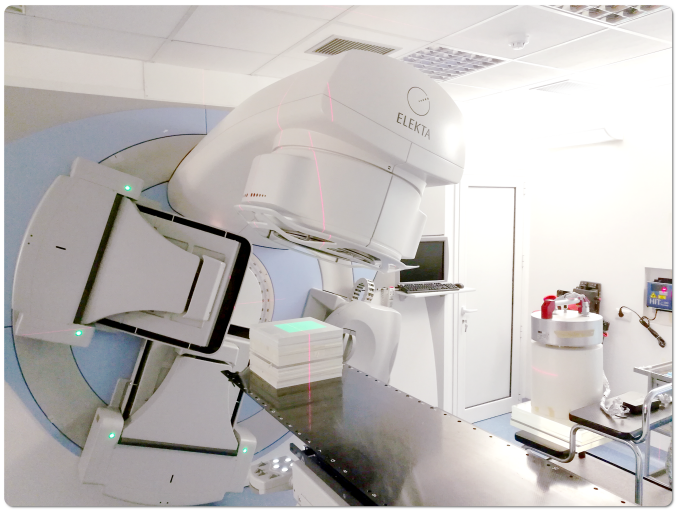

Figure 3.8. Elekta Synergy 3028, ASUI Hospital, Trieste

Likewise the previous experiments, a phantom made in polystyrene with 2% TiO2 in mass of 30x30 cm2 area and 20 cm height was placed on the patient bed at a source to skin distance (SSD) of 100 cm to simulate the human chest.

3.3.1 Measurements with LUPIN Detector

Irradiation with photon beams

Similarly to what was done in Varese and Lucca, the first part of the work consisted in the measurement of the neutron dose with the LUPIN detector. Again, the experiment was made to assess the neutron ambient dose equivalent related to the linear accelerator operating with photon beams in different conditions. The measurements, in this case, were made only with the LUPIN detector, since no other rem counter was available on site. The machine was used with the usual configuration in order to get comparable values to previous experiments.

- Gantry angle: 0°
- SSD: 100 cm
- Irradiation time: 20 s

- Monitor Units: 600 MU per minute (1 MU = 1 cGy in calibration conditions)
- Detector position: on patient bed

The LUPIN detector was placed for the first experiment on the patient bed at 50, 100 and 150 cm from the isocenter, since it was not possible to extend the bed length to 200 cm, and for the second experiment next to the patient bed, as it was done in Lucca. Results of these experiments, as usual expressed in terms of H*(10), are reported in Table 3.16 and Table 3.14.

Table 3.14. Neutron H*(10) from Elekta Synergy 3028 operating with photon beams (2^{nd} experiment), measured by LUPIN in Trieste

Energy (MV)	Detector position	jaw X (cm)	jaw Y (cm)	H*(10) (μSv)
15	Room	20	20	1324
10	Room	20	20	539
6	Room	20	20	50
6	Room	10	10	10
6	Room	3	3	4

Irradiation with electron beams

The second experiment was made with electron beams. Since the experiment in Varese showed that the dose was basically negligible over a distance of 100 cm except for high energy electrons, the detector was placed only at 50 cm from the isocenter. The electron energy was set to 6, 9 and 12 MV.
The working parameters of the machine were the same as in Varese:

- Gantry angle: 0°
- SSD: 100 cm
- Irradiation time: 20 s
- Monitor Units: 600 MU per minute (1 MU = 1 cGy in calibration conditions)
- Detector position: on patient bed

Results are reported in Table 3.15.

Table 3.15. Neutron H*(10) from Elekta Synergy 3028 operating with electron beams, measured by LUPIN in Trieste

Energy (MeV)	D (cm)	jaw X (cm)	jaw Y (cm)	Applicator	H*(10) (μSv)	μSv/MU
6	50	20.4	21.8	A10	3	0.015
9	50	20	22	A10	15	0.075
12	50	17.8	19.2	A10	30	0.150

Table 3.16. Neutron H*(10), H*(10) per Gy and H*(10) per MU from Elekta Synergy 3028 operating with photon beams (1^{st} experiment), measured by LUPIN in Trieste. The approximation 1 MU = 1 cGy was used for all field sizes.

Energy (MV)	Distance (cm)	jaw X	jaw Y	wedge (deg)	H*(10) (μSv)	μSv/Gy	μSv/MU
15	50	3	3		1760	880	8.80
15	50	10	10		1767	884	8.84
15	50	20	20		1791	896	8.96
15	50	20	20	60	1673	837	8.37
15	100	3	3		1425	713	7.13
15	100	10	10		1411	706	7.06
15	100	20	20		1379	690	6.90
15	150	3	3		1103	552	5.52
15	150	10	10		1081	541	5.41
15	150	20	20		1075	538	5.38
10	50	3	3		659	330	3.30
10	50	10	10		700	350	3.50
10	50	20	20		816	408	4.08
10	100	3	3		534	267	2.67
10	100	10	10		539	270	2.70
10	100	20	20		566	283	2.83
10	150	3	3		405	203	2.03
10	150	10	10		406	203	2.03
10	150	20	20		425	213	2.13
6	50	3	3		11	5	0.05
6	50	10	10		52	26	0.26
6	50	20	20		242	121	1.21
6	100	3	3		2	1	0.01
6	100	10	10		7	3	0.03
6	100	20	20		47	23	0.23
6	150	3	3		1	0	0.00
6	150	10	10		5	2	0.02
6	150	20	20		11	5	0.05

3.3.2 Measurements with Bubble Detectors

The second part of the work in Trieste consisted in the acquisition of the neutron dose by using BDT and BD-PND bubble dosimeters, either with and without the above mentioned dosimetric phantom. The setup parameters were the same that were used for the results acquired in Table 3.14 and are summarized below:

- LINAC configuration: Gantry at 0°
- Solid water phantom: positioned on the patient bed with its surface at a distance of 90 cm from the isocenter (SSD).
- Bubble dosimeters: placed in the same position of the LUPIN detector (81 + 12.5 cm from isocenter[2], 62.5 + 12.5 cm from the bed vertical axis)
- Photon beam energy: 6, 10, 15 MV
- Field dimension: 20x20, 10x10 and 3x3 cm^2

Figure 3.9. Experimental setup with bubble dosimeters in field and out of field

The readout of bubble detectors was made by eye by two different observators and one more time on a digital photography with enhanced contrast. The proposed result is the average of the three counts.
Before heading to the results, it is important to make some considerations. From the number of bubbles, the dose was calculated by the relationship

$$Dose(\mu Sv) = \frac{number\ of\ bubbles}{S} \tag{3.1}$$

[2]12.5 cm is the radius of the LUPIN detector

where S (μSv^{-1}) is the sensibility given by the manufacturer, which is different for each dosimeter.
The dose d_I (%) represents the fraction of the impinging dose without the polyethylene layer, while the value T/F (%) is the percentile ratio between the dose due to thermal neutrons and the dose due to fast neutrons.
The neutron flux, in terms of n/cm^2/UM, was calculated from the ambient equivalent dose through conversion coefficients [9]

- k_f = 1x10^{-5} μSv·cm^2 for fast neutrons;
- k_{th} = 4x10^{-4} μSv·cm^2 for thermal neutrons.

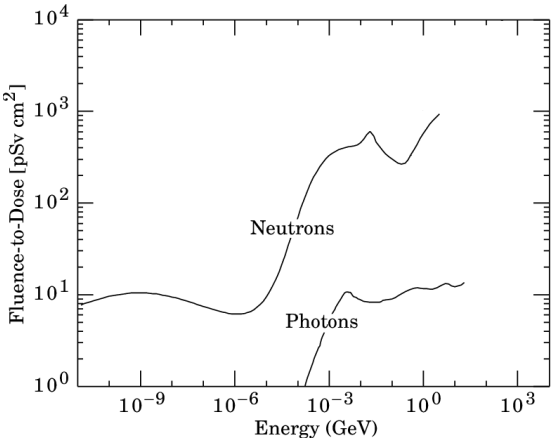

Figure 3.10. Fluence to dose equivalent conversion factors for neutrons and photons

Since BDT dosimeters are mainly sensible to thermal neutrons, but they still show a small sensibility to fast neutrons, an uncertainty of about 10% in the dose measurement should be considered, meaning that a tenth of the detected neutrons could be fast instead of thermal. However, results are reported here without the subtraction of the uncertainty.
Also, BDT dosimeters inside the dosimetric phantom do not interact with thermal neutrons from the source. In fact, such neutrons are absorbed by the phantom. The dose reported by BDT dosimeters inside the dosimetric phantom is, actually, the dose related to fast and epithermal neutrons that have been slowed down to thermal energy by the dosimetric phantom.
Finally, it is important to note that each dosimeter was irradiated with a different amount of monitor units, in order to get a sufficient number of bubbles. For this reason, the relevant results are collected as dose per MU. Results are reported in Table 3.17 and will be commented below.

Table 3.17. Neutron H*(10) measured by bubble dosimiters. A = in field, B = out of field, C = in field inside the phantom D = out of field inside the phantom

Pos.	Type	S (1/μSv)	Dose/UM	d1	T/F	Fluence (n/cm2/UM)
A	BDT	2.2	1.693	100	12.87	4.23E+02
	BD-PND	2.3	13.154	100		1.32E+05
B	BDT	2.8	0.161	100	9.78	4.02E+01
	BD-PND	2.8	1.643	100		1.64E+04
C	BDT	2.2	1.125	66.5	11.79	2.81E+02
	BD-PND	2.6	9.538	72.51		9.54E+04
D	BDT	2.3	0.058	36.19	19.66	1.46E+01
	BD-PND	2.7	0.296	18.03		2.96E+03

3.3.3 Montecarlo Simulation

The final part of the work was to compare the LUPIN results with a montecarlo simulation. The code was developed by the University of Trieste using the transport code MCNPX by Los Alamos National Laboratory (New Mexico, U.S.).

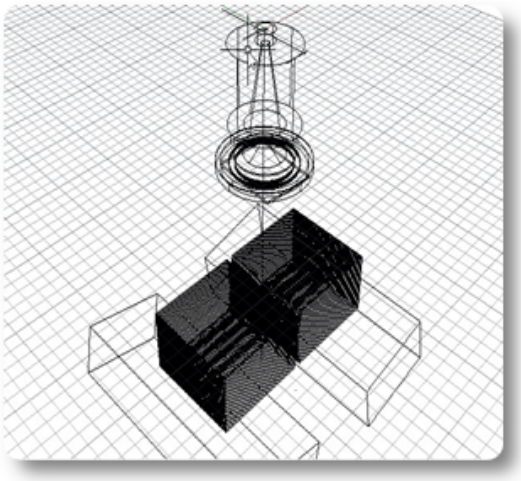

Figure 3.11. LINAC head modeling for montecarlo simulation. You can easily recognize the target, the flattening filter and the collimator jaws

First, all the components of the Elekta Synergy linac head and the room plant were modeled with Autocad with data provided by Elekta. Then, "VISED" visual editor was used to convert the complex geometry to the geometry CARD of MCNPX. Finally, data were coded and the code was evaluated in terms of measured percentile-depth-dose (PDD) and dose profile for 15 MV photon beam energy. The results showed a good agreement either with experimental data acquired with bubble dosimeters (see Figure 3.12) and literature data [26].
The point ambient dose equivalent was calculated using the F5 tally which scores the

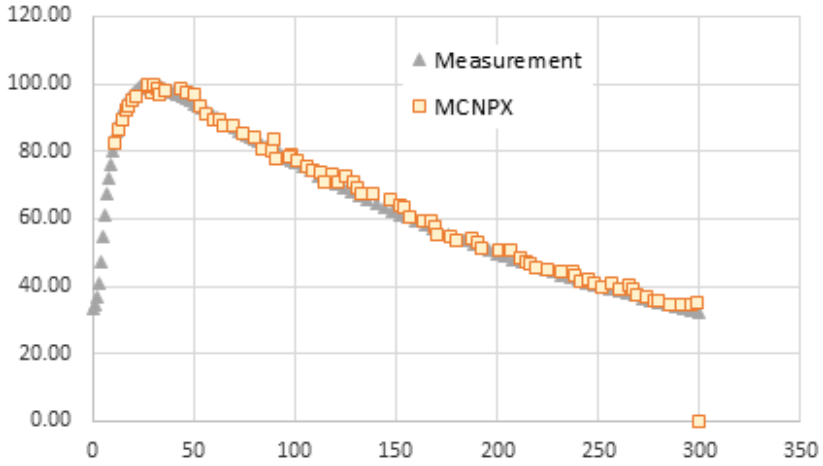

Figure 3.12. Validation of the simulation of linac for 15MV and 10X10 field size (PDD)

neutron fluence at a certain point and can be converted to ambient dose equivalent by conversion function features of MCNPX.

Table 3.18. Neutron H*(10) calculated by montecarlo code (MCNPX) for Elekta Synergy 3028, Trieste. The results from the LUPIN detector are reported for comparison, based on the approximation 1 MU = 1 cGy

Energy (MV)	D (cm)	jaw X	jaw Y	MC (mSv/Gy)	LUPIN (mSv/Gy)
15	50	3	3	0.92	0.88
15	100	3	3	0.81	0.8835
15	150	3	3	0.63	0.8955
15	50	10	10	0.95	0.7125
15	100	10	10	0.83	0.7055
15	150	10	10	0.65	0.6895
15	50	20	20	0.99	0.5515
15	100	20	20	0.85	0.5405
15	150	20	20	0.68	0.5375
6	50	3	3	0.0057	0.0055
6	100	3	3	0.0044	0.026
6	150	3	3	0.0021	0.121
6	50	10	10	0.0091	0.001
6	100	10	10	0.0085	0.0035
6	150	10	10	0.0058	0.0235
6	50	20	20	0.164	0.0005
6	100	20	20	0.055	0.0025
6	150	20	20	0.0081	0.0055

The simulation was performed at three different positions along the patient bed (50, 100 and 150 cm from the isocenter) for three different field sizes (3x3, 10x10 and 20x20 cm^2) and a SSD of 100 cm. Also, a preliminary neutron spectrum was simu-

lated, and it is reported in Figure 3.13.

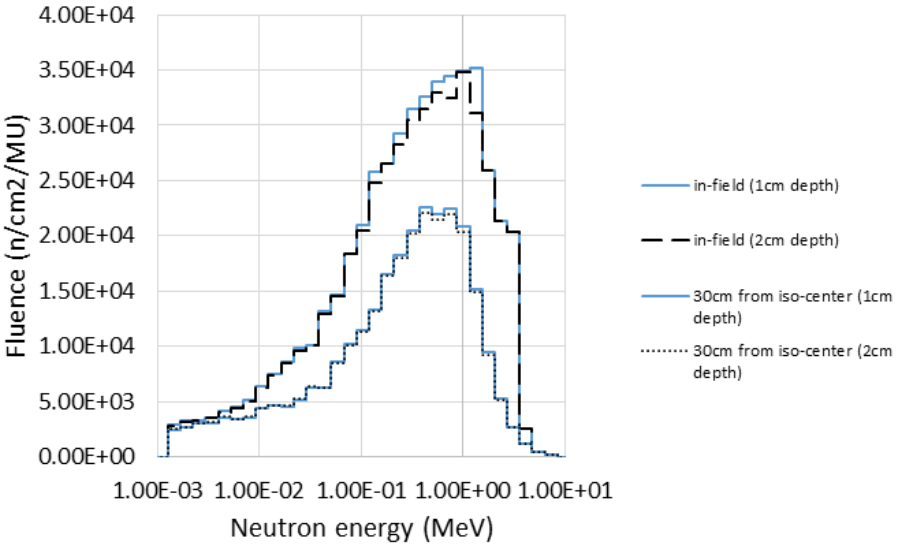

Figure 3.13. Neutron energy spectrum (preliminary) simulated by MCNPX

It should be noted that MCNPX results are estimated per source particle (i.e. electron), therefore the final results were normalized to the scored dose at the maximum depth in a water phantom. For the Elekta Synergy 3028, the machine is calibrated to give 1 cGy per MU at maximum depth for reference conditions of 100 cm SSD and 10x10 cm^2 field size. Maximum depth is D_{max} = 2.9 cm for 15 MV and and D_{max} = 1.7 cm for 6 MV photons. Though an in-depth evaluation is still to be done, preliminary results of the montecarlo simulation are reported in Table 3.18.

3.4 Results

Neutron Production

The measurements gathered in this work open up to various considerations. About neutron production, it is easily confirmed that the photoneutron production is far higher for photon beam energy above 6 MV, and increases for higher energy. This behaviour strongly agrees with the hypothesis that the main neutron production takes place in tungsten, that is the main component of the bremsstrahlung target and the collimation stages for most linear accelerators [8]. This behaviour is also confirmed by the montecarlo simulation of the Varian 2100C/2300C presented by A. Naseri et Al. [7] and M. Kralik et Al. [27], showing that the greatest neutron production takes place in such components, in particular the primary collimator ($\sim$ 40%) and the jaws ($\sim$ 30%). Also, we can notice in Figure 3.14 that neutron production per monitor

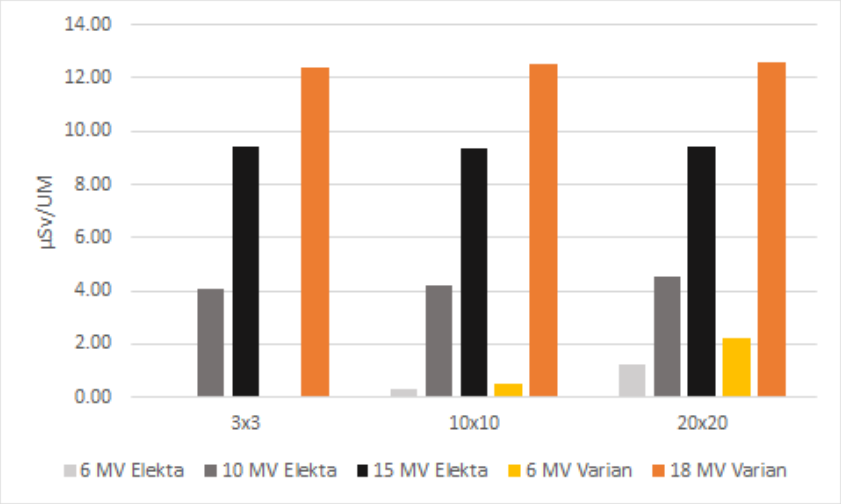

Figure 3.14. Dose expressed as H*(10) per Monitor Unit (μSv/MU) for different energy (MV) and field size (cm^2) at 50 cm from the isocenter, Elekta Synergy (Lucca) and Varian Clinac (Varese)

unit for either the Varian and the Elekta linacs is almost constant at high energy (15 and 18 MV) while increasing a lot with the irradiation field size for 6 MV energy and by a small amount at 10 MV. Though it is reported in literature that the neutron yield increases linearly as the field size decreases [28], in fact, it must be considered that also the attenuation of neutrons increases with the closing of the jaws. For example, by taking into account this double behavior, H. Kim et Al. calculated that 20x20 cm^2 is the field dimension related to the maximum photoneutron dose around the Varian Clinac 2100C/2300C either at 10 and 15 MV [29], and such conclusion can be considered well in agreement with our results.

This behaviour is also in agreement with the calculations made by Naseri et Al. [7],

showing a different overall contribution of the machine head components at different energy. In fact, the contribution of the jaws increases of about ∼20% when dealing with 10 MV photons with respect to 20 MV photons. This is be possible because neutrons produced at lower energy in previous stages of the machine head are also more likely to be absorbed, lowering their overall contribution. Then, we can easily justify a higher contribution of the jaws to the neutron production at 6 MV.
In general, the ambient dose data acquired by the LUPIN detector and normalized by delivered Gy (or UM) are in good agreement with data available in literature and measured by passive detectors around different linear accelerators (a full list of data is available in Reference [7], [8], [10], [11], [30], [27] and [31]). For example, the results presented by Cardenas et Al., by operating a Varian 2liX with a 4x4 cm^2 18 MV photon beam, measured an ambient dose of around 1500 μSv/Gy at 30 cm from the isocenter using gold foils in moderator buckets [10], and such result well agrees with the dose measured in similar conditions by the lupin detector, that was 1527 μSv/Gy (Varian Clinac DHX, 18 MV beam energy, 3x3 cm^2 field size, 50 centimeters from the isocenter, see Table 3.2). From the simulation of therapy plans, most of which are summmarized in Figure 3.15, we can see that the neutron ambient dose equivalent related to a complete therapy is typically around few millisieverts. However, therapies

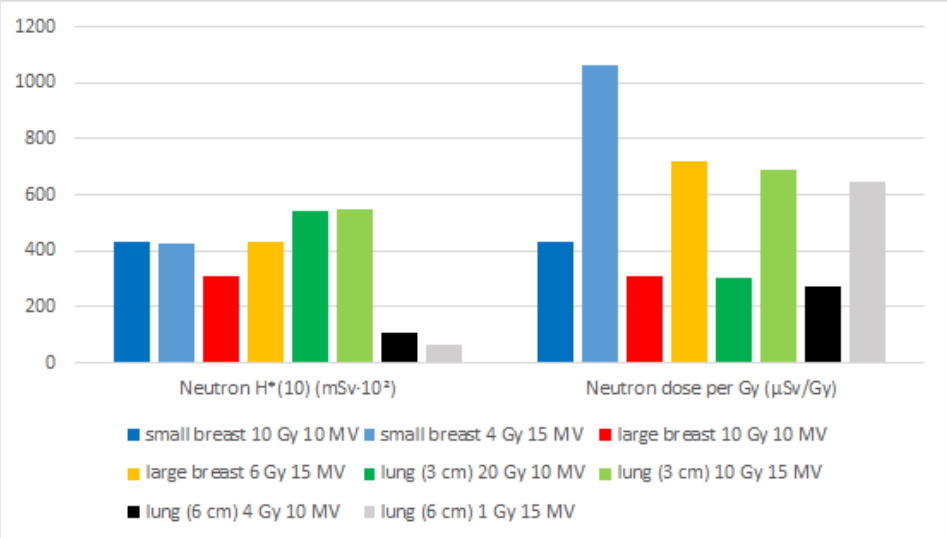

Figure 3.15. Dose expressed as H*(10) (mSv·10^2) and μSv per Gy for different therapy plans simulated on the BOMAB phantom - Elekta Synergy 3028, Lucca

are never conducted in a single session, and most times are divided in fractions of about 2 Gy each. If we consider the neutron dose as dose per delivered Gy, which is a more valuable physical dimension for comparison purposes, we can conclude that the overall neutron dose is again dependent from the beam energy, with 15 MV therapy being responsible for a dose per Gy that results to be almost double with respect

to 10 MV therapy, but all values settle in the hundreds of μSv per Gy up to 1 mSv per Gy, values that are in the same order of magnitude of the montecarlo simulation results.
Moving from photon to electron therapy, it is important to note that the same considerations about neutron production are still valid for electron primary beams. However, the neutron production is very little compared to the one due to photon beams. This is mainly justified by the fact that, in case of electron therapy, photons reacting with components materials are only the unwanted photons produced by the collision of electrons against walls or other components, but, in principle, all electrons should be focused and delivered to the patient without the production of photons, so without photoneutron production. In fact, the maximum ambient dose equivalent related to electron beams in this work results to be about 150 μSv/200 MU, and it was acquired at 50 cm from the isocenter by operating the Varian linac at 20 MeV energy (see Table 3.5), but, in general, values are an order of magnitude lower than those acquired for photon beams of similar energy. Also, it is sufficient to decrease the beam energy from 20 to 16 MV to get a dose that results almost halved (77 μSv per 200 MU). To conclude, such value is also well in agreement with data from Biltekin et Al., which in similar conditions (15 MeV, 10 cm distance, Varian Clinac DHX) measured a value of 0.44 μSv/MU. [32].

LUPIN vs Traditional REM Counters

The LUPIN performance can be easily compared to that of other active instruments that are already available in hospitals. In particular, the NRD neutron rem counter was available in Varese, while three different detectors were available in Lucca (NRD, Berthold, Wendy).
As it was expected from literature, all these detectors fail to measure the correct dose in the pulsed mixed field environment produced by linear accelerators, and such behavior is clearly due to the pulse pile up that affects standard active detectors [12]. By making, for example, a comparison between LUPIN and NRD, we can notice that the LUPIN detector can reveal a neutron dose up to ten times higher than the NRD when operating the Varian Clinac at 18 MV energy (see Figure 3.16). Also, while the LUPIN detector shows a decreasing linear trend with distance, the NRD shows the highest dose at the highest distance, that in principle should not be reasonable. However, this is again justified by the pile-up problem since far from the isocenter, where the dose rate is lower, the detector suffers less from pile up and the overall count can get higher. When dealing with 6 MV photons, the situation is quite different. The LUPIN detector still records an ambient dose equivalent over 15 times higher

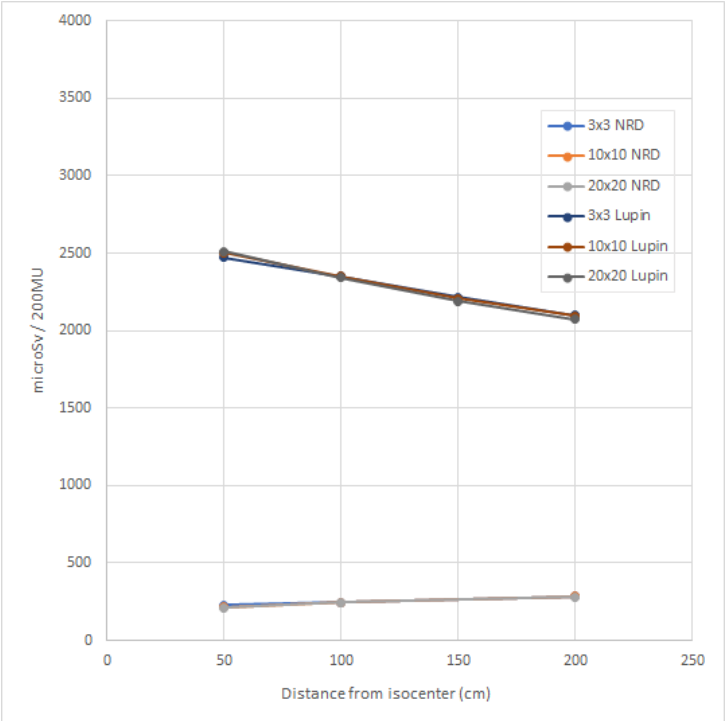

Figure 3.16. Lupin vs NRD ambiental dose (μSv), 18 MV

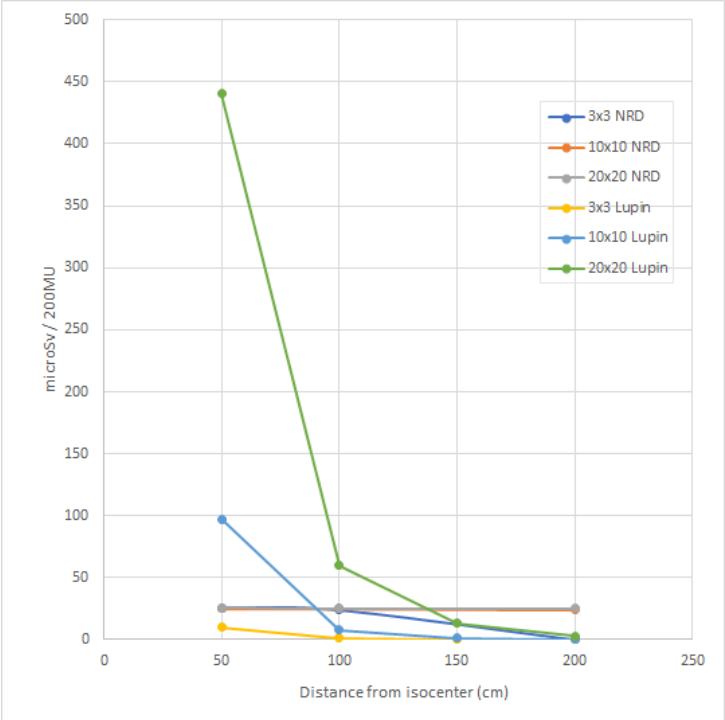

Figure 3.17. Lupin vs NRD ambiental dose (μSv), 6 MV

than the NRD in the worst case scenario (20x20 cm^2 field size, 50 cm distance), but the difference gets smaller and vanishes at increasing distance (and decreasing field size), to the point that the NRD dose results even higher. However, the NRD rem counter still struggles with saturation, in fact, the measured dose do not increase at decreasing distance (except for the 3x3 cm^2 field size), as instead we would reasonably expect.

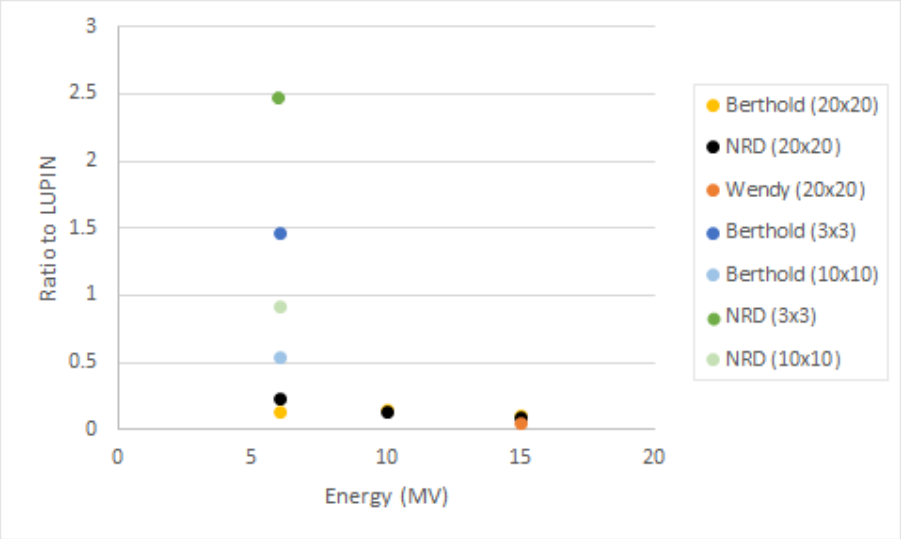

Figure 3.18. Dose Ratio of various detectors to LUPIN, both expressed as μSv per 200 MU in various machine configurations, data acquired at 100 cm from the isocenter, Elekta Synergy (Lucca)

Switching from the Varian Clinac to the Elekta Synergy the result is basically the same, concluding that no detector was able to stand up to the lupin performance (see Figure 3.18) in any condition except when doses are particularly low (6 MV, 3x3 and 10x10 cm^2 field size). This conclusion also confirms the result of a previous study on the Elekta Synergy 3028 made by S. Savatović, Università degli Studi di Trieste, which compared the performance of a Berthold LB 6411 to bubble dosimeters, concluding that such rem counter was not suitable for neutron counting inside a RT treatment room [33].

Instrument Comparison

In this section we will compare results acquired by different detectors and MC simulation, integrated also with previous data collected for the same linear accelerator in 2018 using bubble detectors and a Berthold LB 6411 rem counter [33]. Also, for completeness, a theoretical calculation of the ambient dose equivalent based on the neutron spectrum, calculated by L. Alticozzi et Al. [34], will be included in the comparison.

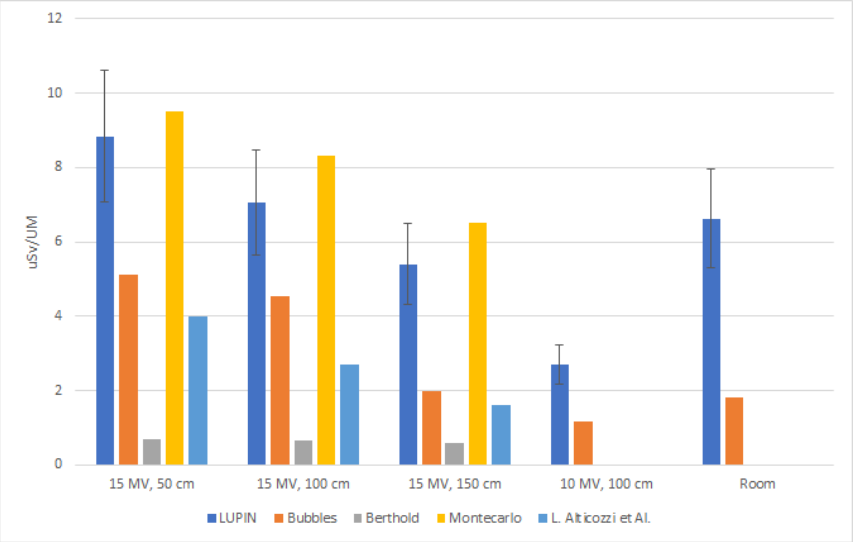

Figure 3.19. Ambient dose per MU compared between LUPIN, bubble detectors, MC simulation and literature data. The label "Room" indicates the measurements acquired on the stand next to the patient bed

As we can see from Figure 3.19, that shows the dose responce in terms of μSv/MU for different instruments, the LUPIN detector and the MC simulation are in good agreement, especially if we consider the uncertainty. In fact, not only the dose per MU is comparable, though slightly higher for the simulation, but also the trend with distance is quite coherent. As we could expect, however, this is not true for the Berthold rem counter, which provides a flat response over distance that is, instead, coherent with the responce of the NRD counter mentioned above. Moving to the bubble detectors, we must notice that, in general, we get a responce that is much lower than the one acquired by the LUPIN detector and calculated by MC simulation, either for our measurements and literature data by Savatovic S. [33]. Also, our measurements are not in agreement with literature data expecially regarding the thermal neutron flux. Though these anomalies are expected to be related to a bad conservation of bubble dosimeters and it is going to be further investigated, results are still worth to be commented and discussed. By using bubble detectors, in principle, it was possible to investigate either the thermal and the epithermal-fast neutron component separately. In particular, we can see that the main contribution to the total dose next to the patient bed, at a distance of about 110 cm, is due to fast neutrons, with a thermal-to-fast ratio of about 10% [25]. However, since the dose related to thermal neutrons is lower than 10% of the maximum dose due to fast neutrons, it stands in the relative error given by the producer, B. T. Industries [35].

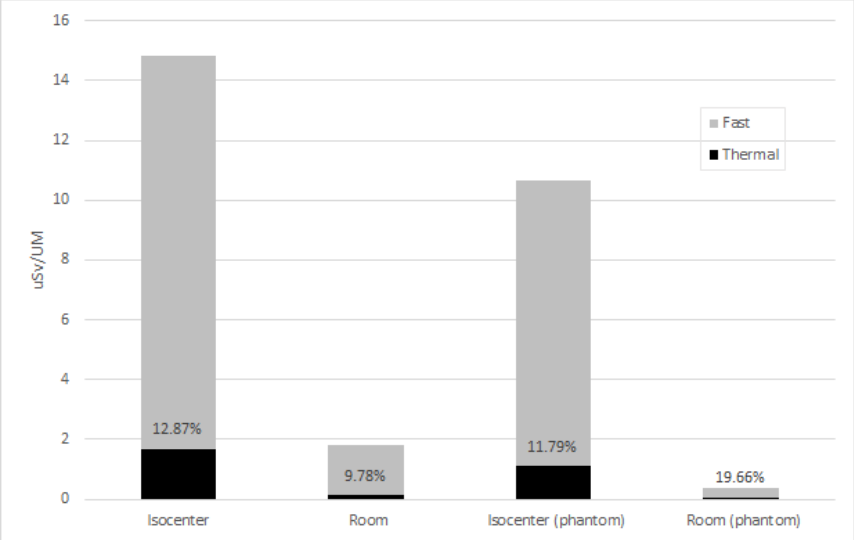

Figure 3.20. Dose per MU measured by bubble detectors, due to thermal and fast component. Also, it is reported the thermal-to-fast ratio.

Chapter 4

Neutron Radiography of Cardiovascular Devices

To investigate the CIEDs internals, and to find a possible relation between malfunctions and boron presence in the devices, which is reported as a possible cause of damage by Zecchin et Al. [5], a neutron radiography analysis was made on a sample of 99 cardiac devices, including pacemakers and defibrillators by different producers and models. Neutron radiography is a non-destructive imaging technique. The resulting image is based on the neutron attenuation properties of the sample. Differently from X-rays, neutrons can only interact with atomic nuclei, so the attenuation pattern is different. Neutrons transmit easily in metals, while they are stopped in light hydrogenous materials and neutron-absorbing materials like Boron and Lithium. For this reason, neutron radiography can be considered sort of complementary to traditional radiography and it is a valid imaging technique to investigate on neutron absorption.

In the production of electronic devices, integrated circuits or other components are sometimes made with a borophosphosilicate glass (BPSG) protective layer [38] that is mainly used for its durability and high resistance to chemicals and thermal shocks, and it is used as an equivalent alternative to the more common phosphosilicate glass (PSG). Since these two materials have identical physical and chemical properties in electronics, they are often used upon availability and no distinction is made in the production process. Nevertheless, BPSG contains boron which has a 20% isotopic abundance in ^{10}B, so it can interact with thermal neutrons and produce heavy ions, which experimental evidence confirms to be a possible cause of damage or symptoms to integrated circuits (ICs) and electronics in general [39] [40]. To investigate on soft errors and malfuctions following the neutron radiography, each device was tested either before and after the irradiation for proper operation.

4.1 The NEUTRA Irradiation Facility

The devices were irradiated at the NEUTRA thermal neutron radiography station at the Paul Scherrer Institut, Forschungsstrasse 111, 5232 Villigen PSI (CH). Measuring position 2 (see Figure 4.1) along the beamline is dedicated to the investigation of samples smaller than 15 cm in diameter.

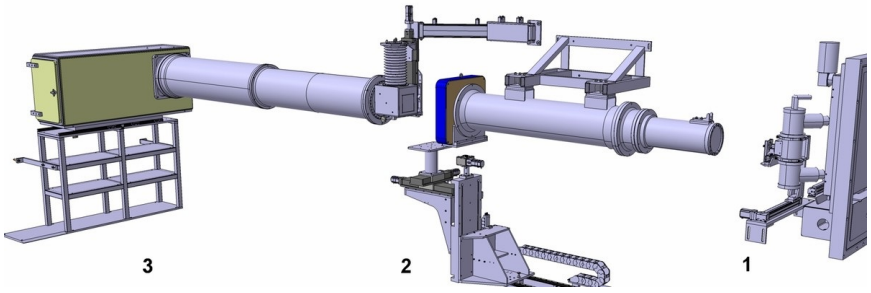

Figure 4.1. Neutra Beam Line

NEUTRA is applied to one of the four twinbeam lines for thermal neutrons at the spallation neutron source SINQ. The neutron spectrum is mainly determined by the moderator, which is heavy water. The beam has a quadratic shape in its centre and the profile is flat over a diameter of about 25 cm [42]. The station can operate with thermal neutrons (0.025 eV) at a flux higher than 5x10^6 neutrons/cm^2/s/mA. The real neutron spectrum is reported in Figure 4.2.

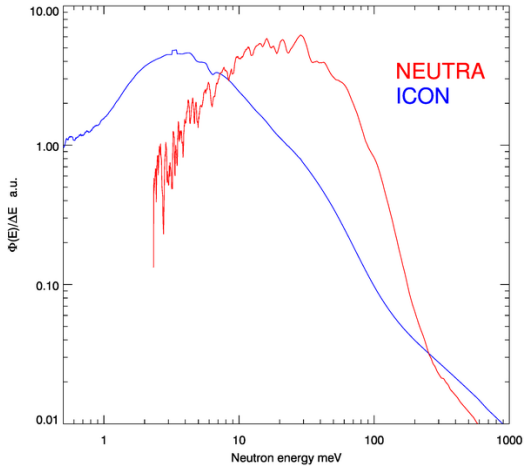

Figure 4.2. Neutra Readout System

The images are acquired by a Ikon-L CCD camera with 50 mm Nikkor lens, connected to a Gadox (Gd_2O_2S) scintillator (see Figure 4.3). The pixel size is 38um and the real resolution using the Siemens star results to be 45 um.
At the NEUTRA station, devices were irradiated by a flux of about 10^7 n/cm^2/s for about 2 minutes each, with some device being irradiated for up to 10 minutes. This

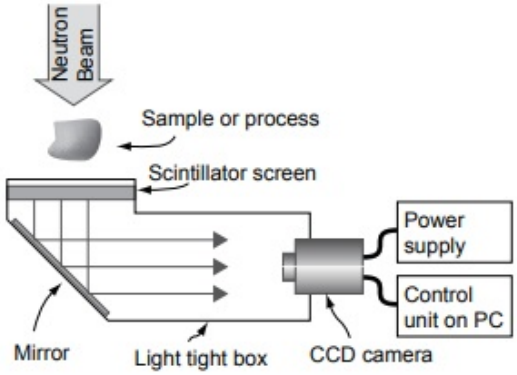

Figure 4.3. Neutra Readout System

is the time that passes between the start and stop of the neutron beam. Nevertheless, a set of 6 images (stacks) were acquired for each device, with an exposure time of 10 seconds for each image, resulting in a total acquisition time of 60 seconds per device. In addition, dark current and open beam image sets were acquired at different time during the day. Dark current images are images acquired with no neutron source, while the open beam images are acquired with no samples. Such image sets are necessary for the image processing of the actual devices. Finally, a reference image set was acquired for samples of regular Luxel and Luxel-n OSL dosimeters, which contains ^{10}B.

4.2 Image Processing

All images were processed using the open source image processing program “ImageJ”. First of all, dark current images were processed by a “Z Project” (projection along the Z axis perpendicular to the image plane) of all stacks into a single image that was then saved as “.tif” file. In this process, each pixel is set to store the average intensity of all stacks at the corresponding pixel location. Then, the dark current (DC) file was used to process the open beam (OB) image closest in time. First, each stack of the OB image was subtracted by the DC file.

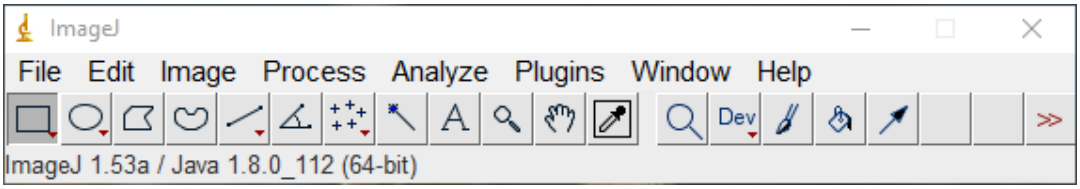

Figure 4.4. Screenshot of the ImageJ software

This is done by the ”image calculator” option. Then, noise was removed by removing

bright outliers. This function replaces a pixel by the median of the pixels in the surrounding area if it deviates from the median by more than a certain threshold (in raw units). The area used for calculating the median was set to a 3 pixel radius area. After noise reduction, a Z project was made on all stacks and the resulting image was saved as ".tif" file.
For processing the images of the cardiac devices, the following procedure was followed. First of all, each stack of the image sequence was checked to make sure that it was correctly acquired. In fact, it is possible that a beam failure results in a bad

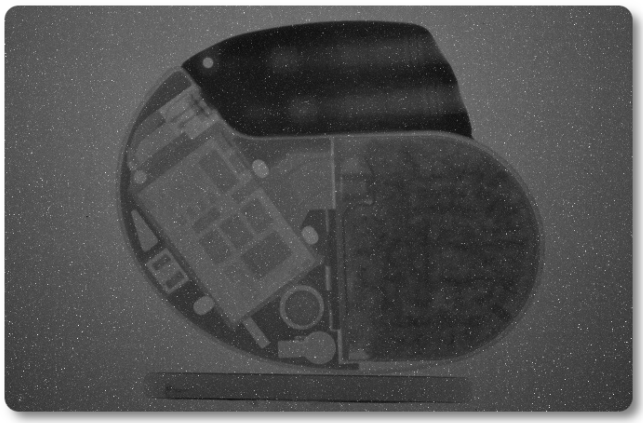

Figure 4.5. St. Jude Verity Adx XL VDR 5456, neutron radiography (raw image)

acquisition that must be excluded. Also, all stacks were flipped vertically to match the open beam and dark current image orientation, which were flipped. Again, all stacks were subtracted by the DC file, noise outliers were removed and a Z project was made, in the same way as it was done for the open beam images. At this point, the resulting image was divided by the previously saved OB file. This is also done by the "image calculator" option. Finally, a min/max regulation was made to setup the image grey scale. The "Min..." command replaces pixels with a value lower than a specified constant by the constant itself, while the "Max..." command does the same to pixels with a value higher than a specified constant. The constants were set to -0.1 and +1.1. The resulting image was exported as ".tif" file, ready to be analyzed.
Since devices were irradiated at different time during the day, the best result is obtained if the open beam and dark current files closest in time are used for the image processing. However, since the outputs resulted to be almost identical, the same OB and DC files were used for processing all images. Also, to make this long procedure faster, a program macro was written and used, and it is reported in Appendix B.

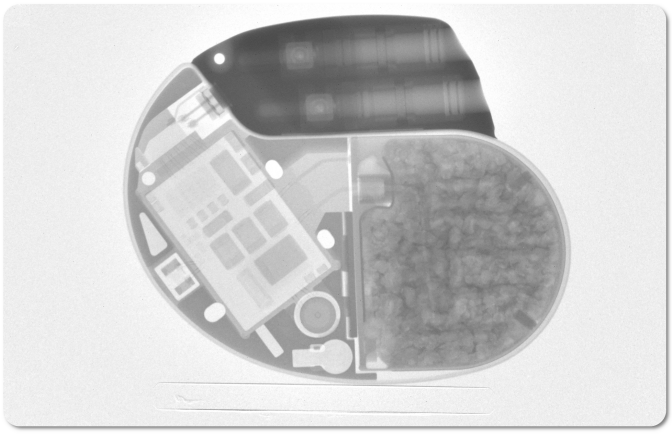

Figure 4.6. St. Jude Verity Adx XL VDR 5456, neutron radiography (processed image)

4.3 Results

4.3.1 Image Analysis

The processed images were analysed by eye and with the help of few ImageJ features in order to search for specific devices with possible presence of BPSG-covered components, expecially between similar models. Boron presency can be easily recognized for the higher neutron absorption resulting in a darker output.
Though, unfortunately, most images of similar devices didn't show any relevant difference, meaning that all similar devices may contain or not BPSG-covered components, a couple models showed a sensibly higher neutron absorption in some integrated circuits of specific units, which in principle can be a relevant clue for boron presency in such specific devices, in suffienct amount to induce damages by neutron absorption. The most relevant example is the Medico GEA DR showed in Figure 4.7.

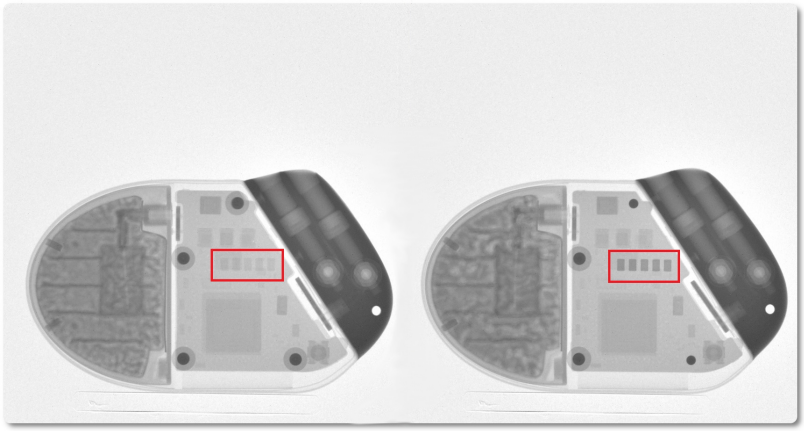

Figure 4.7. Neutron Radiography of two identical devices by Medico, showing a sensibly different neutron absorption in the same chips

As a further investigation, the same devices by Medico were also subjected to 6 MV gammagraphy (Figure 4.8) and conventional radiography at 70 kV (Figure 4.9).

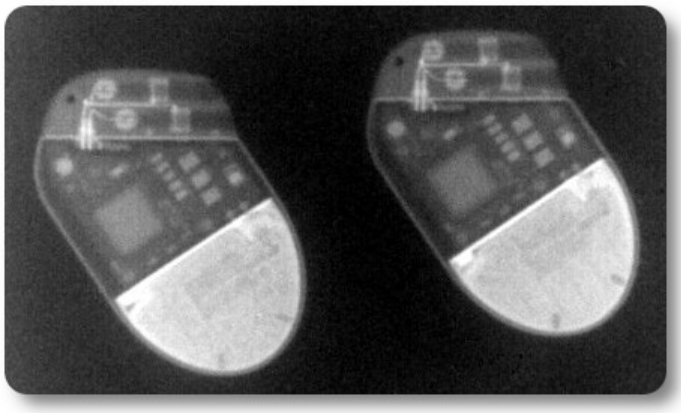

Figure 4.8. Gammagraphy (6 MV) of two identical devices by Medico, showing no difference in photon attenuation

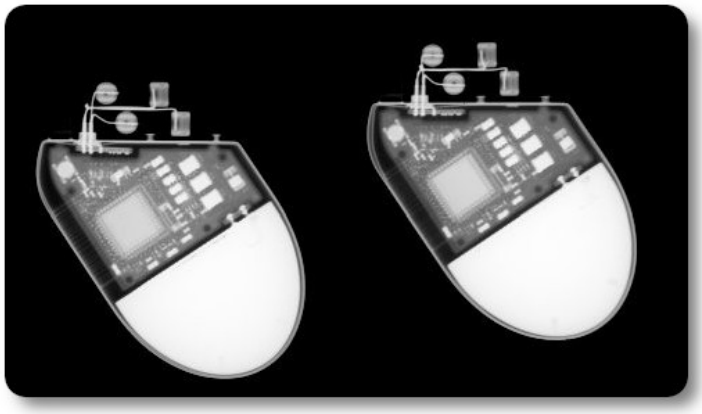

Figure 4.9. Traditional Radiography (70 kV) of two identical devices by Medico, showing no difference in photon attenuation

As we can see from Figure 4.8 and Figure 4.9, there is no difference in photon attenuation between the two devices. This result well agrees with our expectations. In fact, since electronic components are mostly made with semiconductors and metals in general, while boron is a light material with low photon attenuation properties, it is reasonable that BPSG presence do not interfere at all with the overall photon attenuation, despite having a key role in neutron absorption.
Nevertheless, the only BPSG precence may not be the only factor to be considered and the effective rise of malfunctions can be more or less probable depending on the overall electronic structure. In the following section, post-irradiation damages will be discussed.

4.3.2 Device Testing

The irradiation at the NEUTRA facility was performed between August 4^{th} and 6^{th} on a sample of 99 CIEDs including pacemakers and defibrillators, listed in Table 4.1. All devices, recently explanted from patients, were tested in mid July before the shipment and resulted to be working without errors and with a sufficient battery life. After the irradiation, one device could not be shipped back because it was too activated. The others were sent back in late August and were tested again between September and October.

Of the resulting sample of 98 devices, 32 were damaged (Table 4.2) and 8 showed a sensible variation in one or more working parameters or a sensible decrease in battery life. Though most damaged devices were affected by temporary malfunctions, some units showed a complete loss of functionality or could not be read by the diagnosis system. Noteworthy, 7 pacemakers could not be read because of telemetry errors,

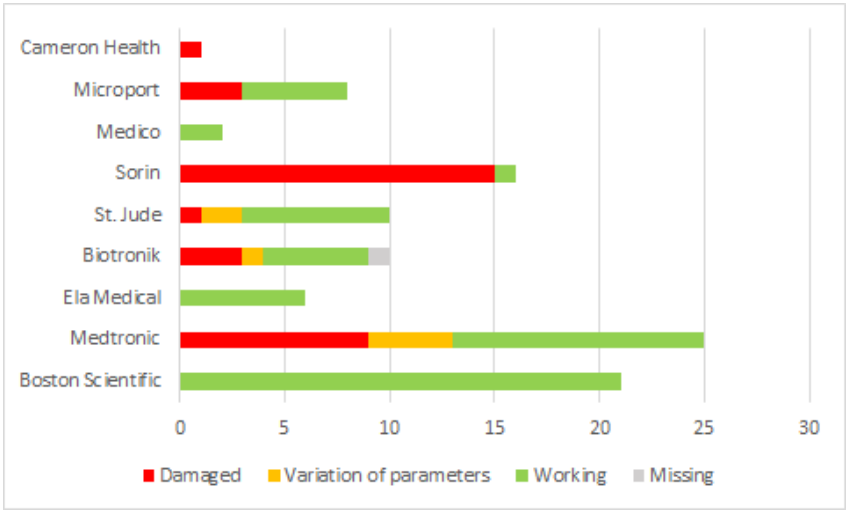

Figure 4.10. Summary of the diagnosis analysis conducted on the devices after the neutron radiography irradiation, divided per producer

1 resulted to be completely discharged and one was completely not working. Most devices had reset themselves or were waiting for a reprogramming. A single device showed a complete loss of information, including the date.

As we can see from Figure 4.10 and Table 4.2, Medtronic Adapta and Sorin devices in general were the most susceptible to damages, while Boston Scientific, former Ela Medical (now Microport) and Medico devices showed no damages at all. Also, pacemakers seem to be more prone to be damaged than internal defibrillators. Also, it's important to note that among the few devices that got irradiated for a longer time (up to 10 minutes), only one was damaged. So, we can exclude a direct relation between the delivered dose and the malfunction probability.

Table 4.1. Full list of CIEDs (PM = pacemaker, ICD = defibrillator) irradiated at the NEUTRA facility. * = parameters variation, ** = damaged devices and *** = not tested after the irradiation

Producer	Model	Tipo	Irradiation (min.s)	
Biotronik	Evia SR-T	PM	1.42	
Biotronik	Rivacor 7 HF-T QP	ICD	11.26	***
Biotronik	Lumax 740 VR-T	ICD	3.59	*
Biotronik	Enitra 8 SR-T	PM	2.12	
Biotronik	Epyra 8 DR-T	PM	1.45	
Biotronik	Epyra 8 DR-T	PM	1.56	
Biotronik	Lumax 740 HF-T	ICD	1.45	
Biotronik	Lumax 540 VR-T	ICD	1.40	**
Biotronik	TALOS SLR	PM	2.54	**
Biotronik	TALOS SLR	PM	1.47	**
Boston Scientific	ADVANTIO MRI J066	PM	2.05	
Boston Scientific	ENERGEN CRT-D P143	ICD	1.55	
Boston Scientific	ENERGEN CRT-D P142	ICD	1.42	
Boston Scientific	ADVANTIO MRI J066	PM	1.41	
Boston Scientific	ADVANTIO J063	PM	10.55	
Boston Scientific	ADVANTIO J063	PM	1.56	
Boston Scientific	INCEPTA CRT-D P162	ICD	1.39	
Boston Scientific	AUTOGEN MINI ICD D044	ICD	1.40	
Boston Scientific	ADVANTIO J063	PM	1.42	
Boston Scientific	INGENIO MRI J176	PM	1.40	
Boston Scientific	ADVANTIO MRI J066	PM	1.40	
Boston Scientific	ADVANTIO J063	PM	5.09	
Boston Scientific	COGNIS 100-D P108	ICD	1.44	
Boston Scientific	ADVANTIO J063	PM	1.40	
Boston Scientific	ADVANTIO MRI J066	PM	1.45	
Boston Scientific	Altrua 60 S601	PM	1.40	
Boston Scientific	ALTRUA 50	PM	2.05	
Boston Scientific	ALTRUA 50	PM	1.57	
Boston Scientific	ALTRUA 50	PM	2.07	
Boston Scientific	ALTRUA 50	PM	3.14	
Boston Scientific	ALTRUA 50	PM	1.54	
Cameron Health		ICD	1.36	*
Ela Medical	Elaview 3.02 HSO 2.82 Rhapsody D 20410 (D3)	PM	1.22	
Ela Medical	Elaview 3.02 HSO 2.82 Rhapsody D 20410 (D3)	PM	2.20	
Ela Medical	SYMPHONY	PM	4.02	
Ela Medical	SYMPHONY	PM	2.08	
Ela Medical	SYMPHONY	PM	2.39	
Ela Medical	SYMPHONY	PM	2.15	
Medico	GEA DR	PM	1.40	
Medico	GEA DR	PM	1.40	
Medtronic	Ensura DR MRI EN1DR01	PM	2.02	
Medtronic	Evera MRI S DR DDMC3D4	ICD	2.17	*
Medtronic	Visia AF MRI S VR DVFC3D4	ICD	1.37	*
Medtronic	Evera MRI S DR DDMC3D4	ICD	1.49	*
Medtronic	Sensia SEDR01	PM	2.10	
Medtronic	Viva Quad XT CRT-D DTBA2QQ	ICD	1.45	*
Medtronic	Viva Quad XT CRT-D DTBA2QQ	ICD	1.41	*
Medtronic	Viva Quad XT CRT-D DTBA2Q1	ICD	2.10	
Medtronic	Viva XT CRT-D DTBA2D1	ICD	1.37	
Medtronic	Viva S CRT-D DTBB2D1	ICD	2.10	

Table 4.1 continued from previous page

Producer	Model	Tipo	Irradiation (min.s)	
Medtronic	Ensura DR MRI EN1DR01	PM	1.50	
Medtronic	Relia RESR01	PM	1.42	
Medtronic	ADAPTA	PM	1.40	**
Medtronic	ADAPTA	PM	1.53	**
Medtronic	ADAPTA	PM	1.41	**
Medtronic	ADAPTA	PM	1.42	**
Medtronic	ADAPTA	PM	2.03	**
Medtronic	ADAPTA	PM	1.42	**
Medtronic	ADAPTA	PM	2.20	
Medtronic	ADAPTA	PM	1.40	**
Medtronic	ADAPTA	PM	1.42	**
Medtronic	ADAPTA	PM	1.42	**
Medtronic	ADAPTA	PM	1.37	**
Medtronic	VIVA QUAD XT CRT-D	ICD	1.45	
Medtronic	VIVA QUAD XT CRT-D	ICD	1.45	
Microport	Smartview 3.02 HSO 2.82 Esprit DW 2.92	PM	1.42	
Microport	Smartview 3.02 HSO 2.82 Esprit DW 2.76	PM	1.51	
Microport	Smartview 3.02 HSO 2.82 Esprit DW 2.76	PM	1.53	**
Microport	Smartview 3.02 HSO 2.82 Esprit DW 2.76	PM	1.46	
Microport	Esprit DW 2.75	PM	10.49	**
Microport	Smartview 3.02 HSO 2.82 Paradym DR W2.8.8	ICD	10.57	
Microport	Smartview 3.02 HSO 2.82 Paradym RF DR W3.104.4	ICD	1.46	
Microport	Smartview 3.02 HSO 2.82 Esprit DW 2.76	PM	1.50	**
Sorin	PLATINIUM VR 1210	ICD	1.17	
Sorin	ESPRIT DR	PM	3.48	**
Sorin	ESPRIT DR	PM	3.00	**
Sorin	ESPRIT DR	PM	1.48	**
Sorin	REPLY 200 DR	PM	1.40	**
Sorin	REPLY 200 DR	PM	1.41	**
Sorin	REPLY DR	PM	4.05	**
Sorin	REPLY DR	PM	1.40	**
Sorin	REPLY DR	PM	1.40	**
Sorin	REPLY DR	PM	1.40	**
Sorin	REPLY DR	PM	3.02	**
Sorin	REPLY SR	PM	1.44	**
Sorin	REPLY VDR	PM	2.00	**
Sorin	REPLY VDR	PM	1.41	**
Sorin	REPLY VDR	PM	1.40	**
Sorin	REPLY VDR	PM	1.40	**
St. Jude	Endurity 1162 Pacemaker	PM	1.54	
St. Jude	Anthem RF 3212 CRT-P	ICD	2.02	*
St. Jude	Quadra Assura MP 3371-40QC CRT-D	ICD	missing	
St. Jude	Unify Assura 3361-40Q CRT-D	ICD	2.07	
St. Jude	Current + DR 221136 ICD	ICD	missing	*
St. Jude	Verity Adx XL VDR 5456	PM	1.10	**
St. Jude	Quadra Assura 3367-40QC CRT-D	ICD	1.43	
St. Jude	PROMOTE QUADRA	ICD	2.03	
St. Jude	PROMOTE QUADRA	ICD	2.32	
St. Jude	PROMOTE QUADRA	ICD	1.47	

Table 4.2. List of damaged devices and errors

Producer	Model	Malfunction
Biotronik	LUMAX 540 VR-T	Entered Secutiry Mode on 06/08/2020 at 0:00
Biotronik	TALOS SLR	Re-initialized
Biotronik	TALOS SLR	Re-initialized
Medtronic	Adapta	Complete electronic reset (lost timestamp)
Medtronic	Adapta	Reprogrammed VVI 65
Medtronic	Adapta	Reprogrammed VVI 65
Medtronic	Adapta	Reprogrammed VVI 65
Medtronic	Adapta	Reprogrammed VVI 65
Medtronic	Adapta	Battery ran out of life
Medtronic	Adapta	Reprogrammed VVI 65
Medtronic	Adapta	Reprogrammed VVI 65
Medtronic	Adapta	Reprogrammed VVI 65
Medtronic	Adapta	Reprogrammed VVI 65
Microport	Esprit DW 2.75	Standby, waiting for reset
Microport	Smartview 3.02 HSO 2.82 Esprit DW 2.76	Reset
Microport	Smartview 3.02 HSO 2.82 Esprit DW 2.76	No device found
Sorin	Esprit DR	Standby, waiting for reinitialization
Sorin	Esprit DR	Standby, waiting for reinitialization
Sorin	Esprit DR	Telemetry error, impossible to interrogate
Sorin	Reply 200 DR	VVI 70 AIDA memory asking for reprogramming
Sorin	Reply 200 DR	VVI 70 AIDA memory asking for reprogramming
Sorin	Reply DR	Telemetry error, impossible to interrogate
Sorin	Reply DR	Telemetry error, impossible to interrogate
Sorin	Reply DR	Telemetry error, impossible to interrogate
Sorin	Reply DR	Telemetry error, impossible to interrogate
Sorin	Reply DR	Telemetry error, impossible to interrogate
Sorin	Reply SR	Standby, waiting for reinitialization
Sorin	Reply VDR	Telemetry error, impossible to interrogate
Sorin	Reply VDR	VVI 70 AIDA memory asking for reprogramming
Sorin	Reply VDR	Standby, waiting for reinitialization
Sorin	Reply VDR	Standby, waiting for reinitialization
St. Jude	Verity Adx XL VDR 5456	Backup VVI mode. Searching for software updates

Conclusions

The aim of this thesis work was to measure the neutron ambient dose equivalent around medical linear accelerators and to investigate on neutron interaction and neutron induced damages on cardiac implantable electronic devices. This chapter summarizes the main results obtained from both experiments and outlines the future steps in the long run of the work.

The experimental campaign for neutron measurement described in the present work was performed between July 2019 and October 2019 at different hospitals in Italy: "Ospedale Maggiore" (Trieste), "San Luca" (Lucca) and "Ospedale di Circolo e Fondazione Macchi" (Varese). The medical linear accelerators that were used were the Clinac DHX by Varian Medical Systems and the Synergy 3028 by Elekta.

Measurements of ambient dose equivalent were performed with the LUPIN detector (i.e. a REM counter specifically designer for pulsed neutron fields) and, according to availability, compared with traditional REM counters, bubble dosimeters and montecarlo simulations.

The measurement campaign was first focused on systematic and reproducible experiments. Radiation beams were delivered to a solid water phantom in different conditions (e.g. beam type, beam energy, field size) and the neutron ambient dose equivalent was measured at different distances from the isocenter of the machine on the patient bed. The second part of the campaign was to perform the simulation of real therapy plans and to measure the same quantity in more realistic conditions.

From our results, in line with expectations, the LUPIN detector resulted to be a good survey instrument and the only valid active detector for the neutron dose measurement in the radiation therapy pulsed neutron field. All other REM counters basically failed by pile-up. The measured H*(10) values, both for open beam experiments and therapy simulations, range from few μSv up to few mSv. In particular, the highest neutron dose is related to photon beams and increases a lot for increasing energy and field size. Instead, it is about one order of magnitude lower for electron beams.

From the measurements with bubble dosimeters, including previous literature data from the same linear accelerator, it is evident that the highest dose either inside and

out of the beam field is due to fast neutrons, but the thermal component is expecially relevant in terms of neutron fluence and far from the isocenter. Compared with the LUPIN, however, bubble dosimeters showed an evident underestimation of the dose. The montecarlo simulation, made in MCNPX by the University of Trieste for the Elekta system, was developed to compute the neutron ambient dose equivalent per unit of delivered Gy at different points along the patient bed and, compared to the LUPIN, results are well in agreement, either in terms of absolute values and trend with increasing distance.

The results of the neutron radiography conducted on a sample of 99 devices showed that the presence of BPSG covered chips in cardiac electronic devices may be possible, but is not related to specific models. In fact, similar models may all contain or not PBSG-covered components, but also the same model can contain them or not depending on the production lot or year. In fact, BPSG is an equivalent alternative to the more common PSG and usually no distinction is made during the manufacturing process. The presence of BPSG, in principle, can be cause of damages in electronic devices because of the neutron absorption in ^{10}B and the resulting nuclear reaction producing high-LET heavy charged particles. However, the actual occurrence of damages for sure depends on the electronic structure of the device and specific circuits can be more or less delicate. From the testing of CIEDs before and after the neutron irradiation, almost half devices - mainly pacemakers - showed errors, general malfunctions or a sensible variation of working parameters. Some devices suffered also a critical decrease in battery life, which in turn can be due to neutron absorption in lithium-6.

If we consider a neutron normalized dose of 1.5 mSv/Gy at 50 cm from the isocenter (from Table 3.2) as a reference scenario for 18 MV radiation therapy, and we consider a thermal dose contribution around 10%, which was found from bubble dosimeters [33], from the fluence-to-dose conversion coefficient reported in ICRP Publication 74 [44] we can derive a thermal fluence at the same distance in the order of 10^7 n/cm^2/Gy. Also, it must be considered that cardiac devices can be even closer to the primary beam, depending on the tumor site. Therefore, during the course of a 60 Gy radiation therapy, which is a typical dose for neck, breast and head cancer [45], the integral fluence at the device location should easily reach values around 10^9 n/cm^2. Since such value is in the same order of magnitude of the fluence used for most devices in neutron radiography at the NEUTRA station, and we can assume that electronic devices do not recover from damages between therapy sessions, we can conclude that in principle neutron radiography can be well representative for radiation therapy, and several malfunctions can occur to CIEDs in radiation therapy that are mainly due to

thermal neutrons.
However, since our study only focused on thermal neutrons, a similar sample of devices should be irradiated with a fast neutron source, for example Am-Be, to verify if also fast neutrons can induce damages. Also, a chemical analysis on dismantled components could be a valuable way to confirm with certainty the presence of BPSG, and in general it will be necessary to make the device manufacturers aware of the malfunctions that many devices can suffer, in order to develop more robust devices in terms of neutron-induced damages.

Appendix A

Neutron Dose in Proton Therapy

The European Radiation Dosimetry (EURADOS) Group is a european non-profit association promoting research and development in the field of ionizing radiation dosimetry. The overall work is performed by working groups (WG) and sub-groups, each one focusing on a different field. In particular, the WG9.2 is the group dedicated to "radiation dosimetry in radiotherapy - hadron therapy" and the WG11.2 is the one dedicated to "high energy radiation fields - high-energy high-dose rate pulsed fields dosimetry".
In the framework of a joint activity of the two groups [47], we were invited to perform a neutron dose measurement intercomparison at the proton therapy MAASTRO Clinic, Doctor Tanslaan 12, 6229 ET Maastricht (NL).
The MAASTRO Clinic houses the MEVION S250i Proton Therapy System with HYPERSCAN Pencil Beam Scanning. The Mevion HYPERSCAN is a concentric dual gantry configuration mounting a synchrocyclotron on the outer gantry to eliminate the traditional beamline. A 3D model of the Mevion system is shown in Figure A.1.

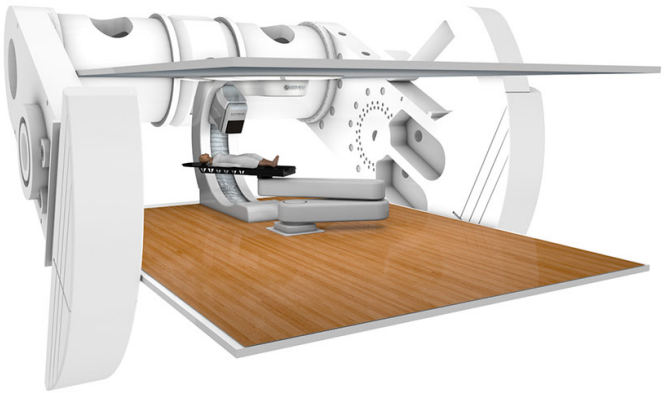

Figure A.1. 3D model of the Mevion 250i Hyperscan System

The inner gantry mounts the nozzle containing monitoring chambers, energy modulators and the multi-leaf collimator (adaptive aperture). The maximum proton energy is 227 MeV [48].
The use of proton beams for radiation therapy was proposed by Robert Wilson in 1946 [49], and the first irradiation was performed in 1954 at the Lawrence Berkeley National Laboratory, 1 Cyclotron Rd, Berkeley (California, U.S.). The main advantage of this technique over traditional radiation therapy is found in the high ballistic precision of protons. As shown in Figure A.2, protons gradually lose their energy in

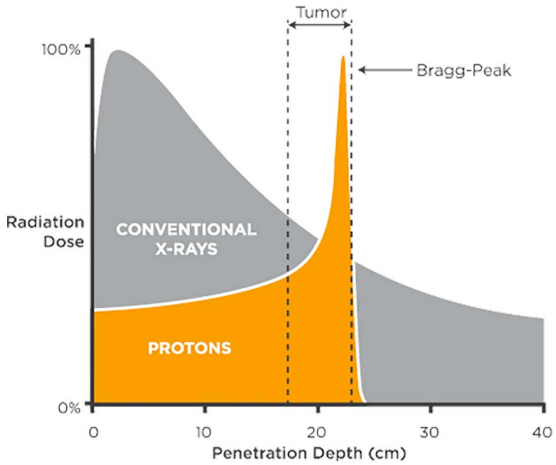

Figure A.2. Dose-depth curve of protons compared to conventional x-rays

tissue and lower is their energy, higher is the stopping power. For this reason, the stopping power increases in depth up to a peak. At such depth, the proton releases the maximum amount of dose and then is stopped. After that point, the proton has no more sufficient energy to produce any ionization, and the result is the so-called "Bragg Peak". Therefore, proton therapy results in a more precise, less invasive alternative to traditional radiation therapy, reducing the committed dose to healthy tissues and the risk of side effects.

A.1 Experimental Setup

The main goal of the intercomparison was the primary beam dosimetry by passive dosimeters. Active detectors, in addition, were used to measure the secondary neutron ambient dose equivalent at various positions around the machine. Following the result of previous intercomparisons [13], the LUPIN detector was chosen as the reference instrument for its capability to perform well in high energy pulsed neutron field, like it is the field generated by a synchrocyclotron. The neutron detectors that were used, together with their home institution, are reported in table A.1.

The experimental setup consisted in a phantom placed on the patient bed filled with passive dosimeters and 9 stands, one for each active detector, set around the machine at 0, ±22.5, ±45, ±90 and ±135 degrees at a distance of 225 cm from the isocenter[1], as shown in Figure A.3.

Figure A.3. Room setup at Maastro Clinic, with numbered positions

Table A.1. List of neutron detectors and home institution

Detector Name	Home Institution
LUPIN	Politecnico di Milano
LINUS	CERN
Wendy	Institute of Nuclear Physics Polish Academy of Sciences (IFJ)
Wendy	SCKCEN
Berthold	SCKCEN
Berthold	Skandion Clinic
Berthold	Universitat Autònoma de Barcelona (UAB)
RemPb	Helmholtz Zentrum München (HZM)
REM	HZM

The first experiment consisted in the simulation of different treatment plans, from 10 to 75 Gy total dose, delivered to a water phantom placed on the patient bed. For every simulation, each detectors was moved to a new position. The neutron ambient dose equivalent H*(10), acquired by the LUPIN detector for each run, is listed in Table A.2. To compare the performance between different detectors, for each session the neutron ambient dose equivalent measured by each instrument was registered and normalized to the RBE dose delivered to the phantom. Then, the responce of each detector was divided by the responce of the LUPIN.

[1]Due to physical constraint, position 8 was set at a 215 cm distance

Table A.2. Neutron H*(10) from Mevion S250i at different positions, measured by LUPIN

Pos.	Angle (deg)	Distance (cm)	Dose (Gy)	H*(10) (μSv)	Ratio (μSv/Gy)
1	0	225	10	1332	133
2	45	225	10	992	99
3	90	225	40	3911	98
4	135	225	30	6593	220
5	135	225	30	6616	221
6	90	225	10	1183	118
7	45	225	10	1328	133
8	22.5	215	40	3638	91
9	22.5	225	75	5805	77

Results are shown in Figure A.4. Figure A.5 also shows the dose rate profile as registered by the LUPIN detector.

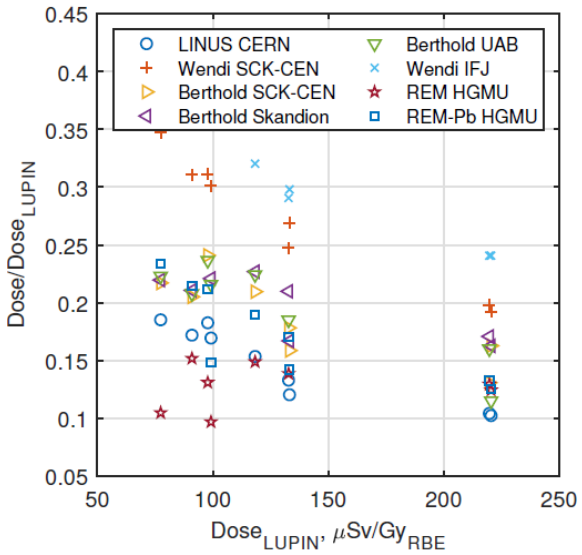

Figure A.4. Ratio between the responce of each rem counter and the LUPIN responce in terms of normalized dose (μSv/Gy)

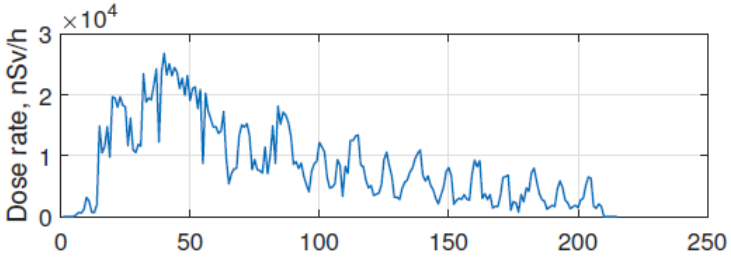

Figure A.5. Example of dose rate profile from experiment 1 (water phantom), acquired by LUPIN

The second experiment consisted in the irradiation of two anthropomorphic CIRS phantoms provided by the SCK-CEN institute, modeled on children of 5 and 10 years. In particular, a 40 Gy therapy plan was delivered multiple times from two different gantry angles, 90° and 140°. The comparison for the experiment involved only the LUPIN and LINUS detectors, in position 1 and 2. The overall result is a comparison between the LUPIN and LINUS detectors, for identical plan simulations at the same position.
Again, results are shown in Table A.3 and Figure A.6 shows the dose rate profile as registered by the LUPIN detector.

Table A.3. Comparison between the LUPIN and LINUS responce in terms of normalized dose

Phantom	Angle (deg)	Pos.	LUPIN (μSv/Gy)	LINUS (μSv/Gy)	LINUS/LUPIN
5y	90	2	33.05	5.32	0.16
5y	140	2	missing	4.91	
10y	90	2	33.38	5.32	0.16
10y	140	2	29.45	4.85	0.16
5y	90	1	53.98	4.04	0.07
5y	140	1	39.73	missing	
10y	140	1	40.53	3.62	0.09
10y	90	1	48.45	4.04	0.08

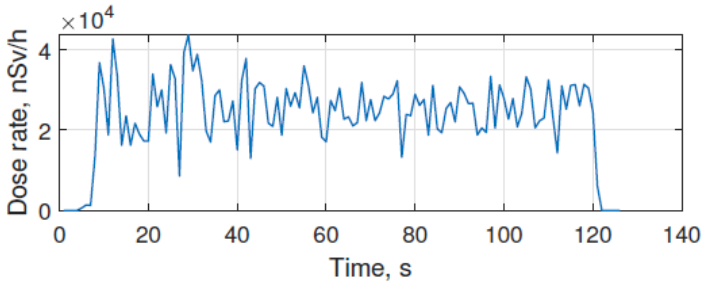

Figure A.6. Example of dose rate profile from experiment 2 (10 years CIRS), acquired by LUPIN

A.2 Results

Though part of the study, including the montecarlo simulation of the MEVION system, is yet to be done, preliminary results of the study were presented by the Polimi group at the EURADOS annual meeting 2020 (January 27^{th}-31^{st}, Florence, Italy). Similarly to previous intercomparisons, the measurements at the MAASTRO Clinic

show a relevant difference between the LUPIN and other detectors capability to perform neutron dose measurements in high energy pulsed fields. In fact, all detectors show a detection ratio below 0.5 when compared to the lupin detector, down to 0.1 for higher doses. This behaviour, mainly caused by the excessive pile-up of traditional REM counters working in pulse mode, makes most rem counters unsuitable for proton therapy dosimetry applications. For such reason, the LUPIN detector is possibly confirmed as the best reference active instrument for out-of-field dose evaluation in radiation therapy, including proton therapy delivered with modern synchrocyclotrons.

Appendix B

ImageJ Macro

The macro used for the image processing of neutron radiographs is here reported.

```
run("Flip Vertically", "stack");
selectWindow("data");
run("Enhance Contrast", "saturated=0.35");
imageCalculator("Subtract create 32-bit stack",
"data","MED_DCat1016.tif");
selectWindow("Result of data");
//run("Brightness/Contrast...");
run("Enhance Contrast", "saturated=0.35");
run("Remove Outliers...",
"radius=3 threshold=150 which=Bright stack");
run("Enhance Contrast", "saturated=0.35");
run("Z Project...", "projection=[Average Intensity]");
run("Enhance Contrast", "saturated=0.35");
imageCalculator("Divide create 32-bit",
"AVG_Result of data","AVG_OPat1014.tif");
selectWindow("Result of AVG_Result of data");
run("Enhance Contrast", "saturated=0.35");
run("Min...", "value=-0.1");
run("Max...", "value=1.1");
saveAs("Tiff", "C:/Result of AVG_Result of data.tif");
```

Acronyms

AIAC	"Associazione Italiana Aritmologia e Cardiostimolazione"
AIFM	"Associazione Italiana Fisica Medica"
AIRO	"Associazione Italiana Radioterapia Oncologica"
ADC	analog-to-digital converter
BPSG	borophosphosilicate glass
BD-PND	Bubble Detector - Personal Neutron Dosimeter
BDT	Bubble Detector Thermal
BOMAB	BOttle MAnnikin ABsorber
CIED	cardiac implantable electronic devices
DNA	Deoxyribonucleic Acid
DSB	double strand break
EURADOS	European Radiation Dosimetry
HZB	Helmholtz Zentrum Berlin
HZM	Helmholtz Zentrum München
IAEA	International Atomic Energy Agency
ICD	implantable cardioverter-defibrillators
ICRP	International Commission on Radiological Protection
ICRU	International Commission on Radiation Units and Measurements
IFJ	Institute of Nuclear Physics Polish Academy of Sciences
LET	Linear Energy Transfer
LINAC	linear particle accelerator
LUPIN	Long interval, Ultra-wide dynamic Pile-up free Neutron rem counter
OER	oxygen enhancement ratio

PM	pacemakers
PNF	pulsed neutron fields
PSG	phosphosilicate glass
PSI	Paul Scherrer Institute
RBE	Relative Biological Effectiveness
SSB	single strand break
UAB	Universitat Autònoma de Barcelona
WHO	World Health Organization
XRT	x-ray radiation therapy

Bibliography

[1] Hannah Ritchie, "Causes of death," *Our World in Data*, 2018. [Online]. Available: https://ourworldindata.org/causes-of-death

[2] WHO, "Cardiovascular diseases (CVDs) fact sheets," 2016.

[3] C. P. Stewart, B. W., Wild, "World Cancer Report 2014 - World Health Organization," *IARC Nonserial Publication*, 2014.

[4] M. Zecchin, M. Severgnini, A. Fiorentino, V. L. Malavasi, L. Menegotti, F. Alongi, D. Catanzariti, B. A. Jereczek-Fossa, M. Stasi, E. Russi, and G. Boriani, "Management of patients with cardiac implantable electronic devices (CIED) undergoing radiotherapy: A consensus document from Associazione Italiana Aritmologia e Cardiostimolazione (AIAC), Associazione Italiana Radioterapia Oncologica (AIRO), Associazione ," *International Journal of Cardiology*, vol. 255, no. March, pp. 175–183, 2018. [Online]. Available: https://doi.org/10.1016/j.ijcard.2017.12.061

[5] M. Zecchin, G. Morea, M. Severgnini, E. Sergi, A. Baratto Roldan, E. Bianco, S. Magnani, A. De Luca, A. Zorzin Fantasia, L. Salvatore, V. Milan, G. Giannini, and G. Sinagra, "Malfunction of cardiac devices after radiotherapy without direct exposure to ionizing radiation: Mechanisms and experimental data," *Europace*, vol. 18, no. 2, pp. 288–293, 2016.

[6] M. D. Falco, D. Genovesi, L. Caravatta, C. Di Carlo, B. Ekaterina, M. Appignani, M. Faustino, N. Furia, and E. Di Girolamo, "A randomized in vitro evaluation of transient and permanent cardiac implantable electronic device malfunctions following direct exposure up to 10 Gy," *Strahlentherapie und Onkologie*, 2020. [Online]. Available: https://doi.org/10.1007/s00066-020-01651-7

[7] A. Naseri and A. Mesbahi, "A review on photoneutrons characteristics in radiation therapy with high-energy photon beams," *Reports of Practical Oncology and Radiotherapy*, vol. 15, no. 5, pp. 138–144, 2010.

[8] A. V. Belousov, S. M. Varzar, M. V. Zheltonozhskaya, E. N. Lykova, and A. P. Chernyaev, "The Dose from Secondary Neutrons during the Operation of Modern Medical Accelerators," *Moscow University Physics Bulletin*, vol. 74, no. 6, pp. 551–558, 2019.

[9] IAEA, "Safety Reports Series No. 47 - Radiation Protection in the Design of Radiotherapy Facilities," p. 9, 2006. [Online]. Available: http://www-pub.iaea.org/MTCD/publications/PDF/Pub1223{_}web.pdf

[10] C. E. Cardenas, P. L. Nitsch, R. J. Kudchadker, R. M. Howell, and S. F. Kry, "Out-of-field doses and neutron dose equivalents for electron beams from modern Varian and Elekta linear accelerators," *Journal of Applied Clinical Medical Physics*, vol. 17, no. 4, pp. 442–455, 2016.

[11] E. Vagena, P. Katsaras, K. Theodorou, and S. Stoulos, "AMBIENT DOSE EQUIVALENT RECEIVED at 15 MV LINAC ENVIRONMENTS DUE to PHOTONEUTRONS CONTAMINATION," *Radiation Protection Dosimetry*, vol. 182, no. 4, pp. 472–479, 2018.

[12] M. Caresana, C. Cassell, M. Ferrarini, E. Hohmann, G. P. Manessi, S. Mayer, M. Silari, and V. Varoli, "A new version of the LUPIN detector: Improvements and latest experimental verification," *Review of Scientific Instruments*, vol. 85, no. 6, 2014.

[13] M. Caresana, A. Denker, A. Esposito, M. Ferrarini, N. Golnik, E. Hohmann, A. Leuschner, M. Luszik-Bhadra, G. Manessi, S. Mayer, K. Ott, J. Röhrich, M. Silari, F. Trompier, M. Volnhals, and M. Wielunski, "Intercomparison of radiation protection instrumentation in a pulsed neutron field," *Nuclear Instruments and Methods in Physics Research, Section A: Accelerators, Spectrometers, Detectors and Associated Equipment*, vol. 737, pp. 203–213, 2014. [Online]. Available: http://dx.doi.org/10.1016/j.nima.2013.11.073

[14] ICRP, "1990 Recommendations of the International Commission on Radiological Protection." *Annals of the ICRP*, 1991.

[15] D. Solpan, "Radiation Chemistry PPT Lecture," no. 2014, 2016.

[16] E. Britannica, "Encyclopedia - Britannica Online Encyclopedia," 2011.

[17] P. Guerrieri, P. Montemaggi, V. Budach, C. Stromberger, V. Budach, V. Budach, A. E. Dragun, V. Budach, F. T. Troicki, J. Poli, J. H. Brashears, G. E. Laramore, J. J. Liao, J. K. Rockhill, C. A. Perez, W. L. Thorstad, C. Oliai, C. Oliai, T. S.

Quang, L. Li, J. P. Lamond, S. Mose, T. S. Quang, T. C. Zhu, K. K.-H. Wang, T. W. Speer, P. Guerrieri, P. Montemaggi, R. Lanciano, D. E. Wazer, N. J. Yue, E. Limbergen, C. B. Saw, B. J. Fisher, L. C. Daugherty, D. E. Wazer, J. Wang, F.-M. Kong, I. Rusu, B. J. Fisher, L. C. Daugherty, and A. E. Dragun, "Linear Accelerators (LINAC)," in *Encyclopedia of Radiation Oncology*, 2013.

[18] K. Kainz, "Radiation Oncology Physics: A Handbook for Teachers and Students," *Medical Physics*, 2006.

[19] Glenn G. Knoll, *Radiation Detection and Measurement (4th Edition)*, 2010.

[20] G. P. Manessi, C. Welsch, M. Caresana, and M. Ferrarini, "The lupin detector: Supporting least intrusive beam monitoring technique through neutron detection," *IBIC 2013: Proceedings of the 2nd International Beam Instrumentation Conference*, no. December, pp. 648–651, 2013.

[21] M. Caresana, M. Ferrarini, G. P. Manessi, M. Silari, and V. Varoli, "A neutron detector for pulsed mixed fields: preliminary measurements," *Progress in Nuclear Science and Technology*, vol. 4, pp. 725–728, 2014.

[22] M. Ferrarini, V. Varoli, A. Favalli, M. Caresana, and B. Pedersen, "A wide dynamic range BF3 neutron monitor with front-end electronics based on a logarithmic amplifier," *Nuclear Instruments and Methods in Physics Research, Section A: Accelerators, Spectrometers, Detectors and Associated Equipment*, vol. 613, no. 2, pp. 272–276, 2010. [Online]. Available: http://dx.doi.org/10.1016/j.nima.2009.11.078

[23] M. Caresana, M. Ferrarini, G. P. Manessi, M. Silari, and V. Varoli, "LUPIN, a new instrument for pulsed neutron fields," *Nuclear Instruments and Methods in Physics Research, Section A: Accelerators, Spectrometers, Detectors and Associated Equipment*, vol. 712, pp. 15–26, 2013. [Online]. Available: http://dx.doi.org/10.1016/j.nima.2013.01.060

[24] G. P. Manessi, "Rivelatore attivo per campi di neutroni pulsati," MSc. Thesis, Politecnico di Milano, 2010.

[25] S. Marković, "Misure di dosi neutroniche presso acceleratori radioterapici mediante rivelatori attivi e passivi," BSc. Thesis, Università degli studi di Trieste, 2020.

[26] A. T. Feye, "Percentage depth dose and beam profile measurements for electron and photon beam in reference field size for different energies," *International Journal of Scientific & Engineering Research*, vol. 9, no. 2, pp. 1460–1464, 2018.

[27] M. Králík, J. Šolc, V. Vondráček, J. Šmoldasová, E. Farkašová, and I. Tichá, "Spectral fluence of neutrons generated by radiotherapeutic linacs," *Radiation Protection Dosimetry*, vol. 163, no. 3, pp. 373–380, 2014.

[28] X. S. Mao, K. R. Kase, J. C. Liu, W. R. Nelson, J. H. Kleck, and S. Johnsen, "Neutron sources in the varian clinac 2100C/2300C medical accelerator calculated by the EGS4 code," *Health Physics*, 1997.

[29] H. S. Kim, Y. H. Park, B. C. Koo, J. W. Kwon, J. S. Lee, and H. S. Choi, "Evaluation of the photoneutron field produced in a medical linear accelerator," *Radiation Protection Dosimetry*, vol. 123, no. 3, pp. 323–328, 2007.

[30] J. Liu, K. Kase, J. Kleck, X. Mao, W. Nelson, and S. Johnson, "Calculation of Photoneutrons from Varian Clinac Accelerators and Their Transmissions in Materials," pp. 1–5, 2006.

[31] R. M. Howell, S. F. Kry, E. Burgett, N. E. Hertel, and D. S. Followill, "Secondary neutron spectra from modern Varian, Siemens, and Elekta linacs with multileaf collimators," *Medical Physics*, vol. 36, no. 9, pp. 4027–4038, 2009.

[32] F. Biltekin, G. Ozyigit, M. Yeginer, D. Yildiz, M. Cengiz, F. Yildiz, F. Akyol, F. Zorlu, and M. Gurkaynak, "Ep-1487 the Neutron Contamination Measurement in High-Energy Electron Beams Therapy," *Radiotherapy and Oncology*, vol. 103, p. S568, 2012.

[33] S. Savatović, "Confronto tra misure di dosi neutroniche con diversi rivelatori presso acceleratori radioterapici ospedalieri," BSc. Thesis, Università degli studi di Trieste, 2018.

[34] L. Alticozzi, P. Barca, M. Caresana, R. Ciolini, F. D. Errico, C. Ferrante, V. Gagliardi, E. Lorenzini, E.-s. Ingegneria, and N.-c. Politecnico, "Interconfronto multicentrico per rivelatori di neutroni in radioterapia," in *Convegno Nazionale AIRP di Radioprotezione*. Perugia: AIRP, 2019, pp. 62–69.

[35] H. Ing, R. A. Noulty, and T. D. McLean, "Bubble detectors - A maturing technology," *Radiation Measurements*, vol. 27, no. 1, pp. 1–11, 1997.

[36] K. Alikaniotis, M. Severgnini, G. Giannini, and V. Milan, "Measurements of the parasitic neutron dose at organs from medical linacs at different energies by using bubble detectors," *Radiation Protection Dosimetry*, vol. 180, no. 1-4, pp. 267–272, 2018.

[37] K. Alikaniotis, "Combined tumour treatment by coupling conventional radiotherapy to an additional dose contribution from thermal neutrons," PhD Thesis, Università degli Studi di Trieste, 2018.

[38] C. Serra, "Results from: University of Vigo Surface Analysis Service C.A.C.T.I." Universoty of Vigo, Vigo, Tech. Rep., 2007.

[39] F. Gómez, A. Iglesias, and F. S. Doblado, "A new active method for the measurement of slow-neutron fluence in modern radiotherapy treatment rooms," *Physics in Medicine and Biology*, vol. 55, no. 4, pp. 1025–1039, 2010.

[40] A. Vazquez-Luque, J. Marin, J. A. Terron, M. Pombar, R. Bedogni, F. Sanchez-Doblado, and F. Gomez, "Neutron induced single event upset dependence on bias voltage for CMOS SRAM with BPSG," *IEEE Transactions on Nuclear Science*, vol. 60, no. 6, pp. 4692–4696, 2013.

[41] Swift Glass, "Glass Wafer Fabrication (Borosilicate & Quartz)," 2020. [Online]. Available: https://www.swiftglass.com/glass-wafers

[42] E. H. Lehmann, P. Vontobel, and L. Wiezel, "Properties of the radiography facility NEUTRA at SINQ and its potential for use as European reference facility," in *Nondestructive Testing and Evaluation*, 2001.

[43] S. Agosteo, A. Foglio Para, B. Maggioni, V. Sangiust, S. Terrani, and G. Borasi, "Radiation transport in a radiotherapy room," *Health Physics*, 1995.

[44] ICRP, *ICRP Publication 74. Conversion Coefficients for use in Radiological Protection against External Radiation.*, 1996.

[45] Yolanda Smith, "Radiation Therapy Dosage," 2018. [Online]. Available: https://www.news-medical.net/health/Radiation-Therapy-Dosage.aspx

[46] S. Agosteo, "Notes for the course "MEDICAL APPLICATIONS OF RADIATION FIELDS"," Milano, 2019.

[47] W. Rühm, E. Fantuzzi, R. Harrison, H. Schuhmacher, F. Vanhavere, J. Alves, P. Fattibene, M. A. Lopez, S. Mayer, S. Neumaier, P. Olko, H. Stadtmann, R. Tanner, and C. Woda, *Visions for Radiation Dosimetry over the Next*

Two Decades - Strategic Research Agenda of the European Radiation Dosimetry Group, 2014, no. May.

[48] M. Kang, R. Cessac, and D. Pang, "Commissioning and beam characterization of the first gantry-mounted accelerator pencil beam scanning proton system," *Medical Physics*, 2020.

[49] R. R. WILSON, "Radiological use of fast protons." *Radiology*, 1946.